REPORT DOCUMENTATION PAGE

Form Approved
OMB No. 0704-0188

The public reporting burden for this collection of information is estimated to average 1 hour per response, including the time for reviewing instructions, searching existing data sources, gathering and maintaining the data needed, and completing and reviewing the collection of information. Send comments regarding this burden estimate or any other aspect of this collection of information, including suggestions for reducing the burden, to Department of Defense, Washington Headquarters Services, Directorate for Information Operations and Reports (0704-0188), 1215 Jefferson Davis Highway, Suite 1204, Arlington, VA 22202-4302. Respondents should be aware that notwithstanding any other provision of law, no person shall be subject to any penalty for failing to comply with a collection of information if it does not display a currently valid OMB control number.
PLEASE DO NOT RETURN YOUR FORM TO THE ABOVE ADDRESS.

1. REPORT DATE *(DD-MM-YYYY)*	2. REPORT TYPE	3. DATES COVERED *(From - To)*
06/1/2006	Final	1 April 2003- 31 March 2006

4. TITLE AND SUBTITLE
High Cycle Fatigue Prediction for Mistuned Bladed Disks with Fully Coupled Fluid-Structural Interactions

5a. CONTRACT NUMBER

5b. GRANT NUMBER
F49620-03-1-0253

5c. PROGRAM ELEMENT NUMBER

6. AUTHOR(S)
Ge-Chenga Zha
Ming-Ta Yang

5d. PROJECT NUMBER

5e. TASK NUMBER

5f. WORK UNIT NUMBER

7. PERFORMING ORGANIZATION NAME(S) AND ADDRESS(ES)
University Of Miami
Dept. of Mechanical Engineering
Coral Gables, FL 33124

8. PERFORMING ORGANIZATION REPORT NUMBER

9. SPONSORING/MONITORING AGENCY NAME(S) AND ADDRESS(ES)
Air Force Office of Scientific Research /NM
4015 Wilson Blvd
Mail Room 713
Arlington, VA 22203
Dr. Fahroo

10. SPONSOR/MONITOR'S ACRONYM(S)

11. SPONSOR/MONITOR'S REPORT NUMBER(S)
AFRL-SR-AR-TR-06-0277

12. DISTRIBUTION/AVAILABILITY STATEMENT
Distribution A; distribution unlimited

13. SUPPLEMENTARY NOTES

14. ABSTRACT
During the period from April 2003 to March 2006, this research had been progressing well as planned toward the ultimate goal of simulating the mistuned rotor with fully-coupled fluid structure interaction. This is multidisciplinary comprehensive project that needs components from both fluid and structure dynamics.

15. SUBJECT TERMS

16. SECURITY CLASSIFICATION OF:			17. LIMITATION OF ABSTRACT	18. NUMBER OF PAGES	19a. NAME OF RESPONSIBLE PERSON
a. REPORT	b. ABSTRACT	c. THIS PAGE			19b. TELEPHONE NUMBER *(Include area code)*
U	U	U	UU		

Final Report to AFOSR, Dr. Fariba Fahroo

High Cycle Fatigue Prediction for Mistuned Bladed Disks with Fully Coupled Fluid-Structural Interactions

Final Report

on AFOSR HBCU/MI Grant F49620-03-1-0253

June, 2006

Ge-Cheng Zha[1]
Dept. of Mechanical Engineering
University of Miami
Coral Gables, Florida 33124
E-mail: zha@apollo.eng.miami.edu

Ming-Ta Yang[2]
Discipline Engineering - Structures
Pratt & Whitney
400 Main Street, M/S 163-07
East Hartford, CT 06108
E-mail: yangm@pweh.com

[1] Associate Professor, Director of CFD Lab.
[2] Principal Engineer.

20060809642

Chapter 1

Abstract

During the period from April 2003 to March 2006, this research had been progressing well as planned toward the ultimate goal of simulating the mistuned rotor with fully-coupled fluid structure interaction. This is a multidisciplinary comprehensive project that needs components from both fluid and structure dynamics. The following important capabilities have been achieved and the detailed results are presented in the report.

1) A new accurate and efficient Riemann solver, Zha E-CUSP2 scheme, has been developed and applied to moving grid systems for fully coupled fluid-structure interaction. The schemes are validated to possess very low numerical diffusion and be able to capture crisp shock and contact discontinuities. The robustness and efficiency of the scheme is essential for the calculation of fluid-structural interactions.

2) The fully coupled fluid-structural interaction methodology has been developed and is successfully applied to predict the 2D and 3D transonic wing flutter. For the fluid-structural interaction, an implicit time marching method with dual time stepping algorithm and unfactored Gauss-Seidel line relaxation is employed to achieve fast convergence rate. For the 2D cases, the exact structural equations are solved. For the 3D AGARD wing, a modal approach is used to be consistent with the Subsets of Nominal Modes (SNM) model of the Mistuned rotor.

3) A non-reflective boundary condition based on Navier-Stokes equations in generalized coordinates has been developed to accurately treat the boundaries of the unsteady flows to remove the reflective waves.

4) The transient response (time domain) structural vibration model for mistuned rotor bladed disk based on the efficient SNM model has been developed. The vibration response results predicted by the SNM model for a full annulus bladed disk with blade frequency variation agree very well with the results predicted by the finite element model.

5) The code has been intensively validated with several cases including steady state 2D transonic airfoil and 3D wing, unsteady vortex shedding of a stationary cylinder, induced vibration of a cylinder, forced vibration of a pitching airfoil, induced vibration and flutter boundary of 2D NACA 64A010 transonic airfoil, 3D plate wing structural response. The predicted results agree well with benchmark experimental results or the results calculated by a finite element solver for structural response. The limited cycle oscillation (LCO) is captured.

6) The full 3D AGARD wing flutter boundary is calculated and agree well with the experiment. The "sonic dip" phenomenon is captured.

This solver based on the fully coupled fluid-structural interaction is ready to calculate the mistuned rotor flutter and forced response. However, since the funding is only 3 years, which is one year shorter than the 4 years time period originally proposed, the mistuned rotor simulation is not finished and will be completed in future when the funding is available.

In this research project, we have 5 journal papers, 2 papers submitted for journal publications, and 12 conference papers.

Contents

1 Abstract **3**

2 Introduction **9**

3 Numerical Strategy **13**

3.1 Low Diffusion High Efficiency Upwind Scheme 13

3.2 Implicit Time Marching Scheme 14

3.3 Non-Reflective Boundary Conditions 14

3.4 Modal Structural Solver 16

3.5 High Performance Computing 17

4 Discretization Schemes **19**

4.1 Flow Governing Equations 19

4.2 Time Marching Scheme 21

4.3 The Zha E-CUSP Scheme[1, 2] 22

4.3.1 Numerical Dissipation 25

4.3.2 Zha E-CUSP2 Scheme[3] 26

4.4 Roe's Riemann Solver on Moving Grid System[4, 5] 26

4.5 Conventional Boundary Conditions 27

4.6 Moving/Deforming Grid Systems 28

4.7 Geometric Conservation Law 29

5 Non-Reflective Boundary Conditions **31**

5.1 Characteristic Form of the Navier-Stokes Equations[6] 31

5.2 Non-Reflective Boundary Conditions[6] 35

5.2.1 Supersonic outflow boundary conditions 36
5.2.2 Subsonic outflow boundary conditions 36
5.2.3 Subsonic inflow boundary conditions 38
5.2.4 Adiabatic wall boundary conditions 38

6 Structural Models **41**
6.1 Modal Approach for 3D Wing[4] 41
6.2 Mistuned Bladed Structural Model for Transient Response 44

7 Fully Coupled Fluid-Structural Interaction **47**

8 Results and Discussion **49**
8.1 Validation of Zha-Hu E-CUSP Schemes[1] 49
8.1.1 Shock Tubes 49
8.1.2 Entropy condition 51
8.1.3 Wall Boundary Layer 52
8.1.4 Transonic Converging-Diverging Nozzle 53
8.1.5 Transonic Inlet-Diffuser 54
8.2 Validation of the Zha E-CUSP2 Scheme[3] 55
8.2.1 Transonic Converging-Diverging Nozzle 55
8.3 2D Flow Induced Vibration 56
8.3.1 Stationary Cylinder 56
8.3.2 Vortex-Induced Oscillating Cylinder 57
8.3.3 Elastically Mounted Airfoil 59
8.3.4 Forced Pitching Airfoil 60
8.3.5 Flow-Induced Vibration of NACA 64A010 Airfoil 61
8.3.6 2D Airfoil Flutter Boundary Prediction 63
8.4 SNM Model Used for Transient Response 64
8.4.1 Low Frequency Case 65
8.4.2 High Frequency Case 65
8.5 Non-Reflective Boundary Conditions 66
8.5.1 A Vortex propagating through a outflow boundary 66

8.5.2 Inlet-Diffuser Flow 68
8.5.3 Steady State Solutions 68
8.5.4 Unsteady Solutions 69
8.6 Separated Flow of NASA 3D Flutter Cascade 70
8.6.1 Steady state results 71
8.6.2 Unsteady separated flow simulation 72
8.7 Forced Vibration of the NASA Flutter Cascade 75
8.7.1 Parameters used in flow analysis 75
8.7.2 The Cascade 76
8.7.3 Computation domain decomposition and mesh generation . . . 77
8.7.4 Simulation in two passage cascade 78
8.7.5 Simulation in full scale cascade 79
8.8 3D AGARD Wing Flutter Prediction 82
8.8.1 Steady State Transonic ONERA M6 wing 82
8.8.2 Validation of Structural Solver 83
8.8.3 AGARD Wing 445.6 Flutter 83

9 Personnel **85**

10 Conclusions **87**
10.1 The New E-CUSP scheme 87
10.2 Non-Reflective Boundary Conditions 88
10.3 2D Flutter Prediction 89
10.4 SNM model of Transient Response 89
10.5 Separated Flows in NASA 3D Flutter Cascade 90
10.6 Forced Vibration of the NASA Flutter Cascade 90
10.7 3D AGARD Wing Flutter Prediction 91
10.8 Future Work 92

11 Publications **93**

12 Acknowledgment **97**

Chapter 2

Introduction

Flow induced structural vibration is one of the most critical technical problems affecting the readiness of the US Air Force fleet today. Due to the extremely complicated non-linear flow-structure interaction phenomena, there is a lack of high fidelity computational tools to study the basic physics and to predict the structural failure. The problems are more complex for the aircraft engine turbomachinery than airframe because the turbomachinery has numerous blades and is much more complicated than the one or two wings of the external airframe.

For aircraft engine turbomachinery, the most general flow induced vibration problem is the mistuning problem. The mistuning refers to the fact that, in a bladed disk, blade responses can significantly differ from each other due to small geometric variations from blade to blade. The small variations typically result from within-tolerance manufacturing imperfections or in-service wear-offs, which are difficult to eliminate in the production process or during the life span of an engine. In other words, virtually all turbomachinery bladed disks are mistuned. However, up to date, almost all of the fluid-structure interaction research work focuses on the tunned systems because the mistuned systems are much more challenging.

This research is to develop a methodology to couple a state of the art CFD code, RANS3D (3D unsteady Reynolds averaged NS solver), with a state of the art structural model, SNM (Subset of Nominal Modes), for a mistuned bladed disk. The aerodynamic force and blade motion of a full annulus rotor are unknown variables and are simultaneously solved within each time step. No prescribed blade motion is used to accurately represent the coupled system. The process proceeds in temporal direction step by step until it reaches desired solutions for forced response or flutter.

The methodology developed in this research is based on the strategy of computing frameworks recently suggested by Melville[7]. The computing frameworks is to fully take advantages of the state of the art of each individual discipline and the multidisciplinary computation is connected through standard interfaces. In this research,

the multi-disciplines involved are the CFD model and the structural model. Since the methodologies of each individual discipline have been developed and matured independently, each methodology will usually use different grid generation and time marching scheme to achieve the highest possible accuracy and efficiency. A common interface to conserve the energy between the fluid aerodynamic forcing and the structural deformation is necessary to combine the CFD and structural solvers. The strategy of the computing frameworks will allow the two disciplines to continue to develop their state of the art and ensure that the multi-disciplinary solver will always be at the forefront of the technology.

Currently, the method used to predict the aerodynamic damping of mistuned bladed disks is based on the Influence Coefficient Technique which requires prescribed blade motion (Silkowski et. al., 2001) [8]. This technique assumes no structural coupling between blades and does not account for the feedback from the mistuned structure to the fluid field or vice versa. The accuracy of such approach is questionable when the structural coupling is important or highly nonlinear flow conditions exist. For instance, at stall flutter region, there may exist large oscillating separation, rotating stall cells, shock motion, oscillating tip vortex, etc. Under this circumstance, it is not feasible to prescribe the blade motion caused by the complicated interaction between the flow and the structure.

To simulate the vibratory response of a mistuned bladed disk, the sector model used for a tuned system is no longer applicable. A model that simulates the whole bladed disk is needed to take into account the asymmetric pattern of the blade vibration around the full annulus (Hilbert and Blair, 2001) [9], which includes the differences in amplitudes, unequal phase differences between adjacent blades, and sometimes changes in blade mode shapes.

There are increasing efforts recently to couple a computational fluid dynamics(CFD) solver with a structural solver, in particular for external airframe problems. Bendiksen et al. pioneered the research by using an explicit CFD code coupled with a structural integrator based on the convolution integral to obtain the flutter boundary for a NACA 64A010 airfoil[10]. Alonso and Jameson etc. developed a dual-time step coupled aeroelastic solver for 2D airfoils[11, 12]. Similar techniques was applied to 3D wing with an finite element structural model by Liu etc[13]. Melville et al. developed a fully implicit method based on Beam-Warming scheme with a coupled modal structural solver for a 3D wing[14].

Due to the difficulties in turbomachinery, calculation of fluid induced vibration based on fully coupled fluid-structure interaction has began only very recently. The research group in UK led by Dr. Imregun has made notable progresses (Breard, et al. 1999, Sayma 2001a, Sayma 2001b, Sayma 2001c, Sayma 2001d) [15][16][17][18]. They carried out full annulus and multiblade row computations for forced response and flutter. The flow solutions are primarily based on Euler equations with limited 3D Navier-Stokes modeling and the structural response is simulated by mode shapes

of bladed disks. Nonlinear friction constraints are considered in their study; however, no mistuning study was attempted. In addition, in their work, a mode superposition of the structure is incorporated into a finite element CFD solver. This method hence may not best fit the computing frameworks[7]. In 2002, Doi and Alonso[19] applied their dual time stepping CFD algorithm[11, 12] with the structural solver of MSC/NASTRAN to simulate a tuned compressor rotor fluid-structural interaction. In the model of Doi and Alonso[19], the fluid and structural models are closely coupled but structural deformation is lagged. This method may be limited to first-order accuracy in time regardless of the temporal accuracy of the individual solvers[14].

To achieve the research goal, the numerical strategy is given in the next chapter. The details of the numerical algorithms are given in chapter 4.

Chapter 3

Numerical Strategy

The challenges for high cycle fatigue prediction based on a fully coupled fluid-structural interaction are two-folds, efficiency and accuracy. The fully coupled fluid-structural interaction needs to iterate the flow and structural solver within each physical time step. It is a very CPU time consuming task and the dynamic response of the system is sensitive to the numerical dissipation introduced by the numerical scheme. Consequently, it's required that the numerical scheme is able to model the flow field with high efficiency and low numerical diffusion.

3.1 Low Diffusion High Efficiency Upwind Scheme

Recently, there have been many efforts to develop efficient Riemann solvers using scalar dissipation instead of matrix dissipation. For the scalar dissipation Riemann solver schemes, there are generally two types: H-CUSP schemes and E-CUSP schemes [20, 21, 22]. The abbreviation CUSP stands for "convective upwind and split pressure", named by [20, 21, 22]. The H-CUSP schemes have the total enthalpy from the energy equation in their convective vector, while the E-CUSP schemes use the total energy in the convective vector. Liou's AUSM family schemes [23], Van Leer-Hänel scheme [24], and Edwards's LDFSS schemes [25, 26] belong to the H-CUSP group.

The H-CUSP schemes may have the advantage of better conserving the total enthalpy for steady state flows. However, from the characteristic theory point of view, the H-CUSP schemes are not fully consistent with the disturbance propagation directions, which may affect the stability and robustness of the schemes [1]. The H-CUSP scheme may have more inconsistencies when it is extended to the moving grid system. It will leave the pressure term multiplied by the grid velocity in the energy flux, which cannot be contained in the total enthalpy, and must therefore be treated as part of the pressure term. From a characteristic point of view, it is not obvious how to treat this term in a consistent manner.

In this research, we developed an efficient E-CUSP scheme, Zha E-CUSP2 scheme, which is consistent with the characteristic directions [1, 3]. The scheme has low diffusion and is able to capture crisp shock profiles and exact contact discontinuities. The scheme is more CPU efficient since it only uses the scalar dissipation. In addition, is is fairly straightforward to extend the new scheme to the 3D moving grid system[27, 4, 28]. This is because the grid velocity belongs to the convective terms in the E-CUSP schemes. The pressure term is determined by the weighted average based on the wave eigenvalues from downstream and upstream. The new E-CUSP scheme is more efficient than the Roe scheme without matrix operation. For a 2D nozzle calculation for comparison, the CPU time to evaluate the flux using the new E-CUSP scheme is only about 1/4 of that needed by the Roe scheme [1].

3.2 Implicit Time Marching Scheme

Among the researchers in the area of 3D time-marching aeroelastic analysis based on Euler/Navier-Stokes approaches, Lee-Rausch and Batina[29][?] used a three-factor, implicit, upwind-biased Euler/Navier-Stokes approach coupled with a lagged structure solver. Morton, Melville and Gordnier et al. developed an implicit fully coupled fluid-structure interaction model, which used the Beam-Warming implicit approximate factorization scheme for the flow solver coupled with modal structural solver [30][31][14][32]. Liu et al. developed a fully coupled method using Jameson's explicit scheme with multigrid approach utilizing Euler equations and a modal structural model[13]. Doi and Alonso[19] coupled an explicit Runge-Kutta multigrid RANS flow solver with a FEM structure solver to predict the aeroelastic responses of NASA Rotor 67 blade.

In this research, we have developed an implicit time marching algorithm using a dual-time stepping unfactored line Gauss-Seidel iteration [5, 2, 4, 28]. The unfactored Gauss-Seidel iteration is unconditionally stable and allows larger pseudo or physical time steps than explicit method. It avoids the factorization error introduced by those implicit approximate factorization methods, such as those used in [29][30][31][14][32]. Even though the factorization error diminishes within each physical time step, the factorization error can limit the numerical stability. The linear stability analysis shows that approximate factorized method is not stable for 3D computation even though it is stable for 2D computation.

3.3 Non-Reflective Boundary Conditions

The accuracy of unsteady flow calculations relies on accurate treatment of boundary conditions. Due to the limitation of computer resources, usually only a finite computational domain is considered for a flow calculation. This means that we have to

"cut off" the domain that is not of our primary interest. However, the cut boundaries may cause artificial wave reflections, which may include both physical waves and numerical waves[33]. Such waves may bounce back and forth within the computational domain and may seriously contaminate the solutions and produce misleading results. This is particularly true for internal flows such as the flows in turbomachinery, in which the computational domain usually is confined very near the solid objects. For example, previous studies indicated that the different treatments of numerical perturbation at upstream and downstream boundaries can change the compressor blade stall inception pattern [34] [35].

The currently often used non-reflective boundary conditions for unsteady internal flows are based on eigenvalue analysis of linearized Euler equations developed by Giles[36]. However, Giles' method may only apply to the inviscid solutions which require the far field flow to be uniform so that the propagation waves have the Fourier mode shapes. For viscous flows, the mean flow in the downstream far field region may be non-uniform due to the airfoil or blade wakes, which means that there will be no Fourier mode shapes. In addition, the inconsistency of the Navier-Stokes governing equations for the inner domain and linearized Euler equations at far field boundary may also cause numerical wave reflections.

The more rigorous treatment of non-reflective boundary conditions (NRBC) for Navier-Stokes equations is the one suggested by Poinsot and Lele in 1992[33] for Direct Numerical Simulation of turbulence. However, the NRBC given by Poinsot and Lele in [33] is only for the regular mesh aliened with the coordinate axises in Cartesian coordinates. The explicit time marching scheme was used in the calculation of Poinsot and Lele. For practical engineering applications, the body fitted generalized coordinates are usually necessary. In 2000, Kim and Lee [37] made an effort to extend the NRBC of Poinsot and Lele from the Cartesian coordinates to generalized coordinates. However, in their derivation, a flaw was made by absorbing the eigenvector matrix into the partial derivatives, their formulations apply only if: 1) it is 1D equation; 2) the eigenvector matrix is constant in the flow field; 3) the partial differential equations satisfy Pfaff's condition. For multidimensional Navier-Stokes equations, all these three conditions are not satisfied[38, 39]. Hence, the wave amplitude vector derived in [37] is erroneous.

More recently, based on the characteristic approach of Poinsot and Lele[33], Bruneau and Creuse [40] suggested a variation of the approximate treatment of the incoming wave amplitude in the exit boundary conditions by assuming that the pressure and velocity values will "convect" with time to the location where the phantom cells are located. The results show the method works well. Prosser and Schluter [41] used an approach based on a low Mach number asymptotic expansion of the the governing equations to improve the specification of time dependent boundary conditions. With the help of the Local One-Dimensional Inviscid (LODI) relations, Moureau et al.[42] implemented characteristic boundary conditions for multi-component mixtures

in DNS and LES computations using a modified NRBC formulation.

In this research, we extend the NRBC system of Poinsot and Lele[33] from Cartesian coordinates to generalized coordinates and apply it numerically for unsteady calculations in an implicit time marching method. In a finite difference or finite volume approach, the governing equations are more straightforward to be solved in generalized coordinates, in which a complex physical domain becomes a rectangular computational domain (for 2-D case) or a hexahedral computational domain (for 3-D case) with equal grid spacings. The moving grid effect can be naturally included in the generalized coordinates. Strictly speaking, for finite differencing or finite volume methods, only solving the equations in generalized coordinates can preserve the accuracy of high order numerical schemes.

In general, implicit methods permit a larger time step and are widely used for many practical applications. To be consistent with the implicit solver of the inner domain, in this paper, the NRBC equations are implicitly discretized and solved simultaneously in a fully coupled manner. Two numerical cases are tested in this paper: a vortex propagating through a outflow boundary and a transonic inlet-diffuser flow with shock/boundary layer interaction. The numerical results indicate that the present methodology is robust and accurate.

The strategy is to fully couple the flow and structural solver within each time step by iterating the flow solution and structural deformation. Since the fully coupled fluid-structural interaction is very CPU intensive, this research has developed high efficiency high accuracy CFD and structural algorithms. The following sub-section will outline the developed methodology. The detailed numerical algorithms are described in next chapter.

3.4 Modal Structural Solver

Since the full annulus of a mistuned rotor will be calculated, the nonlinear 3D Navier-Stokes equations are CPU intensive. Hence it is very important that the structural solver is CPU efficient and accurate. Based on this consideration, the structural solver completely based on the finite element method for the mistuned bladed disk is not favored due to the high CPU cost.

For this proposed research, the structural solution for a mistuned bladed disk will employ the SNM model in time domain(Yang and Griffin, 2001)[43] developed under the support of the GUIde Consortium (Government, Universities, and Industry). The SNM model uses a subset of tuned bladed disk modes to represent the vibration of a mistuned bladed disk. It is verified that the SNM model is both numerically accurate and computationally efficient (Srinivasan, 1999) [44].

Other well-recognized models for mistuned bladed disks include TURBO REDUCE

(Kruse and Pierre, 1996)[45] and MISTRESS (Petrov et. al., 2000) [46]. TURBO REDUCE utilizes a Component Mode Synthesis (CMS) technique that accounts for blade frequency mistuning only. MISTRESS and SNM, on the other hand, employ the Modal Reduction (MR) technique which allows general mistuning of the structure including mass and stiffness variations. Since it is our desire to develop a methodology that can be applied to general mistuning problems, Modal Reduction technique (MISTRESS and SNM) became the method of our choice. A detailed comparison of CMS and MR techniques for mistuned bladed disk vibration is documented by Moyroud et al, 2002 [47].

We selected SNM over MISTRESS based on the following three reasons:

1. The fluid-structural interaction problem requires the calculation of the vibration of all nodes on the surfaces of the airfoils of a bladed disk.

2. MISTREE uses the receptance method which is only efficient when the number of nodal solutions calculated is limited (e.g., the study of the vibration of a mistuned bladed disk with friction dampers only interests in the vibration at a limited number of friction joints.) Using MISTRESS for our study would be computationally expensive since the number of nodes on the airfoil surfaces of a bladed disk can range from 10,000 to 100,000.

3. SNM uses a limited set of tuned modes to represent the vibration of a mistuned bladed disk. Its efficiency solely depends on the number of tuned modes of choice. The typical number of modes needed to represent an industrial bladed disk is in the order of 100 (Srinivasan, 1999) [44].

Considering CFD calculation is very CPU intensive, using SNM to simulate the response of mistuned bladed disks becomes particularly appealing and essential to make the simulation of the fully coupled fluid-structural problem possible.

3.5 High Performance Computing

The parallel computing capability based on SPMD (Single Program Miltiple Data) is implemented in our code to reduce the wall clock calculation time. The reduction of wall clock time by parallel computing is essential and necessary.

Chapter 4

Discretization Schemes

4.1 Flow Governing Equations

The governing equations for the flow field computation are the Reynolds-Averaged Navier-Stokes equations (RANS) with Favre mass average which can be transformed to the generalized coordinates and expressed as:

$$\frac{\partial \mathbf{Q}'}{\partial t} + \frac{\partial \mathbf{E}'}{\partial \xi} + \frac{\partial \mathbf{F}'}{\partial \eta} + \frac{\partial \mathbf{G}'}{\partial \zeta} = \frac{1}{Re}\left(\frac{\partial \mathbf{E}'_{\mathbf{v}}}{\partial \xi} + \frac{\partial \mathbf{F}'_{\mathbf{v}}}{\partial \eta} + \frac{\partial \mathbf{G}'_{\mathbf{v}}}{\partial \zeta}\right) \tag{4.1}$$

where Re is the Reynolds number and

$$\mathbf{Q}' = \frac{\mathbf{Q}}{J} \tag{4.2}$$

$$\mathbf{E}' = \frac{1}{J}(\xi_t \mathbf{Q} + \xi_x \mathbf{E} + \xi_y \mathbf{F} + \xi_z \mathbf{G}) = \frac{1}{J}(\xi_t \mathbf{Q} + \mathbf{E}'') \tag{4.3}$$

$$\mathbf{F}' = \frac{1}{J}(\eta_t \mathbf{Q} + \eta_x \mathbf{E} + \eta_y \mathbf{F} + \eta_z \mathbf{G}) = \frac{1}{J}(\eta_t \mathbf{Q} + \mathbf{F}'') \tag{4.4}$$

$$\mathbf{G}' = \frac{1}{J}(\zeta_t \mathbf{Q} + \zeta_x \mathbf{E} + \zeta_y \mathbf{F} + \zeta_z \mathbf{G}) = \frac{1}{J}(\zeta_t \mathbf{Q} + \mathbf{G}'') \tag{4.5}$$

$$\mathbf{E}'_{\mathbf{v}} = \frac{1}{J}(\xi_x \mathbf{E}_{\mathbf{v}} + \xi_y \mathbf{F}_{\mathbf{v}} + \xi_z \mathbf{G}_{\mathbf{v}}) \tag{4.6}$$

$$\mathbf{F}'_{\mathbf{v}} = \frac{1}{J}(\eta_x \mathbf{E}_{\mathbf{v}} + \eta_y \mathbf{F}_{\mathbf{v}} + \eta_z \mathbf{G}_{\mathbf{v}}) \tag{4.7}$$

$$\mathbf{G}'_{\mathbf{v}} = \frac{1}{J}(\zeta_x \mathbf{E}_{\mathbf{v}} + \zeta_y \mathbf{F}_{\mathbf{v}} + \zeta_z \mathbf{G}_{\mathbf{v}}) \tag{4.8}$$

where the variable vector $\mathbf{Q}$, and inviscid flux vectors $\mathbf{E}$, $\mathbf{F}$, and $\mathbf{G}$ are

$$\mathbf{Q} = \begin{pmatrix} \bar{\rho} \\ \bar{\rho}\tilde{u} \\ \bar{\rho}\tilde{v} \\ \bar{\rho}\tilde{w} \\ \bar{\rho}\tilde{e} \end{pmatrix}, \mathbf{E} = \begin{pmatrix} \bar{\rho}\tilde{u} \\ \bar{\rho}\tilde{u}\tilde{u} + \tilde{p} \\ \bar{\rho}\tilde{u}\tilde{v} \\ \bar{\rho}\tilde{u}\tilde{w} \\ (\bar{\rho}\tilde{e} + \tilde{p})\tilde{u} \end{pmatrix}, \mathbf{F} = \begin{pmatrix} \bar{\rho}\tilde{v} \\ \bar{\rho}\tilde{u}\tilde{v} \\ \bar{\rho}\tilde{v}\tilde{v} + \tilde{p} \\ \bar{\rho}\tilde{w}\tilde{v} \\ (\bar{\rho}\tilde{e} + \tilde{p})\tilde{v} \end{pmatrix}, \mathbf{G} = \begin{pmatrix} \bar{\rho}w \\ \bar{\rho}\tilde{u}\tilde{w} \\ \bar{\rho}\tilde{v}\tilde{w} \\ \bar{\rho}\tilde{w}\tilde{w} + \tilde{p} \\ (\bar{\rho}\tilde{e} + \tilde{p})\tilde{w} \end{pmatrix},$$

The $\mathbf{E}''$, $\mathbf{F}''$, and $\mathbf{G}''$ are the inviscid fluxes at the stationary grid system and are:

$$\mathbf{E}'' = \xi_x \mathbf{E} + \xi_y \mathbf{F} + \xi_z \mathbf{G},$$

$$\mathbf{F}'' = \eta_x \mathbf{E} + \eta_y \mathbf{F} + \eta_z \mathbf{G},$$

$$\mathbf{G}'' = \zeta_x \mathbf{E} + \zeta_y \mathbf{F} + \zeta_z \mathbf{G},$$

and the viscous flux vectors are given by

$$\mathbf{E}_{\mathbf{v}} = \begin{pmatrix} 0 \\ \bar{\tau}_{xx} - \overline{\rho u'' u''} \\ \bar{\tau}_{xy} - \overline{\rho u'' v''} \\ \bar{\tau}_{xz} - \overline{\rho u'' w''} \\ Q_x \end{pmatrix}, \mathbf{F}_{\mathbf{v}} = \begin{pmatrix} 0 \\ \bar{\tau}_{yx} - \overline{\rho v'' u''} \\ \bar{\tau}_{yy} - \overline{\rho v'' v''} \\ \bar{\tau}_{yz} - \overline{\rho v'' w''} \\ Q_y \end{pmatrix}, \mathbf{G}_{\mathbf{v}} = \begin{pmatrix} 0 \\ \bar{\tau}_{zx} - \overline{\rho w'' u''} \\ \bar{\tau}_{zy} - \overline{\rho w'' v''} \\ \bar{\tau}_{zz} - \overline{\rho w'' w''} \\ Q_z \end{pmatrix}$$

In above equations, ρ is the density, u, v, and w are the Cartesian velocity components in x, y and z directions, p is the static pressure, and e is the total energy per unit mass. The overbar denotes the Reynolds-averaged quantity, tilde and double-prime denote the Favre mean and Favre fluctuating part of the turbulent motion respectively. All the flow variable in above equations are non-dimensionlized by using the freestream quantities and a reference length L.

Let subscript 1, 2 and 3 represent the coordinates, x, y, and z, and use Einstein summation convention, the shear-stress and Q_x, Q_y, Q_z terms in non-dimensional forms can be expressed in tensor form as

$$\bar{\tau}_{ij} = -\frac{2}{3}\tilde{\mu}\frac{\partial \tilde{u}_k}{\partial x_k}\delta_{ij} + \tilde{\mu}(\frac{\partial \tilde{u}_i}{\partial x_j} + \frac{\partial \tilde{u}_j}{\partial x_i}) \tag{4.9}$$

$$Q_i = \tilde{u}_j(\bar{\tau}_{ij} - \overline{\rho u'' u''}) - (\bar{q}_i + C_p \overline{\rho T'' u''_i}) \tag{4.10}$$

where the mean molecular heat flux is

$$\bar{q}_i = -\frac{\tilde{\mu}}{(\gamma-1)Pr}\frac{\partial a^2}{\partial x_i} \tag{4.11}$$

The molecular viscosity $\tilde{\mu} = \tilde{\mu}(\tilde{T})$ is determined by Sutherland law, and $a = \sqrt{\gamma R T_\infty}$ is the speed of sound. The equation of state closes the system,

$$\bar{\rho}\tilde{e} = \frac{\tilde{p}}{(\gamma-1)} + \frac{1}{2}\bar{\rho}(\tilde{u}^2 + \tilde{v}^2 + \tilde{w}^2) + k \tag{4.12}$$

where γ is the ratio of specific heats, k is the Favre mass-averaged turbulence kinetic energy. The turbulent shear stresses and heat flux appeared in above equations are calculated by Baldwin-Lomax model[48]. The viscosity is composed of $\mu + \mu_t$, where μ is the molecular viscosity and μ_t is the turbulent viscosity determined by Baldwin Lomax model. For a laminar flow, the μ_t is set to be zero.

4.2 Time Marching Scheme

The time dependent governing equation (4.1) is solved using the control volume method with the concept of dual time stepping suggested by Jameson [49]. A pseudo temporal term $\frac{\partial \mathbf{Q}}{\partial \tau}$ is added to the governing equation (4.1). This term vanishes at the end of each physical time step, and has no influence on the accuracy of the solution. However, instead of using the explicit scheme as in [49], an implicit pseudo time marching scheme using line Gauss-Seidel iteration is employed to achieve high CPU efficiency. For unsteady time accurate computations, the temporal term is discretized implicitly using a three point, backward differencing as the following

$$\frac{\partial \mathbf{Q}}{\partial t} = \frac{3Q^{n+1} - 4Q^n + Q^{n-1}}{2\Delta t} \tag{4.13}$$

Where n is the time level index. The pseudo temporal term is discretized with first order Euler scheme. Let m stand for the iteration index within a physical time step, the semi-discretized governing equation (4.1) can be expressed as

$$[(\frac{1}{\Delta\tau} + \frac{1.5}{\Delta t})I - (\frac{\partial R}{\partial Q})^{n+1,m}]\delta Q^{n+1,m+1} = R^{n+1,m} - \frac{3Q^{n+1,m} - 4Q^n + Q^{n-1}}{2\Delta t} \tag{4.14}$$

where the $\Delta\tau$ is the pseudo time step, R is the net flux going through the control volume,

$$R = -\frac{1}{V}\int_s [(E' - \frac{1}{Re}E'_v)\mathbf{i} + (F' - \frac{1}{Re}F'_v)\mathbf{j} + (G' - \frac{1}{Re}G'_v)\mathbf{k}]\cdot ds \tag{4.15}$$

where V is the volume of the control volume, s is the control volume surface area vector. Equation (4.14) is solved using the unfactored line Gauss-Seidel iteration. Two line sweeps in each pseudo time steps are used, one sweeps forward and the other sweeps backward. The alternative sweep directions are beneficial to the information propagation to reach high convergence rate. Within each physical time step, the solution marches in pseudo time until converged. The method is unconditionally stable and can reach very large pseudo time step since no factorization error is introduced.

4.3 The Zha E-CUSP Scheme[1, 2]

To clearly describe the formulations, the vectors $\mathbf{Q}$ and $\mathbf{E}'$ in Eq. (4.1) are given below:

$$\mathbf{Q} = \begin{pmatrix} \bar{\rho} \\ \bar{\rho}\tilde{u} \\ \bar{\rho}\tilde{v} \\ \bar{\rho}\tilde{w} \\ \bar{\rho}\tilde{e} \end{pmatrix}, \quad \mathbf{E}' = \frac{1}{J}\hat{\mathbf{E}}, \quad \hat{\mathbf{E}} = \begin{pmatrix} \bar{\rho}\tilde{U} \\ \bar{\rho}\tilde{u}\tilde{U} + \xi_x\tilde{p} \\ \bar{\rho}\tilde{v}\tilde{U} + \xi_y\tilde{p} \\ \bar{\rho}\tilde{w}\tilde{U} + \xi_z\tilde{p} \\ \bar{\rho}\tilde{e}\tilde{U} + \tilde{p}\tilde{U} \end{pmatrix} \tag{4.16}$$

$\tilde{U}$ is the contravariant velocity in ξ direction and is defined as the following:

$$\tilde{U} = \xi_t + \xi_x\tilde{u} + \xi_y\tilde{v} + \xi_z\tilde{w} \tag{4.17}$$

$\bar{U}$ is defined as:

$$\bar{U} = \tilde{U} - \xi_t \tag{4.18}$$

The Jacobian matrix $\hat{\mathbf{A}}$ is defined as:

$$\hat{\mathbf{A}} = \frac{\partial\hat{\mathbf{E}}}{\partial\mathbf{Q}} = \hat{\mathbf{T}}\hat{\mathbf{\Lambda}}\hat{\mathbf{T}}^{-1} \tag{4.19}$$

where $\hat{\mathbf{T}}$ is the right eigenvector matrix of $\hat{\mathbf{A}}$, and $\hat{\mathbf{\Lambda}}$ is the eigenvalue matrix of $\hat{\mathbf{A}}$ on the moving grid system with the eigenvalues of:

$$(\tilde{U} + \tilde{C}, \tilde{U} - \tilde{C}, \tilde{U}, \tilde{U}, \tilde{U}) \tag{4.20}$$

where $\tilde{C}$ is the speed of sound corresponding to the contravariant velocity:

$$\tilde{C} = c\sqrt{\xi_x^2 + \xi_y^2 + \xi_z^2} \tag{4.21}$$

and where $c = \sqrt{\gamma RT}$ is the physical speed of sound.

Due to the homogeneous relationship between $\mathbf{Q}$ and $\hat{\mathbf{E}}$, the following formulation applies:

$$\hat{\mathbf{E}} = \hat{\mathbf{A}}\mathbf{Q} = \hat{\mathbf{T}}\hat{\mathbf{\Lambda}}\hat{\mathbf{T}}^{-1}\mathbf{Q} \tag{4.22}$$

In an E-CUSP scheme, the eigenvalue matrix is split as the following:

$$\hat{\mathbf{\Lambda}} = \begin{pmatrix} \tilde{U}-\tilde{C} & 0 & 0 & 0 & 0 \\ 0 & \tilde{U} & 0 & 0 & 0 \\ 0 & 0 & \tilde{U} & 0 & 0 \\ 0 & 0 & 0 & \tilde{U} & 0 \\ 0 & 0 & 0 & 0 & \tilde{U}+\tilde{C} \end{pmatrix} = \tilde{U}[\mathbf{I}] + \begin{pmatrix} -\tilde{C} & 0 & 0 & 0 & 0 \\ 0 & 0 & 0 & 0 & 0 \\ 0 & 0 & 0 & 0 & 0 \\ 0 & 0 & 0 & 0 & 0 \\ 0 & 0 & 0 & 0 & \tilde{C} \end{pmatrix} \tag{4.23}$$

The grid velocity term $\xi_t[\mathbf{I}]$ due to the moving mesh is naturally included in the convective term, $\tilde{U}$, as given in Eq. (4.43). Therefore, Eq. (4.22) becomes:

$$\begin{aligned} \hat{\mathbf{E}} = \hat{\mathbf{T}}\{\tilde{U}[\mathbf{I}] + \begin{pmatrix} -\tilde{C} & 0 & 0 & 0 & 0 \\ 0 & 0 & 0 & 0 & 0 \\ 0 & 0 & 0 & 0 & 0 \\ 0 & 0 & 0 & 0 & 0 \\ 0 & 0 & 0 & 0 & \tilde{C} \end{pmatrix}\}\hat{\mathbf{T}}^{-1}\mathbf{Q} &= \hat{\mathbf{E}}^c + \hat{\mathbf{E}}^p \\ &= \begin{pmatrix} \bar{\rho}\tilde{U} \\ \bar{\rho}\tilde{u}\tilde{U} \\ \bar{\rho}\tilde{v}\tilde{U} \\ \bar{\rho}\tilde{w}\tilde{U} \\ \bar{\rho}\tilde{e}\tilde{U} \end{pmatrix} + \begin{pmatrix} 0 \\ \xi_x\tilde{p} \\ \xi_y\tilde{p} \\ \xi_z\tilde{p} \\ \tilde{p}\tilde{U} \end{pmatrix} \end{aligned} \tag{4.24}$$

where $\hat{\mathbf{E}}^c$ and $\hat{\mathbf{E}}^p$ are namely the convective and pressure fluxes. As shown above, the way of splitting the total flux into convective and pressure fluxes in an E-CUSP scheme is purely based on the analysis of characteristics of the system. As shown in Eq. (4.24), the convective flux has the upwind characteristic $\tilde{U}$ and is only associated with the convective velocity. The pressure flux has a downwind and an upwind characteristic and it completely depends on the propagation of an acoustic wave.

The Zha E-CUSP2 scheme is based on the E-CUSP scheme suggested by Zha and Hu [1], which is extended to a moving mesh system by the following:

$$\hat{\mathbf{E}}_{\frac{1}{2}} = \frac{1}{2}[(\bar{\rho}\tilde{U})_{\frac{1}{2}}(\mathbf{q^c}_L + \mathbf{q^c}_R) - |\bar{\rho}\tilde{U}|_{\frac{1}{2}}(\mathbf{q^c}_R - \mathbf{q^c}_L)] + \begin{pmatrix} 0 \\ P^+\tilde{p}\xi_x \\ P^+\tilde{p}\xi_y \\ P^+\tilde{p}\xi_z \\ \frac{1}{2}\tilde{p}(\bar{U} + \bar{C}_{\frac{1}{2}}) \end{pmatrix}_L + \begin{pmatrix} 0 \\ P^-\tilde{p}\xi_x \\ P^-\tilde{p}\xi_y \\ P^-\tilde{p}\xi_z \\ \frac{1}{2}\tilde{p}(\bar{U} - \bar{C}_{\frac{1}{2}}) \end{pmatrix}_R \tag{4.25}$$

where

$$(\bar{\rho}\tilde{U})_{\frac{1}{2}} = (\bar{\rho}_L\tilde{U}_L^+ + \bar{\rho}_R\tilde{U}_R^-) \tag{4.26}$$

$$\mathbf{q^c} = \begin{pmatrix} 1 \\ \tilde{u} \\ \tilde{v} \\ \tilde{w} \\ \tilde{e} \end{pmatrix} \tag{4.27}$$

$$\tilde{C}_{\frac{1}{2}} = \frac{1}{2}(\tilde{C}_L + \tilde{C}_R) \tag{4.28}$$

$$\tilde{M}_L = \frac{\tilde{U}_L}{\tilde{C}_{\frac{1}{2}}}, \quad \tilde{M}_R = \frac{\tilde{U}_R}{\tilde{C}_{\frac{1}{2}}} \tag{4.29}$$

$$\tilde{U}_L^+ = \tilde{C}_{\frac{1}{2}}\{\frac{\tilde{M}_L + |\tilde{M}_L|}{2} + \alpha_L[\frac{1}{4}(\tilde{M}_L + 1)^2 - \frac{\tilde{M}_L + |\tilde{M}_L|}{2}]\} \tag{4.30}$$

$$\tilde{U}_R^- = \tilde{C}_{\frac{1}{2}}\{\frac{\tilde{M}_R - |\tilde{M}_R|}{2} + \alpha_R[-\frac{1}{4}(\tilde{M}_R - 1)^2 - \frac{\tilde{M}_R - |\tilde{M}_R|}{2}]\} \tag{4.31}$$

$$\alpha_L = \frac{2(\tilde{p}/\bar{\rho})_L}{(\tilde{p}/\bar{\rho})_L + (\tilde{p}/\bar{\rho})_R}, \quad \alpha_R = \frac{2(\tilde{p}/\bar{\rho})_R}{(\tilde{p}/\bar{\rho})_L + (\tilde{p}/\bar{\rho})_R} \tag{4.32}$$

$$P^{\pm} = \frac{1}{4}(\tilde{M} \pm 1)^2(2 \mp \tilde{M}) \pm \alpha\tilde{M}(\tilde{M}^2 - 1)^2, \quad \alpha = \frac{3}{16} \tag{4.33}$$

$$\bar{C} = \tilde{C} - \xi_t \tag{4.34}$$

$$\bar{C}_{\frac{1}{2}} = \frac{1}{2}(\bar{C}_L + \bar{C}_R) \tag{4.35}$$

Please note that, in the energy equation of the pressure splitting, $\bar{U}$ and $\bar{C}$ are used instead of $\tilde{U}$ and $\tilde{C}$. The term $\bar{C}$ is constructed by taking into account the effect of the grid velocity so that the flux will transit from subsonic to supersonic smoothly. When $\xi_t = 0$, Eq. (4.25) naturally returns to the one for a stationary grid.

For supersonic flow, when $\tilde{U}_L \geq \tilde{C}$, $\hat{\mathbf{E}}_{\frac{1}{2}} = \hat{\mathbf{E}}_L$; when $\tilde{U}_R \leq -\tilde{C}$, $\hat{\mathbf{E}}_{\frac{1}{2}} = \hat{\mathbf{E}}_R$.

4.3.1 Numerical Dissipation

The low numerical dissipation at stagnation is important to accurately resolve wall boundary layers. An upwind scheme can be written as a central differencing plus a numerical dissipation.

To analyze the numerical dissipation at stagnation, the 1D Euler equation is used as the example. Assuming $u = 0$, the numerical dissipation vector of the new E-CUSP scheme at stagnation is:

$$\mathbf{D} = -\frac{a_{\frac{1}{2}}}{2}\begin{pmatrix} 0 \\ 0 \\ \delta p \end{pmatrix} \tag{4.36}$$

where

$$\delta p = p_R - p_L \tag{4.37}$$

The numerical dissipation of the Roe scheme at stagnation is:

$$\mathbf{D}_{Roe} = -\frac{\tilde{a}_{\frac{1}{2}}}{2(\gamma - 1)}\begin{pmatrix} (\gamma - 1)/\tilde{a}^2_{\frac{1}{2}}\delta p \\ 0 \\ \delta p \end{pmatrix} \tag{4.38}$$

where the ˜ stands for the Roe's average[50].

Comparing eq.(4.36) and (4.38), it can be seen that the numerical dissipation of the new E-CUSP scheme for the continuity equation vanishes at $u = 0$ while the Roe scheme has the non-vanishing dissipation. For the energy equation, the two schemes have equivalent dissipation. For ideal gas with the $\gamma = 1.4$, the coefficient of the Roe scheme energy dissipation term is 2.5 times larger than that of the new E-CUSP scheme.

In conclusion, even though there is one non-vanishing numerical dissipation term in the energy equation for the new E-CUSP scheme, the overall numerical dissipation

of the new E-CUSP scheme is not greater than that of the Roe scheme. The Roe scheme is proved to be accurate to resolve wall boundary layers[51]. It is hence expected that the new E-CUSP scheme should also have sufficiently low dissipation to accurately resolve wall boundary layers. This is indeed the case shown by the numerical experiment for a flat plate boundary layer.

4.3.2 Zha E-CUSP2 Scheme[3]

The original Zha-Hu scheme is proved to have low diffusion and is able to capture crisp shock wave profile and exact contact surface[1]. However, the scheme is found to have temperature oscillations near the solid wall region when the grids is skewed. Therefore, the scheme used in the present study is the modified version scheme, Zha CUSP2 scheme[52]. In this scheme, the total enthalpy instead of the static pressure is used to calculate the numerical dissipation coefficients for the energy equation as below:

$$\alpha_L = \frac{2(\tilde{H}/\bar{\rho})_L}{(\tilde{H}/\bar{\rho})_L + (\tilde{H}/\bar{\rho})_R}, \quad \alpha_R = \frac{2(\tilde{H}/\bar{\rho})_R}{(\tilde{H}/\bar{\rho})_L + (\tilde{H}/\bar{\rho})_R} \tag{4.39}$$

Note that Equation (4.39) is only used for the energy equation. For the continuity and momentum equations, Equation (4.32) is still used as the smoothing coefficient.

4.4 Roe's Riemann Solver on Moving Grid System[4, 5]

The Roe's Riemann solver is also implemented in the solver as a benchmark scheme to compare the results. Roe scheme is recognized as having very low diffusion and can capture exact shock and contact discontinuities. In present study, the original Roe scheme is extended to moving grid system as the following, for example, in ξ direction:

$$\mathbf{E}'_{i+\frac{1}{2}} = \frac{1}{2J}[\mathbf{E}''(\mathbf{Q_L}) + \mathbf{E}''(\mathbf{Q_R}) + \mathbf{Q_L}\xi_{tL} + \mathbf{Q_R}\xi_{tR} - |\tilde{\mathbf{A}}|(\mathbf{Q_R} - \mathbf{Q_L})]_{i+\frac{1}{2}} \tag{4.40}$$

where $\mathbf{Q_L}$ and $\mathbf{Q_R}$ are the reconstructed variables to the left and right sides of the cell face, ξ_{tL} and ξ_{tR} are the reconstructed grid velocity component in ξ direction to the left and right sides of the cell interface $i + \frac{1}{2}$, $\mathbf{A}$ is the Jacobian matrix, $\mathbf{A} = \frac{\partial \mathbf{E}'}{\partial \mathbf{Q}}$ and it takes the form as $\mathbf{A} = \mathbf{T}\mathbf{\Lambda}\mathbf{T}^{-1}$, $\mathbf{T}$ is the right eigenvector matrix of $\mathbf{A}$, $\mathbf{\Lambda}$ is the eigenvalue matrix of $\mathbf{A}$, and

$$\tilde{\mathbf{A}} = \tilde{\mathbf{T}}\tilde{\mathbf{\Lambda}}\tilde{\mathbf{T}}^{-1} \tag{4.41}$$

where $\tilde{\mathbf{\Lambda}}$ is the eigenvalue matrix on moving grid system with the eigenvalues of

$$(\tilde{U} + \tilde{C}, \tilde{U} - \tilde{C}, \tilde{U}, \tilde{U}, \tilde{U}) \tag{4.42}$$

where $\tilde{U}$ is the contravariant velocity in ξ direction on moving grid,

$$\tilde{U} = \tilde{\xi}_t + \xi_x\tilde{u} + \xi_y\tilde{v} + \xi_z\tilde{w} \tag{4.43}$$

$\tilde{C}$ is the speed of sound corresponding to the contravariant velocity:

$$\tilde{C} = \tilde{c}\sqrt{\xi_x^2 + \xi_y^2 + \xi_z^2} \tag{4.44}$$

where $c = \sqrt{\gamma RT}$ is the physical speed of sound. The $\sim$ stands for the Roe-averaged quantities. For example,

$$\tilde{\xi}_t = (\xi_{tL} + \xi_{tR}\sqrt{\rho_R/\rho_L})/(1 + \sqrt{\rho_R/\rho_L}) \tag{4.45}$$

It can be proved that the eigenvector matrix $\mathbf{T}$ has exactly the same form as the one without moving grid. The only difference between the moving grid and the stationary grid system is that, for the moving grid system, the contravariant velocity in the eigenvalues contains the grid velocity as given in Equation (4.43). It is hence straightforward to extend the code from a stationary grid system to the moving grid system using Roe scheme without major change.

The grid velocity is evaluated at the center of each cell and is determined by the averaged value that counts the movement of the eight vertexes if hexahedral control volumes are used. The grid velocity is reconstructed with 3rd order MUSCL differencing.

4.5 Conventional Boundary Conditions

Two sets of boundary conditions are developed in this research. The first set is the conventional boundary conditions. The second set is the non-reflective boundary conditions to be described in Chapter 5.

The conventional boundary conditions used for both the steady state and unsteady calculation are as follows:

(1) Inlet boundary conditions: The far field boundary is divided into inlet and outlet boundaries. On inlet boundary, it is assumed that the streamwise velocity u

is uniform, transverse velocity $v = 0$, and spanwise velocity $w = 0$. Other primitive variables are specified according to the freestream condition except the pressure which is extrapolated from interior.

(2) Outlet boundary conditions: All the flow quantities are extrapolated from interior except the pressure which is set to be its freestream value.

(3) Solid wall boundary conditions: At moving boundary surface, the no-slip condition is enforced by extrapolating the velocity between the phantom and interior cells,

$$u_0 = 2\dot{x}_b - u_1, \qquad v_0 = 2\dot{y}_b - v_1, \qquad w_0 = 2\dot{z}_b - w_1 \tag{4.46}$$

where u_0, v_0 and w_0 denote the velocity at phantom cell, u_1, v_1 and w_1 denote the velocity at the $1st$ interior cell close to the boundary, and u_b, v_b and w_b are the velocity on the moving boundary.

If the wall surface is in η direction, the other two conditions to be imposed on the solid wall are the adiabatic wall condition and the inviscid normal momentum equation[30] as follows,

$$\frac{\partial T}{\partial \eta} = 0, \quad \frac{\partial p}{\partial \eta} = -\left(\frac{\rho}{\eta_x^2 + \eta_y^2 + \eta_z^2}\right)(\eta_x \ddot{x}_b + \eta_y \ddot{y}_b + \eta_z \ddot{z}_b) \tag{4.47}$$

4.6 Moving/Deforming Grid Systems

In the fully-coupled computation, the remeshing is performed in each iteration. Therefore, a CPU time efficient algebraic grid deformation method is employed in the computation instead of the commonly-used grid generation method in which the Poisson equation is solved for grid points. For clarity, the remeshing procedure for 2D cases is sketched in Figure 12.131. This grid deformation procedure is designed in such a way that the far-field boundary (j=jlp) is held fixed, and the grids on the wing surface (j=1) moves and deforms following the instantaneous motion of the wing structure. After the new wing surface is determined, two components of the displacement vector at wing surface node dx_1 and dy_1 can be calculated accordingly. First, the length of each segment along the old mesh line is estimated as:

$$s_j = s_{j-1} + \sqrt{(x_j - x_{j-1})^2 + (y_j - y_{j-1})^2} \qquad (j = 2, \cdots, jlp) \tag{4.48}$$

where $s_1 = 0$ and the displacement vectors at wing surface node (dx_1, dy_1) and at the far-field boundary (dx_{jlp}, $dy_j lp$) are known. Then the grid node points between the wing surface and the far-field boundary can be obtained by using following linear interpolation:

$$dx_j = \frac{dx_{jlp} - dx_1}{s_{jlp} - s_1} s_j + \frac{dx_1 s_{jlp} - dx_{jlp} s_1}{s_{jlp} - s_1} \tag{4.49}$$

$$dy_j = \frac{dy_{jlp} - dy_1}{s_{jlp} - s_1} s_j + \frac{dy_1 s_{jlp} - dy_{jlp} s_1}{s_{jlp} - s_1} \tag{4.50}$$

This simple remeshing strategy is proved to be robust for all the cases investigated in present study. By monitoring the accuracy criterion y^+, it is shown that the method can maintain the initial grid quality and keep almost the same mesh distribution around the wing surface.

For 3D case, the Equation (4.51) becomes

$$s_j = s_{j-1} + \sqrt{(x_j - x_{j-1})^2 + (y_j - y_{j-1})^2 + (z_j - z_{j-1})^2} \qquad (j = 2, \cdots, jlp) \tag{4.51}$$

and one more equation is added to determined the z component of displacement vector:

$$dz_j = \frac{dz_{jlp} - dz_1}{s_{jlp} - s_1} s_j + \frac{dz_1 s_{jlp} - dz_{jlp} s_1}{s_{jlp} - s_1} \tag{4.52}$$

4.7 Geometric Conservation Law

It was pointed out by Thomas et al.[53] that due to the mixed temporal and spatial derivatives after discretization, an additional term appears, which theoretically equals to zero but numerically still remains. Consequently numerical error could be introduced in the discretized form of the equations of the flow motion if this term is neglected. In order to reduce or avoid this error, the geometric conservation law needs to be enforced. In other words, the following additional term should be added to the right-hand side of the equations as a source term:

$$\mathbf{S} = \mathbf{Q}\left[\frac{\partial J^{-1}}{\partial t} + \left(\frac{\xi_t}{J}\right)_\xi + \left(\frac{\eta_t}{J}\right)_\eta + \left(\frac{\zeta_t}{J}\right)_\zeta\right] \tag{4.53}$$

To implement this option in the flow solver, the source term is then linearized such that

$$\mathbf{S}^{n+1} = \mathbf{S}^n + \frac{\partial \mathbf{S}}{\partial \mathbf{Q}} \Delta \mathbf{Q}^{n+1} \tag{4.54}$$

As has been observed in ref.[5], the overall performance of this numerical supplement is beneficial with very little CPU time cost.

Chapter 5

Non-Reflective Boundary Conditions

5.1 Characteristic Form of the Navier-Stokes Equations[6]

The characteristic form of the Navier-Stokes equations in the generalized coordinates will be solved to determine the non-reflective boundary conditions at the phantom cells. To describe the derivation process, the ξ direction will be taken as an example. For the other two directions, the formulations can follow the same procedure and the general formulations are given in the appendix. Based on the strategy of Thompson[39] and Poinsot and Lele[33], the Navier-Stokes equations are expressed first using primitive variables as the following:

$$\mathbf{M}\frac{\partial \mathbf{q}}{\partial t} + \mathbf{A}\cdot\mathbf{M}\frac{\partial \mathbf{q}}{\partial \xi} + \mathbf{B}\cdot\mathbf{M}\frac{\partial \mathbf{q}}{\partial \eta} + \mathbf{C}\cdot\mathbf{M}\frac{\partial \mathbf{q}}{\partial \zeta} = \mathbf{R_v} \tag{5.1}$$

where $\mathbf{A}, \mathbf{B}, \mathbf{C}$ are the Jacobian matrix

$$\mathbf{A} = \frac{\partial \mathbf{E}'}{\partial \mathbf{Q}'}, \mathbf{B} = \frac{\partial \mathbf{F}'}{\partial \mathbf{Q}'}, \mathbf{C} = \frac{\partial \mathbf{G}'}{\partial \mathbf{Q}'} \tag{5.2}$$

where $\mathbf{R_v}$ is the viscous vector on the right hand side of the Navier-Stokes equations, (Equation (4.1)), $\mathbf{q}$ is the primitive variable vector:

$$\mathbf{q} = \frac{1}{J}\begin{pmatrix} \rho \\ u \\ v \\ w \\ p \end{pmatrix} \tag{5.3}$$

$\mathbf{M}$ is the Jacobian matrix between the conservative variables and primitive variables

$$\mathbf{M} = \frac{\partial \mathbf{Q}'}{\partial \mathbf{q}} = \begin{pmatrix} 1 & 0 & 0 & 0 & 0 \\ u & \rho & 0 & 0 & 0 \\ v & 0 & \rho & 0 & 0 \\ w & 0 & 0 & \rho & 0 \\ \frac{\Phi}{\gamma-1} & \rho u & \rho v & \rho w & \frac{1}{\gamma-1} \end{pmatrix} \tag{5.4}$$

where $\Phi = \frac{\gamma-1}{2}(u^2 + v^2 + w^2)$.

Equation (5.1) can be further expressed as:

$$\frac{\partial \mathbf{q}}{\partial t} + \mathbf{a}\frac{\partial \mathbf{q}}{\partial \xi} + \mathbf{b}\frac{\partial \mathbf{q}}{\partial \eta} + \mathbf{c}\frac{\partial \mathbf{q}}{\partial \zeta} = \mathbf{M}^{-1}\mathbf{R_v} \tag{5.5}$$

Where

$$\mathbf{a} = \mathbf{M}^{-1}\mathbf{A}\mathbf{M}, \mathbf{b} = \mathbf{M}^{-1}\mathbf{B}\mathbf{M}, \mathbf{c} = \mathbf{M}^{-1}\mathbf{C}\mathbf{M} \tag{5.6}$$

$$\mathbf{M}^{-1} = \begin{pmatrix} 1 & 0 & 0 & 0 & 0 \\ -\frac{u}{\rho} & \frac{1}{\rho} & 0 & 0 & 0 \\ -\frac{v}{\rho} & 0 & \frac{1}{\rho} & 0 & 0 \\ -\frac{w}{\rho} & 0 & 0 & \frac{1}{\rho} & 0 \\ \Phi & -u(\gamma-1) & -v(\gamma-1) & -w(\gamma-1) & \gamma-1 \end{pmatrix} \tag{5.7}$$

Matrix $\mathbf{a}, \mathbf{b}, \mathbf{c}$ have the same eigenvalues as Jacobian matrix $\mathbf{A}, \mathbf{B}, \mathbf{C}$. In ξ direction,

$$\mathbf{a} = \begin{pmatrix} U & \rho\xi_x & \rho\xi_y & \rho\xi_z & 0 \\ 0 & U & 0 & 0 & \frac{\xi_x}{\rho} \\ 0 & 0 & U & 0 & \frac{\xi_y}{\rho} \\ 0 & 0 & 0 & U & \frac{\xi_z}{\rho} \\ 0 & \gamma p\xi_x & \gamma p\xi_y & \gamma p\xi_z & U \end{pmatrix} \tag{5.8}$$

where $U = \xi_x u + \xi_y v + \xi_z w$. Matrix $\mathbf{a}$ can also be expressed as

$$\mathbf{a} = \mathbf{P}\mathbf{\Lambda}\mathbf{P}^{-1} \tag{5.9}$$

where $\mathbf{\Lambda}$ is the eigenvalue matrix, $\mathbf{P}$ is eigenvector matrix of $\mathbf{a}$, and $\mathbf{P}^{-1}$ is the inverse of $\mathbf{P}$. They are given as the following

$$\mathbf{\Lambda} = \begin{pmatrix} U & 0 & 0 & 0 & 0 \\ 0 & U & 0 & 0 & 0 \\ 0 & 0 & U & 0 & 0 \\ 0 & 0 & 0 & U+C & 0 \\ 0 & 0 & 0 & 0 & U-C \end{pmatrix} \tag{5.10}$$

$$\mathbf{P} = \begin{pmatrix} \tilde{\xi}_x & \tilde{\xi}_y & \tilde{\xi}_z & \alpha & \alpha \\ 0 & -\tilde{\xi}_z & \tilde{\xi}_y & \tilde{\xi}_x/\sqrt{2} & -\tilde{\xi}_x/\sqrt{2} \\ \tilde{\xi}_z & 0 & -\tilde{\xi}_x & \tilde{\xi}_y/\sqrt{2} & -\tilde{\xi}_y/\sqrt{2} \\ -\tilde{\xi}_y & \tilde{\xi}_x & 0 & \tilde{\xi}_z/\sqrt{2} & -\tilde{\xi}_z/\sqrt{2} \\ 0 & 0 & 0 & \alpha c^2 & \alpha c^2 \end{pmatrix} \tag{5.11}$$

$$\mathbf{P}^{-1} = \begin{pmatrix} \tilde{\xi}_x & 0 & \tilde{\xi}_z & -\tilde{\xi}_y & -\tilde{\xi}_x/c^2 \\ \tilde{\xi}_y & -\tilde{\xi}_z & 0 & \tilde{\xi}_x & -\tilde{\xi}_y/c^2 \\ \tilde{\xi}_z & \tilde{\xi}_y & -\tilde{\xi}_x & 0 & -\tilde{\xi}_z/c^2 \\ 0 & \tilde{\xi}_x/\sqrt{2} & \tilde{\xi}_y/\sqrt{2} & \tilde{\xi}_z/\sqrt{2} & \beta \\ 0 & -\tilde{\xi}_x/\sqrt{2} & -\tilde{\xi}_y/\sqrt{2} & -\tilde{\xi}_z/\sqrt{2} & \beta \end{pmatrix} \tag{5.12}$$

where $C = c|\nabla\xi|$, $|\nabla\xi| = \sqrt{{\xi_x}^2 + {\xi_y}^2 + {\xi_z}^2}$, $\tilde{\xi}_x = \xi_x/|\nabla\xi|$, $\tilde{\xi}_y = \xi_y/|\nabla\xi|$, $\tilde{\xi}_z = \xi_z/|\nabla\xi|$, $\alpha = \rho/\sqrt{2}c$, $\beta = 1/\sqrt{2}\rho c$, c is the speed of sound and determined by $c = \sqrt{\gamma RT}$.

The Navier-Stokes equation, Equation (5.5) then can be expressed as:

$$\frac{\partial \mathbf{q}}{\partial t} + \mathbf{P}\mathbf{\Lambda}\mathbf{P}^{-1}\frac{\partial \mathbf{q}}{\partial \xi} + \mathbf{b}\frac{\partial \mathbf{q}}{\partial \eta} + \mathbf{c}\frac{\partial \mathbf{q}}{\partial \zeta} = \mathbf{M}^{-1}\mathbf{R}_v \tag{5.13}$$

or

$$\mathbf{P}^{-1}\frac{\partial \mathbf{q}}{\partial t} + \mathbf{\Lambda}\mathbf{P}^{-1}\frac{\partial \mathbf{q}}{\partial \xi} + \mathbf{P}^{-1}\mathbf{b}\frac{\partial \mathbf{q}}{\partial \eta} + \mathbf{P}^{-1}\mathbf{c}\frac{\partial \mathbf{q}}{\partial \zeta} = \mathbf{P}^{-1}\mathbf{M}^{-1}\mathbf{R}_v \tag{5.14}$$

This is the characteristic form of the Navier-Stokes equations in ξ direction. Define vector $\mathcal{L}$ as:

$$\mathcal{L} = \mathbf{\Lambda}\mathbf{P}^{-1}\frac{\partial \mathbf{q}}{\partial \xi} \tag{5.15}$$

The Navier-Stokes equations (Equation (5.14)) are then expressed as:

$$\mathbf{P}^{-1}\frac{\partial \mathbf{q}}{\partial t} + \mathcal{L} + \mathbf{P}^{-1}\mathbf{b}\frac{\partial \mathbf{q}}{\partial \eta} + \mathbf{P}^{-1}\mathbf{c}\frac{\partial \mathbf{q}}{\partial \zeta} = \mathbf{P}^{-1}\mathbf{M}^{-1}\mathbf{R}_v \tag{5.16}$$

Vector $\mathcal{L}$ is given as the following:

$$\mathcal{L} = \begin{pmatrix} \mathcal{L}_1 \\ \mathcal{L}_2 \\ \mathcal{L}_3 \\ \mathcal{L}_4 \\ \mathcal{L}_5 \end{pmatrix} = \begin{pmatrix} U[\tilde{\xi}_x \frac{\partial}{\partial \xi}(\frac{\rho}{J}) + \tilde{\xi}_z \frac{\partial}{\partial \xi}(\frac{v}{J}) - \tilde{\xi}_y \frac{\partial}{\partial \xi}(\frac{w}{J}) - \frac{\tilde{\xi}_x}{c^2}\frac{\partial}{\partial \xi}(\frac{p}{J})] \\ U[\tilde{\xi}_y \frac{\partial}{\partial \xi}(\frac{\rho}{J}) - \tilde{\xi}_z \frac{\partial}{\partial \xi}(\frac{u}{J}) + \tilde{\xi}_x \frac{\partial}{\partial \xi}(\frac{w}{J}) - \frac{\tilde{\xi}_y}{c^2}\frac{\partial}{\partial \xi}(\frac{p}{J})] \\ U[\tilde{\xi}_z \frac{\partial}{\partial \xi}(\frac{\rho}{J}) + \tilde{\xi}_y \frac{\partial}{\partial \xi}(\frac{u}{J}) - \tilde{\xi}_x \frac{\partial}{\partial \xi}(\frac{v}{J}) - \frac{\tilde{\xi}_z}{c^2}\frac{\partial}{\partial \xi}(\frac{p}{J})] \\ (U+C)[\frac{\tilde{\xi}_x}{\sqrt{2}}\frac{\partial}{\partial \xi}(\frac{u}{J}) + \frac{\tilde{\xi}_y}{\sqrt{2}}\frac{\partial}{\partial \xi}(\frac{v}{J}) + \frac{\tilde{\xi}_z}{\sqrt{2}}\frac{\partial}{\partial \xi}(\frac{w}{J}) + \beta\frac{\partial}{\partial \xi}(\frac{p}{J})] \\ (U-C)[-\frac{\tilde{\xi}_x}{\sqrt{2}}\frac{\partial}{\partial \xi}(\frac{u}{J}) - \frac{\tilde{\xi}_y}{\sqrt{2}}\frac{\partial}{\partial \xi}(\frac{v}{J}) - \frac{\tilde{\xi}_z}{\sqrt{2}}\frac{\partial}{\partial \xi}(\frac{w}{J}) + \beta\frac{\partial}{\partial \xi}(\frac{p}{J})] \end{pmatrix} \tag{5.17}$$

The vector $\mathcal{L}$ is the amplitude of the characteristic waves. If assume $\tilde{\xi}_x = 1, \tilde{\xi}_y = \tilde{\xi}_z = 0$, Equation (5.17) returns to the corresponding formulations in x-direction of the Cartesian coordinates.

As pointed out in [38, 39], for multi-dimensional Navier-Stokes flow equations, Equation (5.14), the matrix $\mathbf{P^{-1}}$ can not be absorbed into the partial derivatives because the flow equations does not satisfy Pfaff's condition and the matrix can not be treated as constants. In other words, it is incorrect to express the characteristic form of the Navier-Stokes equations in the form given in [37] (page 2042) as:

$$\frac{\partial \mathbf{R}}{\partial t} + \mathbf{\Lambda}\frac{\partial \mathbf{R}}{\partial \xi} + = \mathbf{P^{-1}} S_v^* \tag{5.18}$$

The local one-dimensional wave amplitude defined in [37] following Equation (5.18) is therefore also erroneous.

To be consistent with the governing equations of the flow field within inner domain and facilitate programming, it is desirable to express Equation (5.16) in terms of conservative variables. Multiply Equation (5.16) by matrix $\mathbf{M} \cdot \mathbf{P}$, the characteristic Navier-Stokes equations expressed in terms of conservative variables in ξ direction is:

$$\frac{\partial \mathbf{Q}'}{\partial t} + \mathbf{MP}\mathcal{L} + \frac{\partial \mathbf{F}'}{\partial \eta} + \frac{\partial \mathbf{G}'}{\partial \zeta} = \frac{1}{Re}\left(\frac{\partial \mathbf{E}'_\mathbf{v}}{\partial \xi} + \frac{\partial \mathbf{F}'_\mathbf{v}}{\partial \eta} + \frac{\partial \mathbf{G}'_\mathbf{v}}{\partial \zeta}\right) \tag{5.19}$$

Define vector $\mathbf{d}$ as

$$\mathbf{d} = \mathbf{P}\mathcal{L} = \begin{pmatrix} d_1 \\ d_2 \\ d_3 \\ d_4 \\ d_5 \end{pmatrix} = \begin{pmatrix} \tilde{\xi}_x\mathcal{L}_1 + \tilde{\xi}_y\mathcal{L}_2 + \tilde{\xi}_z\mathcal{L}_3 + \alpha(\mathcal{L}_4 + \mathcal{L}_5) \\ -\tilde{\xi}_z\mathcal{L}_2 + \tilde{\xi}_y\mathcal{L}_3 + \frac{\tilde{\xi}_x}{\sqrt{2}}(\mathcal{L}_4 - \mathcal{L}_5) \\ \tilde{\xi}_z\mathcal{L}_1 - \tilde{\xi}_x\mathcal{L}_3 + \frac{\tilde{\xi}_y}{\sqrt{2}}(\mathcal{L}_4 - \mathcal{L}_5) \\ -\tilde{\xi}_y\mathcal{L}_1 - \tilde{\xi}_x\mathcal{L}_2 + \frac{\tilde{\xi}_z}{\sqrt{2}}(\mathcal{L}_4 - \mathcal{L}_5) \\ \alpha c^2(\mathcal{L}_4 + \mathcal{L}_5) \end{pmatrix} \tag{5.20}$$

Define vector $\mathcal{D}$ as:

$$\mathcal{D} = \mathbf{M}\mathbf{d} = \begin{pmatrix} d_1 \\ ud_1 + \rho d_2 \\ vd_1 + \rho d_3 \\ wd_1 + \rho d_4 \\ \frac{1}{2}(u^2+v^2+w^2)d_1 + \rho u d_2 + \rho v d_3 + \rho w d_4 + \frac{1}{\gamma-1} d_5 \end{pmatrix} \tag{5.21}$$

Finally the characteristic form Navier-Stokes equations in conservative form and generalized coordinates in ξ direction can be expressed as:

$$\frac{\partial \mathbf{Q}'}{\partial t} + \mathcal{D} + \frac{\partial \mathbf{F}'}{\partial \eta} + \frac{\partial \mathbf{G}'}{\partial \zeta} = \frac{1}{Re}\left(\frac{\partial \mathbf{E}'_{\mathbf{v}}}{\partial \xi} + \frac{\partial \mathbf{F}'_{\mathbf{v}}}{\partial \eta} + \frac{\partial \mathbf{G}'_{\mathbf{v}}}{\partial \zeta}\right) \tag{5.22}$$

Equation (5.22) will be solved to determine the non-reflective boundary conditions in ξ direction. The Navier-Stokes equations in generalized coordinates and their characteristic forms in η and ζ directions can be obtained straightforwardly following the symmetric rule and are given in the appendix.

By neglecting the transverse and viscous terms in Equation (5.22), the Local One-Dimensional Inviscid (LODI) relation [33] in generalized coordinates is

$$\frac{\partial \mathbf{Q}'}{\partial t} + \mathcal{D} = 0 \tag{5.23}$$

The LODI relation may be used to estimate the amplitudes of the characteristic waves at boundaries. Numerical results show that the LODI relations works well for the boundaries where the flow fields are smooth or uniform, and hence the transverse and viscous terms are small or negligible. For those boundaries where the transverse and viscous terms are significant, the LODI relations may perform poorly.

5.2 Non-Reflective Boundary Conditions[6]

Following the strategy suggested by Poinsot and Lele[33], the characteristic boundary conditions for Navier-Stokes equations can be implemented based on Equation (5.22). In the present study, Equation (5.22) is solved implicitly at the phantom cells in a fully coupled manner with the Navier-Stokes equations governing the inner flow field. For unsteady solutions, the dual time stepping method is used. The semi-discretized equation for Equation (5.22) is:

$$\left[\left(\frac{1}{\Delta\tau} + \frac{1.5}{\Delta t}\right) I - \left(\frac{\partial R_{bc}}{\partial Q}\right)^{n+1,m} + \left(\frac{\partial \mathcal{D}}{\partial Q}\right)^{n+1,m}\right] \delta Q^{n+1,m+1}$$

$$= R_{bc}^{n+1,m} - \mathcal{D}^{n+1,m} - \frac{3Q^{n+1,m} - 4Q^n + Q^{n-1}}{2\Delta t} \tag{5.24}$$

where

$$R_{bc} = -\frac{1}{V}\int_s [(-\frac{1}{Re}\mathbf{E}'_v)\mathbf{i} + (\mathbf{F}' - \frac{1}{Re}\mathbf{F}'_v)\mathbf{j} + (\mathbf{G}' - \frac{1}{Re}\mathbf{G}'_v)\mathbf{k}]\cdot ds \tag{5.25}$$

Compare Equations (5.25) and (4.15), it is noticed that in R_{bc}, there is no $\mathbf{E}'$ flux, which is replaced by vector $\mathcal{D}$. $\mathcal{D}$ is treated as a source term.

Before proceeding to the further analysis, some notations need to be defined. For the finite volume method used in the present study, a row of phantom cells are used outside of the boundary. The boundary conditions are enforced by assigning values to the primitive variables at those phantom cells. All the variables marked by the subscript 'o' are for phantom cells. The variables at the interior cells adjacent to a boundary are denoted by subscript 'i'.

Equation (5.22) provides the set of governing equations for NRBC, but the way to implement the NRBC is not unique. The following is the method used in this study and should not be considered as the only feasible method.

5.2.1 Supersonic outflow boundary conditions

For supersonic flow at exit, all the eigenvalues in Equation (5.10) are positive and the disturbance propagates from inner domain to outside. The wave amplitude vector, Equation (5.17) is evaluated using one side upwind differencing. For supersonic flow at exit, using simple extrapolation may not generate physical wave reflection, but may still generate numerical wave reflection[33]. Solving Equation (5.24) would achieve a more accurate non-reflective boundary conditions for the supersonic flow. For supersonic flow, the exit boundary conditions, ρ_o, ρu_o, ρv_o, ρw_o and ρe_o are completely determined by solving the Navier-Stokes equations in the characteristic form.

To evaluate the derivatives in vector $\mathcal{L}$, either the first order or second order upwind differencing may be used. For the present study, all the partial derivatives in vector $\mathcal{L}$ are calculated by first order upwind differencing.

5.2.2 Subsonic outflow boundary conditions

For subsonic flow at exit, the eigenvalue $U - C$ is negative and the disturbance propagates into the domain from outside. $\mathcal{L}_1$ to $\mathcal{L}_4$ can be still calculated by one-side upwind differencing. However, $\mathcal{L}_5$ corresponding to the eigenvalue of $U - C$ must be treated differently. The commonly-used method to provide a well posed boundary condition is to impose $p = p_\infty$ at the outflow boundary. This treatment however

will create acoustic wave reflections, which may be diffused and eventually disappear when the solution is converged to a steady state solution. For unsteady flows, the wave reflection may contaminate the flow solutions. To avoid wave reflections, the following soft boundary condition was suggested by Rudy-Strikwerda[54] and used by Poinsot-Lele[33].

$$\mathcal{L}_5 = \mathcal{K}(p - p_e) \tag{5.26}$$

where $\mathcal{K}$ is a constant and is determined by $\mathcal{K} = \sigma(1-\mathcal{M}^2)c/L$ as given by Poinsot and Lele in [33] for Cartesian coordinates. The corresponding form used in the generalized coordinates is

$$\mathcal{K} = \sigma|1 - \mathcal{M}^2|/(\sqrt{2}J\rho L) \tag{5.27}$$

where $\mathcal{M}$ is the maximum Mach number in the flow field. L is the characteristic length of the domain. c is the speed of sound. The preferred range for constant σ is 0.2-0.5. The absolute value of $1 - \mathcal{M}^2$ is to ensure the term is positive because the maximum Mach number can be greater than 1 in a transonic flow field.

If $\mathcal{L}_5 = 0$, it switches to the "perfect" non-reflective boundary condition. However, this boundary condition is not well posed and will not lead the solution to the one matching the exit pressure p_∞. Equation (5.26) assumes that the constant exit pressure p_∞ is imposed at infinity. There exists reflection if $p \neq p_\infty$, which is needed for the well posedness of the numerical solution. For the unsteady problems, Equation (5.26) will make the mean value of the pressure at the exit very close to p_∞. However, the pressure at the individual control volume may not be exactly equal to p_∞ even though the value of $\mathcal{L}_5$ can be very small. In this sense, Equation (5.26) may be considered as "almost non-reflective boundary conditions".

The complete boundary conditions used at the exit are the pressure at infinity for Equation (5.26) and three zero gradient viscous conditions:

$$\frac{\partial}{\partial \xi}(\xi_x \tau_{xy} + \xi_y \tau_{yy} + \xi_z \tau_{zy}) = 0 \tag{5.28}$$

$$\frac{\partial}{\partial \xi}(\xi_x \tau_{xz} + \xi_y \tau_{yz} + \xi_z \tau_{zz}) = 0 \tag{5.29}$$

$$\frac{\partial}{\partial \xi}(\xi_x Q_x + \xi_y Q_y + \xi_z Q_z) = 0 \tag{5.30}$$

The amplitudes of the outgoing characteristic waves, $\mathcal{L}_1$, $\mathcal{L}_2$, $\mathcal{L}_3$, and $\mathcal{L}_4$ are computed from the interior domain. All the conservative variables at phantom points are

obtained by solving the characteristic N-S equations, Equation (5.22). All the transverse and viscous terms in Equation (5.22) can be evaluated in the same way as the inner domain control volumes. The Roe's Riemann solver is also used for computing fluxes $\mathbf{F}'$ and $\mathbf{G}'$, central differencing is used for fluxes $\mathbf{E}'_v$, $\mathbf{F}'_v$, $\mathbf{F}'_v$. This strategy makes maximum use of the existing code and minimizes the programming work in implementing the boundary conditions.

5.2.3 Subsonic inflow boundary conditions

At $\xi = 1$ boundary, four characteristic waves, $\mathcal{L}_1$, $\mathcal{L}_2$, $\mathcal{L}_3$, and $\mathcal{L}_4$ are entering the domain while $\mathcal{L}_5$ is leaving the domain. For 3-D open field flow cases, four physical boundary conditions are needed, i.e. u_o, v_o, w_o and ρ_o are set to be constant. Other primitive variables are specified according to the freestream condition. The total energy ρe_o is obtained by solving the energy equation in Equation (5.22). The outgoing wave $\mathcal{L}_5$ can be estimated by using interior variables. The rest of the waves are evaluated by using the LODI relations, Equation (5.23). $\mathcal{L}_1$ - $\mathcal{L}_4$ can be expressed as

$$\mathcal{L}_1 = -\tilde{\xi}_x \frac{\rho}{\sqrt{2}c}(\mathcal{L}_4 + \mathcal{L}_5), \quad \mathcal{L}_2 = -\tilde{\xi}_y \frac{\rho}{\sqrt{2}c}(\mathcal{L}_4 + \mathcal{L}_5), \quad \mathcal{L}_3 = -\tilde{\xi}_z \frac{\rho}{\sqrt{2}c}(\mathcal{L}_4 + \mathcal{L}_5), \quad \mathcal{L}_4 = \mathcal{L}_5 \tag{5.31}$$

5.2.4 Adiabatic wall boundary conditions

At a 3-D adiabatic wall (η = constant), the no-slip condition is enforced by extrapolating the velocity between the phantom and interior cells, $u_o = -u_i$, $v_o = -v_i$, and $w_o = -w_i$. One more physical boundary condition to be imposed on the wall is the adiabatic condition, $\frac{\partial T}{\partial \eta} = 0$. From the adiabatic condition, the ρ_o can be expressed as the following

$$\frac{p_o}{\rho_o} = \frac{p_i}{\rho_i} \tag{5.32}$$

The total energy ρe_o is determined by solving the energy equation in Equation (5.22). Then using Equation (5.32) and Equation (??), ρ_o and p_o can be solved. Cross a η boundary, vector $\mathcal{L}$ is expressed as the following:

$$\mathcal{L} = \begin{pmatrix} \mathcal{L}_1 \\ \mathcal{L}_2 \\ \mathcal{L}_3 \\ \mathcal{L}_4 \\ \mathcal{L}_5 \end{pmatrix} = \begin{pmatrix} V[\tilde{\eta}_x \frac{\partial}{\partial \eta}(\frac{\rho}{J}) + \tilde{\eta}_z \frac{\partial}{\partial \eta}(\frac{v}{J}) - \tilde{\eta}_y \frac{\partial}{\partial \eta}(\frac{w}{J}) - \frac{\tilde{\eta}_x}{c^2} \frac{\partial}{\partial \eta}(\frac{p}{J})] \\ V[\tilde{\eta}_y \frac{\partial}{\partial \eta}(\frac{\rho}{J}) - \tilde{\eta}_z \frac{\partial}{\partial \eta}(\frac{u}{J}) + \tilde{\eta}_x \frac{\partial}{\partial \eta}(\frac{w}{J}) - \frac{\tilde{\eta}_y}{c^2} \frac{\partial}{\partial \eta}(\frac{p}{J})] \\ V[\tilde{\eta}_z \frac{\partial}{\partial \eta}(\frac{\rho}{J}) + \tilde{\eta}_y \frac{\partial}{\partial \eta}(\frac{u}{J}) - \tilde{\eta}_x \frac{\partial}{\partial \eta}(\frac{v}{J}) - \frac{\tilde{\eta}_z}{c^2} \frac{\partial}{\partial \eta}(\frac{p}{J})] \\ (V+C)[\frac{\tilde{\eta}_x}{\sqrt{2}} \frac{\partial}{\partial \eta}(\frac{u}{J}) + \frac{\tilde{\eta}_y}{\sqrt{2}} \frac{\partial}{\partial \eta}(\frac{v}{J}) + \frac{\tilde{\eta}_z}{\sqrt{2}} \frac{\partial}{\partial \eta}(\frac{w}{J}) + \beta \frac{\partial}{\partial \eta}(\frac{p}{J})] \\ (V-C)[-\frac{\tilde{\eta}_x}{\sqrt{2}} \frac{\partial}{\partial \eta}(\frac{u}{J}) - \frac{\tilde{\eta}_y}{\sqrt{2}} \frac{\partial}{\partial \eta}(\frac{v}{J}) - \frac{\tilde{\eta}_z}{\sqrt{2}} \frac{\partial}{\partial \eta}(\frac{w}{J}) + \beta \frac{\partial}{\partial \eta}(\frac{p}{J})] \end{pmatrix} \tag{5.33}$$

where $V = \eta_x u + \eta_y v + \eta_z w$ and $C = c|\nabla\eta|$, $|\nabla\eta| = \sqrt{{\eta_x}^2 + {\eta_y}^2 + {\eta_z}^2}$. It can be seen from Equation (5.33), the characteristic waves $\mathcal{L}_1$ - $\mathcal{L}_3$ vanish since $V = 0$ at wall surface. At lower wall ($\eta = 1$), the outgoing characteristic wave $\mathcal{L}_5$ is computed from the interior domain. The incoming wave $\mathcal{L}_4$ is estimated by using LODI relations. By solving 2nd - 4th equations in Equation (5.23), it yields $\mathcal{L}_4 = \mathcal{L}_5$. At upper wall (maximum η), the $\mathcal{L}_4$ becomes the outgoing wave, and it can be computed from the interior domain. $\mathcal{L}_5$ is the incoming wave which is evaluated by $\mathcal{L}_5 = \mathcal{L}_4$.

Chapter 6

Structural Models

6.1 Modal Approach for 3D Wing[4]

The governing equation of the solid structure motion can be written as,

$$\mathbf{M}\frac{d^2\mathbf{u}}{dt^2} + \mathbf{C}\frac{d\mathbf{u}}{dt} + \mathbf{K}\mathbf{u} = \mathbf{f} \tag{6.1}$$

where $\mathbf{M}$, $\mathbf{C}$ and $\mathbf{K}$ are the mass, damping, and stiffness matrices of the solid respectively, $\mathbf{u}$ is the displacement vector and $\mathbf{f}$ is the force exerted on the surface node points of the solid, both can be expressed as:

$$\mathbf{u} = \begin{pmatrix} \mathbf{u}_1 \\ \vdots \\ \mathbf{u}_i \\ \vdots \\ \mathbf{u}_N \end{pmatrix}, \mathbf{f} = \begin{pmatrix} \mathbf{f}_1 \\ \vdots \\ \mathbf{f}_i \\ \vdots \\ \mathbf{f}_N \end{pmatrix},$$

where N is the total number of node points of the structural model, $\mathbf{u}_i$ and $\mathbf{f}_i$ are vectors with 3 components in x, y, z directions:

$$\mathbf{u}_i = \begin{pmatrix} \mathbf{u}_{ix} \\ \mathbf{u}_{iy} \\ \mathbf{u}_{iz} \end{pmatrix}, \mathbf{f}_i = \begin{pmatrix} \mathbf{f}_{ix} \\ \mathbf{f}_{iy} \\ \mathbf{f}_{iz} \end{pmatrix}.$$

$\mathbf{f}_i$ is dynamic force exerted on the surface of the solid body. In a modal approach, the modal decomposition of the structure motion can be expressed as follows:

$$\mathbf{K\Phi} = \mathbf{M\Phi\Lambda} \tag{6.2}$$

or

$$\mathbf{K}\phi_j = \lambda_j \mathbf{M}\phi_j \tag{6.3}$$

where $\mathbf{\Lambda}$ is eigenvalue matrix, $\mathbf{\Lambda} = diag[\lambda_1, \cdots, \lambda_j, \cdots, \lambda_{3N}]$, and jth eigenvalue $\lambda_j = {\omega_j}^2$, ω_j is the natural frequency of jth mode, and the mode shape matrix $\mathbf{\Phi} = [\phi_1, \cdots, \phi_j, \cdots, \phi_{3N}]$.

Equation (6.15) can be solved by using a finite element solver (e.g. ANSYS) to obtain its finite number of mode shapes ϕ_j. The first five mode shapes will be used in this paper to calculate the displacement of the structure such that,

$$\mathbf{u}(t) = \sum_j a_j(t)\phi_j = \mathbf{\Phi a} \tag{6.4}$$

where $\mathbf{a} = [a_1, a_2, a_3, a_4, a_5]^T$. Substitute Equation (6.4) to Equation (6.1) and yield

$$\mathbf{M\Phi}\frac{d^2\mathbf{a}}{dt^2} + \mathbf{C\Phi}\frac{d\mathbf{a}}{dt} + \mathbf{K\Phi a} = \mathbf{f} \tag{6.5}$$

Multiply Equation (6.5) by $\mathbf{\Phi}^T$ and re-write it as

$$\hat{\mathbf{M}}\frac{d^2\mathbf{a}}{dt^2} + \hat{\mathbf{C}}\frac{d\mathbf{a}}{dt} + \hat{\mathbf{K}}\mathbf{a} = \mathbf{P} \tag{6.6}$$

where $\mathbf{P} = [P_1, P_2, \cdots, P_j, \cdots, P_N]^T$, the modal force of jth mode, $P_j = \phi_j^T\mathbf{f}$, the modal mass matrix is defined as

$$\hat{\mathbf{M}} = \mathbf{\Phi}^T\mathbf{M\Phi} = diag(m_1, \cdots, m_j, \cdots, m_{3N}) \tag{6.7}$$

where m_j is the modal mass of jth mode, and the modal damping matrix is defined as

$$\hat{\mathbf{C}} = \mathbf{\Phi}^T\mathbf{C\Phi} = diag(c_1, \cdots, c_j, \cdots, c_{3N}) \tag{6.8}$$

where c_j is the modal damping of jth mode, and the modal stiffness matrix is defined as

$$\hat{\mathbf{K}} = \mathbf{\Phi}^T\mathbf{K\Phi} = diag(k_1, \cdots, k_j, \cdots, k_{3N}) \tag{6.9}$$

where k_j is the modal stiffness of jth mode. Equation (6.6) implies

$$\frac{d^2a_j}{dt^2} + 2\zeta_j\omega_j\frac{da_j}{dt} + \omega_j^2 a_j = \frac{\phi_j^T \mathbf{f}}{m_j} \tag{6.10}$$

where ζ_j is modal damping ratio. Equation (6.18) is the modal equation of structure motion, and is solved numerically within each iteration. By carefully choosing reference quantities, the normalized equation may be expressed as

$$\frac{d^2a_j}{dt^{*2}} + 2\zeta_j\left(\frac{\omega_j}{\omega_\alpha}\right)\frac{da_j}{dt^*} + \left(\frac{\omega_j}{\omega_\alpha}\right)^2 a_j = \phi_j^{*T}\mathbf{f}^* V^* \left(\frac{b_s}{L}\right)^2 \frac{\bar{m}}{v^*} \tag{6.11}$$

where the dimensionless quantities are denoted by an asterisk, ω_α is the natural frequency in pitch, b_s is the streamwise semichord measured at wing root, L is the reference length, $\bar{m}$ is the measured wing panel mass, v^* is the volume of a conical frustum having streamwise root chord as lower base diameter, streamwise tip chord as upper base diameter, and panel span as height, $V^* = \frac{U_\infty}{b_s\omega_\alpha\sqrt{\bar{\mu}}}$, and U_∞ is the freestream velocity.

Then the equations are transformed to a state form and expressed as:

$$[\mathbf{M}]\frac{\partial\{\mathbf{S}\}}{\partial t} + [\mathbf{K}]\{\mathbf{S}\} = \mathbf{q} \tag{6.12}$$

where

$$\mathbf{S} = \begin{pmatrix} a_j \\ \dot{a}_j \end{pmatrix},\ \mathbf{M} = [I],\ \mathbf{K} = \begin{pmatrix} 0 & -1 \\ \left(\frac{\omega_j}{\omega_\alpha}\right)^2 & 2\zeta\left(\frac{\omega_j}{\omega_\alpha}\right) \end{pmatrix},\ \mathbf{q} = \begin{pmatrix} 0 \\ \phi_j^{*T}\mathbf{f}^* V^* \left(\frac{b_s}{L}\right)^2 \frac{\bar{m}}{v^*} \end{pmatrix}.$$

To couple the structural equations with the equations of flow motion and solve them implicitly in each physical time step, above equations are discretized and integrated in a manner consistent with Equation (4.14) to yield

$$\left(\frac{1}{\Delta\tau}\mathbf{I} + \frac{1.5}{\Delta t}\mathbf{M} + \mathbf{K}\right)\delta S^{n+1,m+1} = -\mathbf{M}\frac{3\mathbf{S}^{n+1,m} - 4\mathbf{S}^n + \mathbf{S}^{n-1}}{2\Delta t} - \mathbf{K}\mathbf{S}^{n+1,m} + \mathbf{q}^{n+1,m+1} \tag{6.13}$$

where n is the physical time level index while m stands for the pseudo time index. The detailed coupling procedure between the fluid and structural systems is given in the following chapter.

6.2 Mistuned Bladed Structural Model for Transient Response

The Subsets of Nominal Modes (SNM) structural model suggested by Yang and Griffin [43] is developed in this research for time domain to calculate the structural modes, which are expensive to calculate if the direct finite element approach is used. Yang and Griffin recognized that each mistuned structural mode can be well represented by a subset of the tuned structural modes. The SNM approach was developed to take the finite element modal solution of the tuned structure as the input to formulate a reduced order model for the mistuned structure. The order of the problem thus dropped from millions to hundreds, and the computational time to compute a mistuned structural mode is reduced from hours to seconds. This is critical to the simulation of fully coupled fluid-structural problems because only very limited computational resource is required in addition to the CPU intensive CFD computation. A brief description of the SNM model is in the following:

a) Transformation from Finite Element Domain to Modal Domain

First, the equation of motion in the finite element form is transformed into the modal coordinates. Assuming that the variation of the mechanical damping is negligible, then

$$(\hat{M}^0 + \Delta\hat{M})\ddot{\alpha} + \hat{C}^0\dot{\alpha} + (\hat{K}^0 + \Delta\hat{K})\alpha = \mathbf{p} \tag{6.14}$$

In eq. (6.14), the modal coordinate vector α is the displacements of the tuned modes, $\hat{M}^0$, $\hat{C}^0$, and $\hat{K}^0$ are the modal mass, damping, and stiffness matrices of the tuned system, and typically diagonal, $\Delta\hat{K}$ and $\Delta\hat{M}$ are the changes in modal stiffness and mass matrices, and $\mathbf{p}$ is the modal force vector. Eq. (6.14) can then be cast in a state space form,

$$B\dot{\mathbf{y}} = A\mathbf{y} + \mathbf{q} \tag{6.15}$$

where

$$B = \begin{pmatrix} I & 0 \\ 0 & (\hat{M}^0 + \Delta\hat{M}) \end{pmatrix}, \qquad \mathbf{y} = \begin{pmatrix} \alpha \\ \dot{\alpha} \end{pmatrix} \tag{6.16}$$

$$A = \begin{pmatrix} 0 & I \\ -(\hat{K}^0 + \Delta\hat{K}) & -\hat{C}^0 \end{pmatrix}, \qquad \mathbf{q} = \begin{pmatrix} 0 \\ \mathbf{p} \end{pmatrix} \tag{6.17}$$

Eq. (6.15) is the modal equation of motion for the mistuned structure. Without truncating the modes, the order of eq. (6.15) is 2N where N is the number of degrees of freedom of the whole wheel finite element model. However, the order can be reduced

to 2n, where n is tuned modes selected in the SNM representation, to simulate the mistuned structural vibration with sufficient accuracy. N (millions) is typically much greater than n (hundreds).

b) Diagonalization of the Modal Governing Equation

To improve the computational efficiency, the solution of eq. (6.15) can be further expressed in terms of its right eigenvectors $\mathbf{R}$ which satisfies the following eigenvalue problem

$$A\mathbf{R} = B\mathbf{R}\Lambda \tag{6.18}$$

where Λ is the diagonal eigenvalue matrix of the mistuned structure. Applying the classical modal analysis technique, eq. (6.15) can be transformed in a diagonal form

$$\hat{B}\dot{\beta} = \hat{A}\beta + \hat{\mathbf{q}} \tag{6.19}$$

where the diagonal matrices $\hat{B}$ and $\hat{A}$ are the generalized mass and stiffness matrices, β is the generalized coordinates, and $\mathbf{q}$ is the generalized forces. Since the components of β are decoupled from each other, eq. (6.19) can be simulated at very low computational costs.

Note that, in eq. (6.19), $\hat{B}$ and $\hat{A}$ mathematically define a mistuned bladed disk structure, the generalized force $\hat{\mathbf{q}}$ is derived from the pressure distribution on the airfoil surfaces, and the time-varying unknown β will be solved at each time step.

Chapter 7

Fully Coupled Fluid-Structural Interaction

To rigorously simulate fluid-structural interactions, the equations of flow motion and structural response need to be solved simultaneously within each iteration in a fully coupled numerical model. The calculation based on fully coupled iteration is CPU expensive, especially for three dimensional applications. The modal approach can save CPU time significantly by solving the modal displacement equations, Eq. (6.18), instead of the original structural equations, Eq. (6.15), which is usually solved by using finite element method. In the modal approach, the structural mode shapes can be pre-determined by using a separate finite element structural solver. Once the several mode shapes of interest are obtained, the physical displacements can be calculated just by solving those simplified linear equations, i.e., Eqs. (6.18) and (6.4). In present study, the first five mode shapes provided in Ref.[55] are used to model the wing structure. These pre-calculated mode shapes are obtained on a fixed structural grid system and are transformed to the CFD grid system by using a 3rd order polynomial fitting procedure. The procedure is only performed once and then the mode shapes for CFD grid system are stored in the code throughout the simulation.

The procedure of the fully coupled fluid-structure interaction by modal approach is described below:

(1) The flow solver provides dynamic forces on solid surfaces.

(2) Integrate fluid forces at each surface element to obtain the forcing vector $\mathbf{f}$.

(3) Use Eq. (6.18) to calculate modal displacements $a_j (j = 1, 2, 3, 4, 5)$ of the next pseudo time step.

(4) Use Eq. (6.4) to calculate physical displacement $\mathbf{u}$ of the next pseudo time step.

(5) Check the maximum residuals of both solutions of the flow and the structural equations. If the maximum residuals are greater than the prescribed convergence criteria, go back to step (1) and proceed to the next pseudo time. Otherwise the calculation of the flow field and the structural displacement within the physical time step is completed and the next new physical time step starts. The procedure is also illustrated in the flow chart given in Fig. 12.132.

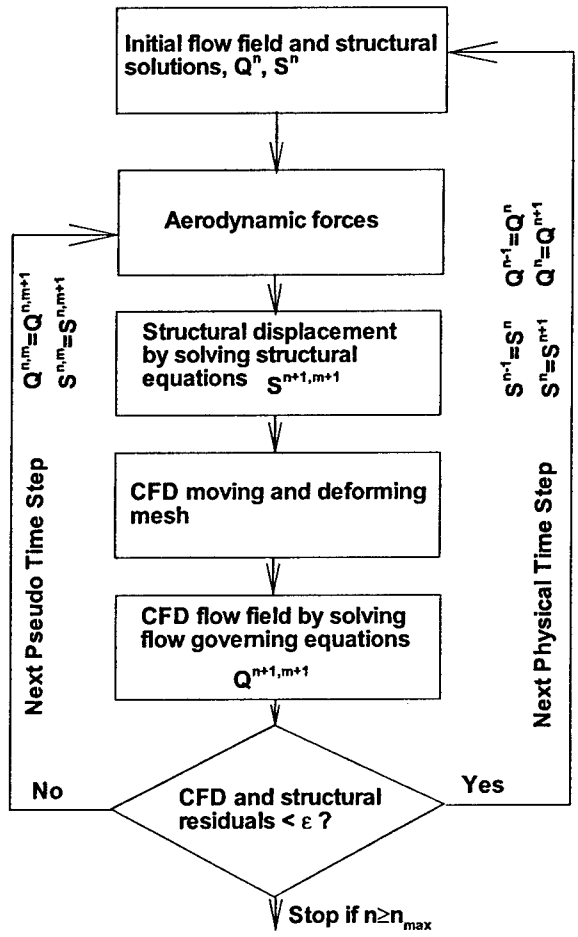

Figure 7.1: Fully coupled flow-structure interaction procedure

Chapter 8

Results and Discussion

8.1 Validation of Zha-Hu E-CUSP Schemes[1]

The original Zhu-Hu E-CUSP scheme described from Eq. 4.25 to 4.35 was developed and then used as the basis for the Zha E-CUSP2 scheme.

8.1.1 Shock Tubes

For shock tube problems, the interests are focused on: 1) the quality (monotonicity and sharpness) of the shock and contact discontinuities; 2)the maximum allowable CFL number to be used for explicit Euler method.

For explicit Euler time marching scheme, it is desirable that the CFL number is close to the upper limit of 1.0. For the 1D linear wave equation with CFL=1 and 1st order upwind scheme, the numerical dissipation and dispersion vanish. For nonlinear Euler equations, it is also true that the closer the CFL to 1.0, the less the numerical dissipation.

The Sod Problem

Fig. 12.1 to 12.5 are the computed temperature distributions using different upwind schemes with first order accuracy compared with the analytical result of the Sod problem[56]. Since the computation stops before the waves reach either end of the shock tube, the first order extrapolation boundary conditions are used at both ends of the shock tube for all the schemes.

The maximum allowable CFL number for a scheme is defined as: beyond which the solution will either be oscillatory or unstable. The new E-CUSP scheme (Zha CUSP in the figures) achieves maximum CFL of 1.00, and the shock profile is the

crispest and remains monotone (Fig.12.1). The maximum allowable CFL of Roe and Van Leer scheme are 0.95 and 0.96 respectively. The new E-CUSP scheme takes three grid points across the shock wave, while the Roe and Van Leer schemes take four grid points (see Fig.12.1, 12.2 and 12.3). The Van Leer scheme generates a tail at the end of the expansion wave (see Fig. 12.3). Interestingly, the Van Leer-Hänel scheme can reach maximum CFL =1.0 and the shock profile is also crisper than the original Van Leer scheme with no tail generated at the end of the expansion wave (see Fig. 12.4). All the schemes smear the contact surface to a similar extent. The expansion wave is captured well by all the schemes. The AUSM$^+$ scheme has the unexpectedly low maximum allowable CFL of 0.275. The whole shock and contact surface profiles are seriously smeared due to the low maximum CFL number.

The table 8.1 given below summarizes the maximum allowable CFL number for each scheme. Overall, for the Sod 1D shock tube problem, the new scheme suggested in this paper performs the best based on the shock sharpness, monotonicity, and stability.

Table 8.1: Maximum CFL Numbers for Sod 1D Shock Tube

Scheme	CFL Number
The new scheme (Zha CUSP)	1.00
Van Leer-Hänel	1.00
Van Leer	0.96
Roe	0.95
Liou $AUSM^+$	0.275

Slowly Moving Contact Surface

This is a shock tube case used in [57] to demonstrate the capability of the scheme to capture the contact surface. The initial conditions are $[\rho, u, p]_L = [0.125, 0.112, 1.0]$, $[\rho, u, p]_R = [10.0, 0.112, 1.0]$. All the results are first order accuracy. Fig. 12.6 shows that the new E-CUSP scheme , the Roe scheme and the AUSM$^+$ scheme all can resolve the contact surface accurately as they are designed. The results of those schemes are at time level 0.01. The velocity is uniformly constant and the density discontinuity is monotone. The new E-CUSP (Zha CUSP) scheme has far higher CFL number than the other schemes with the value of 1.00. The Roe scheme has the max CFL=0.3, and Liou's MUMS$^+$ has 0.48. Fig.12.7 shows that the Roe scheme generates large velocity oscillations when CFL=0.35, greater than its max CFL=0.3.

The schemes of Van Leer, Van Leer-Hänel severely distort the profiles of the contact surfaces as shown in Fig. 12.8. The velocity profiles are largely oscillatory. The density jumps are also more smeared.

The table 8.2 lists the maximum CFL number of each scheme for the slowing moving contact surface. Again, the new scheme outperforms the other schemes by having the highest CFL number and still maintain the monotonicity.

Table 8.2: Maximum CFL numbers of the schemes resolving the contact surface

Scheme	CFL Number
The new E-CUSP (Zha CUSP) scheme	1.00
Liou $AUSM^+$	0.48
Roe	0.32
Van Leer	fail
Van Leer-Hänel	fail

8.1.2 Entropy condition

This case is to test if a scheme violates the entropy condition by allowing the expansion shocks. The test case is a simple quasi-1D converging-diverging transonic nozzle[58, 59]. The correct solution should be a smooth flow from subsonic to supersonic with no shock. However, for an upwind scheme which does not satisfy the entropy condition, an expansion shock may be produced.

For the subsonic boundary conditions at the entrance, the velocity is extrapolated from the inner domain and the other variables are determined by the total temperature and total pressure. For supersonic exit boundary conditions, all the variables are extrapolated from inside of the nozzle. The analytical solution was used as the initial flow field. Explicit Euler time marching scheme was used to seek the steady state solutions. All the schemes use first order differencing.

Fig. 12.9 is the comparison of the analytical and computed Mach number distributions with 201 mesh points using the new scheme and the scheme of Roe, Van Leer, Van Leer-Hänel, Liou's AUSM$^+$. The analytical solution is smooth throughout the nozzle and reaches the sonic speed at the throat (the minimum area of the nozzle, located at $X/h = 4.22$). It is seen that both the Roe scheme and Van Leer scheme generate a strong expansion shock at the nozzle throat. Both schemes can converge to machine zero (12 order of magnitude) with CFL=0.95 even with the expansion shock waves.

The Van Leer-Hänel scheme can not converge even with CFL=0.01. The result plotted in Fig. 12.9 is the one before it diverges. It shows an expansion shock with the Mach number jumping from 0.74 to 1.42. The AUSM$^+$ also has difficulties to converge for this case. Using CFL=0.05, it managed to reduce the residual by 4 order of magnitude. The solution of the AUSM$^+$ also shows an expansion shock with the

Mach number jumping from 0.86 to 1.17.

The new E-CUSP scheme does not have an expansion shock wave at the sonic point, but is not smooth due to the discontinuity of the first derivative of the pressure at the sonic point. This is shown as a small glitch at the sonic point in fig. 12.9. The glitch does not affect the scheme to converge the solution to machine zero with CFL=0.95.

As indicated in [58, 59], the amplitude of the expansion shock decreases when the mesh is refined. When the 2nd order schemes with the MUSCL differencing are used, all the expansion shock waves as well as the glitch of the new scheme at the sonic point disappear. Since this paper is to compare the original Riemann solver schemes, no entropy fix[60] that can remove the expansion shock of Roe schemes was used.

8.1.3 Wall Boundary Layer

To examine the numerical dissipation of the new scheme, a laminar supersonic boundary layer on an adiabatic flat plate is calculated using first order accuracy. The incoming Mach number is 2.0. The Reynolds number based on the length of the flat plate is 40000. The Prandtl number of 1.0 is used in order to compare the numerical solutions with the analytical solution. The baseline mesh size is 81×61 in the direction along the plate and normal to the plate respectively.

Fig.12.10 is the comparison between the computed velocity profiles and the Blasius solution. The solutions of the new scheme (Zha CUSP), Roe scheme, and AUSM$^+$ scheme agree very well with the analytical solution. The Van Leer scheme significantly thickens the boundary layer. The Van Leer- Hänel scheme does not improve the velocity profile.

Fig.12.11 is the comparison between the computed temperature profiles and the Blasius solution. Again, the new scheme (Zha CUSP), Roe scheme, and AUSM$^+$ scheme accurately predict the temperature profiles and the computed solutions basically go through the analytical solution. Both the Van Leer scheme and the Van Leer- Hänel scheme significantly thicken the thermal boundary layer similarly to the velocity profiles.

Table 8.3 shows the wall temperature predicted by all the schemes using the baseline mesh and refined mesh. The predicted temperature value by the Van Leer scheme has a large error. The Van Leer- Hänel scheme does predict the wall temperature accurately even though the overall profile is nearly as poor as that predicted by the Van Leer scheme. The new scheme, Roe scheme and AUSM+ scheme all predict the temperature accurately.

All the results mentioned above are converged based on mesh size. The wall temperatures using the refined mesh of 161×121 are also given in table 8.3. There is little difference between the results of the baseline mesh and the refined mesh. The refined mesh does not help to reduce the large numerical dissipation of the Van Leer

scheme. When the 2nd order schemes are used, both the velocity and temperature profiles of the Van Leer scheme and Van Leer- Hänel are improved (not shown).

Scheme	T_{wall}, Mesh 80 × 60	T_{wall}, Mesh 160 × 120
Blasius analytical solution	1.8000	1.8000
The new E-CUSP (Zha CUSP) scheme	1.8025	1.8018
Roe scheme	1.8002	1.7996
Liou $AUSM^+$	1.8000	1.8000
Van Leer	1.8328	1.8333
Van Leer-Hänel	1.7970	1.7996

Table 8.3: Computed non-dimensional wall temperature using first order schemes with the baseline mesh and refined mesh

8.1.4 Transonic Converging-Diverging Nozzle

To examine the performance of the new scheme in two-dimensional flow and the capability to capture the shock waves which do not align with the mesh lines, a transonic converging-diverging nozzle is calculated as inviscid flow. The nozzle was designed and tested at NASA and was named as Nozzle A1[61]. Third order accuracy of MUSCL type differencing is used to evaluate the inviscid flux with the Minmod limiter. Fig.12.12 is the computed Mach number contour using the new E-CUSP scheme with the mesh size of 175 × 80. In the axial direction, there are 140 mesh points distributed downstream of the nozzle throat, where the oblique shock waves are located. The grid is clustered near the wall. For clarity, the coarsened mesh is drawn as the background with the Mach contours to show the relative orientation of the shock waves and the mesh lines. The nozzle is symmetric about the centerline. Hence only upper half of the nozzle is calculated. The upper boundary uses the slip wall boundary conditions and the lower boundary of the center line uses the symmetric boundary conditions.

As indicated by the wall surface isentropic Mach number distribution shown in fig.12.13, the flow is subsonic at the inlet with the Mach number about 0.22 and is accelerated to sonic at the throat, and then reaches supersonic with Mach number about 1.35 at the exit. Fig.12.12 shows that right after throat, an expansion fan emanates from the wall and accelerates the flow to reach the peak Mach number about 1.5. Due to the sharp throat turning, an oblique shock appears immediately downstream of the expansion fan to turn the flow to axial direction. The two oblique shocks intersect at the centerline, go through each other, hit the wall on the other side, and then reflect from the wall. Such shock patten is repeated to the exit and the shock strength is weakened with the flow going downstream. Fig. 12.13 shows that the isentropic Mach number distributions predicted by the new CUSP scheme

and the Roe scheme agree fairly well with the experiment. The new E-CUSP scheme and the Roe scheme have virtually indistinguishable results.

The mesh refinement study indicates that the mesh resolution in the axial direction does not affect the shock resolution much. The axial mesh size of 280 downstream of the throat yields only slightly better shock resolution than the size of 70. However, the mesh size in the vertical direction dramatically changes the shock resolution. The mesh size of 80 in the vertical direction yields much better resolution than the mesh size of 50. This can be seen from the isentropic Mach number in fig.12.13, which shows that the mesh size of 175×80 generates much sharper profiles than those of the mesh 175×50 for the first and second shock reflections.

For this transonic nozzle with the mesh size 175×80 on an Intel Xeon 1.7Ghz processor, the CPU time per time step per node to calculate the inviscid flux is $2.5871 \times 10^{-6} s$ for the new scheme, which is about 25% of the CPU time of $1.0284 \times 10^{-5} s$ used for the Roe scheme. This is a significant CPU time reduction.

8.1.5 Transonic Inlet-Diffuser

To examine the performance of the new scheme for shock wave/turbulent boundary layer interaction, a transonic inlet-diffuser[62] is calculated as shown by the Mach number contours in fig.12.14, which has the exit back pressure equal to 0.83 times of the inlet total pressure. The Reynolds number based on the throat height is 4.38×10^5. The Baldwin-Lomax[48] algebraic turbulence model is used. Third order accuracy of MUSCL-type differencing with the Minmod limiter is used for the inviscid fluxes and the second order central differencing is used for the viscous terms.

A normal shock is located downstream of the throat as shown in fig.12.14. No flow separation is generated under this back pressure. The baseline mesh size is 100×60. When y_1^+ is held as constant and the mesh is refined in both the horizontal and vertical direction, the results have little variation and are converged based on mesh size. All the inlet-diffuser results presented in this paper are from the mesh size of 100×120. The mesh in the horizontal direction is clustered around the shock location to better resolve the shock profile.

Fig. 12.15 is the comparison of the upper wall surface pressure between the experiment and the computation. The agreement is very good except that the computation predicts the shock location a little downstream of the experimental shock location and the shock strength a little too strong. It is found that the shock profile is sensitive to the y_1^+. The y_1^+ value of $2, 2 \times 10^{-4}, 7 \times 10^{-6}$ are tested. The smaller y_1^+ yields a little closer shock location to the experiment. The results shown in fig.12.14 and 12.15 have the y_1^+ value of 2×10^{-4}. The small y_1^+ effect is believed due to the first order extrapolation of the pressure on wall surface instead of the requirement of the turbulence modeling. In the region with no shock, the first order pressure extrapola-

tion on the wall is insensitive to the distance of the first cell to the wall, while in the shock region it is sensitive due to the large streamwise gradient. As indicated in fig. 12.15, the Roe scheme predicts the shock location slightly closer to the experiment than the new CUSP scheme.

When the back pressure is reduced to 0.72 times of the inlet total pressure. The normal shock is stronger and the flow separation is induced. The same mesh as the previous case is used for this case. Fig.12.17 is the predicted pressure distribution compared with the experiment. Both the new CUSP scheme and the Roe scheme predict the shock location accurately, but the shock strength predicted is too strong. However, the new scheme has the pressure profile in the separation region downstream of the shock noticeably closer to the experiment than that predicted by the Roe scheme.

It should be pointed out that the turbulence modeling is a critical factor for the prediction accuracy of the shock wave/turbulent boundary layer interaction. Hence the discrepancy between the calculation and experiment shown above is only partially attributed to the different discretization schemes.

Fig.12.17 is the pressure contours computed using $p_{out}/p_t = 0.72$ with the new scheme, Roe Scheme, and Liou's AUSM$^+$ scheme. A curved λ shock is formed due to the shock wave/turbulent boundary layer interaction. The shape of the Mach contours of the new scheme (Zha CUSP) and the Roe scheme are very much alike. The contours computed by the AUSM$^+$ scheme has significant oscillations near the wall.

8.2 Validation of the Zha E-CUSP2 Scheme[3]

The Zha E-CUSP2 scheme defined from Eq. 4.25 to 4.39 was validated for the shock tube and laminar boundary layer. The results are as good as the original Zha-Hu scheme or better. More importantly, the Zha E-CUSP2 scheme has cured the temperature oscillation of the original Zha-Hu scheme as shown below.

8.2.1 Transonic Converging-Diverging Nozzle

To examine the performance of the new scheme in two-dimensional flow and the capability to capture the shock waves which do not align with the mesh lines, a transonic converging-diverging nozzle is calculated as inviscid flow. The nozzle was designed and tested at NASA and was named as Nozzle A1[61]. Third order accuracy of MUSCL type differencing is used to evaluate the inviscid flux with no limiter.

Fig.12.18 is the computed Mach number contours using the original Zha CUSP scheme and the Zha CUSP2 scheme with the mesh size of 175×80. The nozzle is

symmetric about the centerline. Hence only upper half of the nozzle is calculated. The upper boundary uses the slip wall boundary conditions and the lower boundary of the center line uses the symmetric boundary conditions. The Mach contour lines computed by the two schemes look very much the same. However, if the temperature contours near the wall is zoomed in, it can be seen that the temperature contours computed by the Zha CUSP scheme has large oscillations as shown in Fig. 12.19, (a). The temperature oscillation exist along the whole upper wall and lower symmetric boundary. The temperature oscillations are removed by the Zha CUSP2 scheme as shown in Fig. 12.19, (b). All the other flow variables are smooth for the new scheme.

The reason that the original Zha CUSP scheme has no temperature oscillation shown in Fig. 2 for the flat plate , but has oscillation for the inviscid nozzle may be the following: 1) The laminar Navier-Stokes equations provide some physical dissipation to smoothen the flow; 2) The boundary layer gradient may generate some numerical dissipation to smoothen the flow; 3) The 1st order scheme (piecewise constant) is used for the flat plate. The 1st order scheme is monotone and has higher numerical dissipation than the 3rd order scheme used for the nozzle.

8.3 2D Flow Induced Vibration

8.3.1 Stationary Cylinder

The flow past a stationary cylinder is used as an unsteady flow validation case. The baseline mesh dimensions are 120×80 in circumferential and radial directions. The far field boundary is located 20 diameters away from the center of the cylinder. The Reynolds number based on the free-stream condition and cylinder diameter is, $Re = 500$. The laminar Navier-Stokes equations will be solved due to the low Reynolds number.

The computed drag and lift coefficients are shown in Figure 12.23. As shown in the figure, the lift oscillates at certain frequency in terms of the Strouhal number. The drag coefficient oscillates with twice that frequency. The mesh refinement study and computed Strouhal number, drag, lift and moment coefficients are listed in Table 8.4

Table 8.4 shows that the solution is converged based on mesh size. The computed lift frequency by Zha-Hu CUSP scheme agrees well with the experimental results of Roshko[66] and Goldstein[64], and is closer to the experimental results than the one computed by by Alonso et al.[65], which uses more grid points.

Table 8.4: Results of Mesh Refinement Study and comparison with the experiments

Mesh Dimension	St_{C_d}	St_{C_l}	St_{C_m}	C_l	C_d
120×80	0.4395	0.2197	0.2197	±1.1810	1.4529±0.1305
200×120	0.4516	0.2246	0.2246	±1.2267	1.4840±0.1450
(Roshko 1954[63])		0.2075			
(Goldstein 1938[64])		0.2066			
384×96 (Alonso 1995[65])	0.46735	0.23313		1.14946(C_{lmax})	1.31523(C_{davg})

8.3.2 Vortex-Induced Oscillating Cylinder

Structure Model of Elastic Cylinder

For the computations of the vortex-induced oscillating cylinder, which is elastically supported as shown in Figure ?? so that it oscillates only in the direction aligned with or normal to the incoming flow, the structural dynamic equations which govern the motion of the cylinder are:

$$m\ddot{x} + C_x\dot{x} + K_x x = D \tag{8.1}$$

$$m\ddot{y} + C_y\dot{y} + K_y y = L \tag{8.2}$$

These equations are solved implicitly together with the equations of flow motion, Equation (4.14), in a fully coupled manner. In Equation (8.1), $\ddot{x}$, $\dot{x}$, and x represent the dimensionless horizontal acceleration, velocity and displacement of the moving object respectively. Similarly, $\ddot{y}$, $\dot{y}$, and y in Equation (8.2) represent their corresponding ones in vertical direction. m, L, and D are the mass, lift, and drag per unit span respectively, C_x and C_y are the damping coefficients in horizontal and vertical directions, K_x and K_y are the spring constants in horizontal and vertical directions. In present study, this 'self-excited oscillators' is designed to have the same response in both direction, i.e. $C_x = C_y$ and $K_x = K_y$.

If the normalization procedure is applied to Equations (8.1) and (8.2) by using the same reference scales of those used for the equations of flow motion, the following nondimensional equations are obtained

$$\ddot{x} + 2\zeta\left(\frac{2}{\bar{u}}\right)\dot{x} + \left(\frac{2}{\bar{u}}\right)^2 x = \frac{2}{\mu_s\pi}C_d \tag{8.3}$$

$$\ddot{y} + 2\zeta\left(\frac{2}{\bar{u}}\right)\dot{y} + \left(\frac{2}{\bar{u}}\right)^2 y = \frac{2}{\mu_s\pi}C_l \tag{8.4}$$

where ζ is the nondimensional structural damping coefficient calculated by $\zeta = \frac{C_{x,y}}{2\sqrt{mK_{x,y}}}$, $\bar{u}$ is the reduced velocity defined by $\bar{u} = \frac{U_\infty}{b\omega}$, b is radius of the cylinder,

$\omega = \sqrt{K_{x,y}/m}$, the mass ratio, $\mu_s = \frac{m}{\pi\rho_\infty b^2}$, C_d and C_l are the drag and lift force coefficients respectively. Then the equations are transformed to a matrix form and expressed by

$$[\mathbf{M}]\frac{\partial\{\mathbf{S}\}}{\partial t} + [\mathbf{K}]\{\mathbf{S}\} = \mathbf{q} \tag{8.5}$$

where

$$\mathbf{S} = \begin{pmatrix} x \\ \dot{x} \\ y \\ \dot{y} \end{pmatrix}, \mathbf{M} = [I], \mathbf{K} = \begin{pmatrix} 0 & -1 & 0 & 0 \\ \left(\frac{2}{\bar{u}}\right)^2 & 2\zeta\left(\frac{2}{\bar{u}}\right) & 0 & 0 \\ 0 & 0 & 0 & -1 \\ 0 & 0 & \left(\frac{2}{\bar{u}}\right)^2 & 2\zeta\left(\frac{2}{\bar{u}}\right) \end{pmatrix}, \mathbf{q} = \begin{pmatrix} 0 \\ \frac{2}{\mu_s\pi}C_d \\ 0 \\ \frac{2}{\mu_s\pi}C_l \end{pmatrix}.$$

To couple the structural equations with the equations of flow motion and solve them implicitly in each physical time step, above equations are discretized and integrated in a manner consistent with Equation (4.14) to yield

$$\left(\frac{1}{\Delta\tau}\mathbf{I} + \frac{1.5}{\Delta t}\mathbf{M} + \mathbf{K}\right)\delta S^{n+1,m+1} = -\mathbf{M}\frac{3\mathbf{S}^{n+1,m} - 4\mathbf{S}^n + \mathbf{S}^{n-1}}{2\Delta t} - \mathbf{K}\mathbf{S}^{n+1,m} + \mathbf{q}^{n+1,m+1} \tag{8.6}$$

where n is the physical time level index while m stands for the pseudo time index. The detailed coupling procedure between the fluid and structural systems is given in section 4.

After validating the stationary cylinder vortex shedding flow, the cylinder is released to be controlled by the structure model as shown in Figure ??. The corresponding structural equations are given in section 3.1. The laminar Navier-Stokes equations are solved due to the low Reynolds number, $Re = 500$.

Using the temporally periodic solution obtained in the computation of stationary cylinder as the initial flow field, the computation is resumed after the cylinder is let to move in both streamwise and transverse directions. For the purpose of comparison with the experimental data of Griffin[67] several different combinations of structural parameters are used in the computations.

Morton et al.[30] suggested to use the reduced velocity $\bar{u} = \frac{1}{\pi St}$ such that the structural oscillator works under or near the resonance conditions. Therefore the computed St number from the stationary cylinder is used to determine $\bar{u}$. For all the cases of oscillating cylinder, St is set to be 0.2, corresponding to $\bar{u} = 1.5915$. Different mass ratios, μ_s, are used to test the different responses of the structural system. They are equal to 1.2732, 5.0, and 12.7324 respectively. To match the wide range of the experimental data, the damping ratio, ζ, is chosen from the range between 0.001 - 1.583.

The dimensionless physical time step $\Delta t = 0.05$ is used, which corresponds to approximately 100 time steps per period determined by the Strouhal number used. The CFL number for the pseudo time steps varies from case to case. For the large cylinder movement cases, smaller pseudo time steps are used to limit the displacement of the cylinder during each iteration.

For the cases computed, the CFL number varies from 5 to 500. The iteration number within one physical time step varies from 20 to 100. Fig. 12.24 shows a typical iteration history within one physical time step. Both the residual of the CFD solver and structure are reduced to machine zero. The structure solver usually converges faster than the CFD solver.

Figure 12.25 displays the computed vorticity contours around the oscillating cylinder. It shows how the vortexes are shed at the moment when the cylinder bounds back toward its mean position in y direction.

A typical trajectory of the center position of the moving cylinder is plotted in Figure 12.26, which is similar to the results computed by Blackburn et al.[68] and Alonso et al.[65]

All the numerical results for present study are plotted in Figure 12.27 for the three values of μ_s. Also plotted are the computations of Alonso et al. [65] with $\mu_s = 5.0$, computations of Morton et al.[30] with $\mu_s = 12.73$, and the experimental data of Griffin[67]. In the figure, the abscissa is the reduced damping with the form of $8\pi^2 St^2 \zeta \frac{m}{\rho D^2}$[68], and the ordinate is the cross-flow displacement of motion normalized by the diameter of the cylinder. Overall, very good agreement is observed between the present results and the experimental results, especially for the case of $\mu_s = 1.2732$. The figure shows that the higher values of mass ratios ($\mu_s = 5.0$ and $\mu_s = 12.7324$) give less satisfactory results than those with $\mu_s = 1.2732$, particularly at low damping ratios. However, they agree well with the results of Morton et al.[30] ($\mu_s = 12.73$).

8.3.3 Elastically Mounted Airfoil

As the validation of the Zha-Hu CUSP scheme for transonic airfoils, the steady state solution of the transonic RAE 2822 airfoil is calculated first. The freestream condition for this study are listed in Table 8.5 below.

Table 8.5: Free-stream condition for RAE 2822 Airfoil

Mach number	Static Pressure (psia)	Temperature (R)	Angle-of-Attack (deg)	Reynolds Number
0.729	15.8073	460.0	2.31	6.5×10^6

The turbulent Reynolds stress and heat flux is calculated by the Baldwin-Lomax algebraic model[48]. This case is run using an O-type grid with three different dimensions, they are 128×50×1, 256×55×1, and 512×95×1 respectively. The outer boundary extends to 15 chords from the center of the airfoil. The experimental data provided by Cook et al.[69] are available for validation. The comparison of pressure coefficient on the airfoil is shown in Figure 12.28. Overall, very good agreement is obtained between the computation and experiment for each mesh dimension, especially for the two larger ones which appear to be sufficient to capture the shock on the suction surface of the airfoil without using any limiter. The important aerodynamic coefficients from both simulation and experiment are summarized in Table 8.6.

Table 8.6: Aerodynamic coefficients and $y+$ for RAE 2822 Airfoil

Mesh Dimension	C_d	C_l	C_m	$y+$
128×50	0.01482	0.73991	0.09914	0.0833 - 2.3864
256×55	0.01455	0.73729	0.09840	0.1318 - 2.4016
512×95	0.01426	0.74791	0.09994	0.2309 - 2.0228
Prananta et al.[70]	0.01500	0.74800	0.09800	
Experiment	0.01270	0.74300	0.09500	

It can be seen in Table 8.6 that the predicted lift coefficients with all mesh dimensions agree well with the experiment. The computed drag and moment coefficients show larger errors, but they have the similar accuracy as those computed by Prananta et al.[70]. The relatively large error of the drag and moment may be mostly due to the inadequacy of the turbulence model, which is difficult to predict the surface friction accurately.

8.3.4 Forced Pitching Airfoil

As a validation case of the scheme for moving grid system, the forced pitching NACA 64A010 airfoil is calculated. For this transonic airfoil, the Reynolds averaged Navier-Stokes equations with Baldwin-Lomax turbulence model are solved. Similar to the previous computation of the flow over the stationary airfoil, an O-type mesh consisting of 280×65 cells is employed for the computations of forced pitching airfoil. The NACA 64A0101 airfoil is selected for this calculation because the experimental data is available. The fine mesh zone or the non-deforming part of the mesh is shown in Figure 12.29. The first grid point adjacent to the wall has the maximum $y^+ \leq 3.43$

The NACA 64A0101 airfoil is forced in pitch around its quarter chord sinusoidally. The angle of attack is imposed as a function of time as $\alpha(t) = \alpha_m + \alpha_o sin(\omega t)$, where α_m and α_o are the mean angle of attack and the amplitude of oscillation respectively.

The ω is the angular frequency which is directly related to the reduced frequency $K_c = \frac{\omega c}{2U_\infty}$, where c is the airfoil chord, and U_∞ is the free-stream velocity. To compare with the experimental results given by Davis[71], the primary parameters used in the computation are listed as follows: $\alpha_m = 0$, $\alpha_o = 1.01°$, $Re = 1.256 \times 10^7$, $M_\infty = 0.8$, reduced frequency, $K_c = 0.202$.

Again, the computation begins with the steady state flow field of the stationary airfoil at 0 degree angle of attack with a dimensionless time step $\Delta t = 0.1$. The transition period takes about 3 cycles and the results becomes periodic in time after that. Figure 12.30 shows the lift oscillation versus the angle of attack after the flow field reaches its temporally periodic solution. The computed lift oscillation agrees well with the experiment[71], which has an evident improvement compared to the recent result computed by McMullen et al. in 2002 [72].

Fig. 12.31 shows the computed moment coefficient compared with the experiment[71]. The computed moment coefficient does not agree as accurately with the experiment as the lift coefficient does. However the results are very similar to those predicted by Bohbot et al.[73] and McMullen et al.[72]. The large discrepancy between the computation and the experiment for the moment coefficient may be due to the inadequacy of the turbulence modeling, which may not predict the surface friction accurately.

8.3.5 Flow-Induced Vibration of NACA 64A010 Airfoil

Structural Models

The structural model for the flow-induced vibration of a 2-D sweptback wing with a NACA 64A010 cross-section is described in section. This model was first introduced by Isogai [74] [74], and has been numerically investigated by several researchers [10] [75] [70] [73].

The system of the elastically mounted airfoil is assumed to be undamped. The airfoil is allowed to move in pitch about a given elastic axis and plunge vertically. The pitch axis is defined by a distance a, which is the multiple of the semi-chord length with the origin point located at the mid-chord position. If a is positive, it means the axis is located downstream of the mid-chord, negative means being located upstream of the mid-chord point.

A sketch of the elastically mounted airfoil is depicted in Figure 12.21. The motion of such an elastic system can be described by using the following equations

$$m\ddot{h} + S_\alpha \ddot{\alpha} + K_h h = -L \tag{8.7}$$

$$S_\alpha \ddot{h} + I_\alpha \ddot{\alpha} + K_\alpha \alpha = M \tag{8.8}$$

where h and α are the plunging and pitching displacements respectively, m is the mass

per unit span, S_α is the static moment around the elastic axis, I_α is the rotational moment of inertia, K_h and K_α are plunging and pitching spring constants respectively, L is the lift force and M is the moment around the elastic axis. The equations of the structure motion (8.7) and (8.8) are normalized by using semi-chord b as the length dimension, the uncoupled natural frequency in pitch ω_α as the time scale, and are expressed as

$$\ddot{h} + x_\alpha \ddot{\alpha} + \left(\frac{\omega_h}{\omega_\alpha}\right)^2 h = -\frac{U^{*2}}{\mu\pi} C_l \tag{8.9}$$

$$x_\alpha \ddot{h} + r_\alpha^2 \ddot{\alpha} + r_\alpha^2 \alpha = \frac{U^{*2}}{\mu\pi} C_m \tag{8.10}$$

where x_α is the static unbalance, ω_h is the uncoupled natural frequency in plunge, r_α^2 is the squared radius of gyration, U^* is the reduced velocity defined as $\frac{U_\infty}{\omega_\alpha b}$, C_l and C_m are the lift and moment coefficient respectively. Since the time scale used in Equations (8.9) and (8.10) is different from the one used in the governing equations of flow, the structural dimensionless time t_s^* needs to be re-scaled and keep its consistency with the entire system during the computation, i.e., $t_s^* = \frac{\omega_\alpha L}{U_\infty} t_f^*$, where t_f^* is the dimensionless time for flow and the L is the length scale. Finally the equations are cast into the form of Equations (8.5) and (8.6), and the corresponding matrices are

$$\mathbf{S} = \begin{pmatrix} h \\ \dot{h} \\ \alpha \\ \dot{\alpha} \end{pmatrix}, \mathbf{M} = \begin{pmatrix} 1 & 0 & 0 & 0 \\ 0 & 1 & 0 & x_\alpha \\ 0 & 0 & 1 & 0 \\ 0 & x_\alpha & 0 & r_\alpha^2 \end{pmatrix}, \mathbf{K} = \begin{pmatrix} 0 & -1 & 0 & 0 \\ \left(\frac{\omega_h}{\omega_\alpha}\right)^2 & 0 & 0 & 0 \\ 0 & 0 & 0 & -1 \\ 0 & 0 & r_\alpha^2 & 0 \end{pmatrix}, \mathbf{q} = \begin{pmatrix} 0 \\ -\frac{U^{*2}}{\mu\pi} C_l \\ 0 \\ \frac{U^{*2}}{\mu\pi} C_m \end{pmatrix}.$$

The structural parameters used in this model are listed as the following: $a = -2.0$, $x_\alpha = 1.8$, $\frac{\omega_\alpha}{\omega_h} = 1$, $r_\alpha^2 = 3.48$, and $\mu = 60$. The elastic axis is located half a chord upstream of the airfoil nose.

The unsteady Reynolds averaged Navier-Stokes equations with the Baldwin-Lomax turbulence model are solved for the flow field in this study. The freestream conditions are: $Re = 1.256 \times 10^7$, $M_\infty = 0.825$.

Due to the symmetric profile of the NACA 64A010 airfoil, an initial perturbation is imposed to trigger the oscillating motion. The airfoil is forced to rotate sinusoidally about its elastic axis at the natural frequency in pitch ω_α with an angle of attack amplitude, $\alpha_o = 1°$. Usually the forced pitching mode lasts for 1 - 3 cycles. After that, the elastically mounted airfoil is let to move in both plunging and pitching directions, and then the dynamic response is recorded.

In present study, the search of the critical point on the transonic flutter boundary at a given *Mach* number is conducted. The speed index, V^* defined as $\frac{U^*}{\sqrt{\mu}}$, is the parameter to classify damped, neutral and divergent responses of the airfoil when the *Mach* is fixed. In this case, the total pressure and temperature need to be adjusted

to match the certain value of the Re number. Several calculations are needed to determine the critical point using a bi-section method.

In Figures (12.34) through (12.36) the time histories of plunging and pitching displacements at $M_\infty = 0.825$ are plotted for three different V^*. In these figures, from $V^* = 0.55$ to $V^* = 0.70$, the plots correspond to the damped, neutral, and diverging responses respectively. The major task of calculating a flutter boundary is to locate where the neutrally stable (critical point) is by looking at those plots and determining where the neutral response occurs as the V^* varies. When the value of V^* is smaller than the critical value on the flutter boundary, both plunging and pitching displacements decay corresponding to the damped response as shown in Figure (12.34). Once the value of V^* coincides with or is close to the critical value, the neutral response appears as shown in Figure (12.35). Any value of V^* beyond the critical value, a diverging response is expected as shown in Figure (12.36). Mach number 0.825 is located at the bottom of the sonic dip as reported in[5, 70, 73]. The predicted critical velocity index $V^* = 0.615$ is consistent with the results computed by those researchers.

8.3.6 2D Airfoil Flutter Boundary Prediction

After the validation of the flow induced vibration of NACA 64A010 Airfoil in chapter 8.3.5, a search of the flutter boundary is conducted. This is ultimately the most important results needed for an aircraft and engine design engineer to determine if the design is located within the safety margin.

At each Mach number, several calculations are needed to determine the critical point on the flutter boundary using a bi-section method. At certain $Mach$ number, the flutter boundary is very 'thin', and more calculations are necessary to really capture the critical points. The dynamic response immediately after the transonic dip becomes very complex, and locating the flutter boundary in that region ($Mach$ = 0.875 - 0.9) is very difficult and time-consuming.

The V^* and the frequency ratio $\frac{\omega}{\omega_\alpha}$ for the flutter boundary are plotted versus $Mach$ number in Figures (12.37) and (12.38) respectively. Also plotted in the figures are the results from two other computations by Prananta et al. [70] and Bohbot et al. [73]. The $Mach$ number for the bottom of the transonic dip of 0.825 is consistent with their results.

Overall, the present results compare well with the results of of Prananta et al. and Bohbot et al. except that both values of V^* and $\frac{\omega}{\omega_\alpha}$ ratio are higher at high $Mach$ number region ($Mach = 0.925$ to 0.95). The primary difference between the present results and their results are: 1) The present results are based on fully coupled fluid-structure interaction. Their results are loosely coupled; 2) The Reynolds number of the present results is about twice higher. Both the present results and Prananta et

al. are based on the same Baldwin-Lomax turbulence model. To study the effect of Reynolds number, the flutter boundary at $Mach = 0.925$ and 0.95 are re-calculated with the same Reynolds number (6×10^6) used by Prananta et al. The difference is small. Hence, the difference between the present results and the results of of Prananta et al. and Bohbot et al. may be due to the fully coupled and loosely coupled algorithm. Since there are no experimental results for comparison, it is difficult to judge which result is more correct.

Except the flutter boundary, the present solver also has captured the Limit Cycle Oscillation (LCO) phenomenon as shown in Figure (12.39). LCO occurs when the velocity index is greater than the flutter velocity index[76]. The amplitude is large, but stable. LCO is considered due to the nonlinear nature of the shock boundary layer interaction occurring for transonic airfoil[76, 73]. Figure (12.40) presents a different LCO with the second torsion mode more dominant.

Figure (12.41) shows an interesting situation happening at $Mach = 0.875$ and in the area of $V^* = 2.5$. Both plunging and pitching displacements of the system increase rapidly immediately after the airfoil is set to be free, but then gradually reach their steady state positions and stay there through the end of the computation. Under this flow condition, the aerodynamic forces and moments are balanced by the structure system. The angle of attack is stabilized at 2.9° and is in the range of the cruise point which should be stable. This situation is only observed at $Mach = 0.875$, and maybe named as 'standing'. The V^* of the standing phenomenon is not located at one point, but a region around $V^* = 2.5$. The results and flow conditions of the 'standing' phenomenon needs to be confirmed by experiment.

8.4 SNM Model Used for Transient Response

A structural model is developed to simulate the transient response of a blade disk structure. This model implements the original SNM theory (for steady state responses) and expands it to simulate transient responses. The study discussed in this section assumes that the fluid forcing function is prescribed such that the transient response can be carried out in the transient simulation of ANSYS. The prescribed forcing function however does have multiple frequency components with all but one primary frequency components decaying in time.

Fig. 12.42 shows a finite element model of 24-blade disk with dynamic characteristics similar to a typical high compressor rotor. The finite element mesh is rather coarse for the purpose of tractable computational cost in ANSYS benchmark computation. When studying a realistic case, the mesh needs to be finer. The transient responses of this model were computed by two methods: In the first method, the transient responses were calculated using the "Full Solution" function in ANSYS which utilizes full system matrices (instead of reduced modal matrices in "Reduced Solu-

tion" function) to avoid modal truncation error. The second method computes the transient responses based on the SNM method. The SNM results are then compared with the ANSYS benchmarks.

Both low frequency response and high frequency response of a tuned bladed disk were studied.

8.4.1 Low Frequency Case

The blade tips are driven by prescribed forces with a circumferential pattern of zero nodal diameter. The force is given by Eq.8.11,

$$f(t) = f_{dc} + f_0 sin(\omega t) + f_1 cos(1.4\omega t)e^{\omega t/1000} + f_2 sin(0.7\omega t)e^{\omega t/2000} \tag{8.11}$$

with $f_{dc} = 0$,$f_0 = 1$, $f_1 = 0.5$, $f_2 = 2$, and $\omega = 500$Hz. Note that the lowest natural frequency of all zero nodal diameter modes is 495 Hz. The overall time history of the force is shown in Fig. 12.43. Fig.12.44 shows that multiple frequency contents (0.7ω, ω, and 1.4ω) co-exist in the forces at the beginning of the simulation and Fig. 12.45 shows that only the primary frequency component (ω) survives at the end the simulation. The forcing function is chosen so to mimic the dynamic pressure of a fluid field and to examine the accuracy of the SNM model.

Fig. 12.46 shows the envelopes of the responses of a tip node of a blade computed by SNM and ANSYS. 24 modes of one blade mode family was used in the SNM simulation. Closer inspections of the SNM and ANSYS results shown in Fig. 12.47 and Fig.12.48 verify that SNM is very accurate in predicting the transient response for this case.

A worthy note is that the numbers of degrees of freedom in the ANSYS and SNM simulations are 2256 and 24 respectively. The time saving of SNM is about 2 orders of magnitude over this simplified ANSYS model. In the case of a realistic ANSYS model, the time saving would be much greater.

8.4.2 High Frequency Case

In the high frequency case, the blade tips are again driven by prescribed the forces defined by Eq. (8.11) with a circumferential pattern of zero nodal diameter. The parameters of the force are $f_{dc} = 0$,$f_0 = 1$,$f_1 = 0.5$, $f_2 = 2$, and $\omega = 2500$ Hz. Note that the 3rd natural frequency of all zero nodal diameter modes is 2506 Hz. The overall time history of the force is shown in Fig. 12.49. Fig. 12.50 and 12.51 show that multiple frequency contents (0.7ω, ω, and 1.4ω) of the force co-exist at the

beginning of the simulation and only the primary frequency component (ω) survives at the end the simulation.

Fig. 12.52 compares the envelopes of the responses of a tip node of a blade computed by SNM and ANSYS. Only 24 modes of the 3rd blade mode family were used in the SNM simulation. Fig. 12.53 and Fig. 12.54 are closer examination of the responses. It is apparent that SNM does not capture the response well initially when the forcing frequency components and are yet to die out but does capture the response quite well at the end when the primary frequency component dominates. This is because of the lack of low and high frequency modes in the SNM model. In this case, the SNM model actually acts as a frequency filter of the overall system. When long term steady state solution is of the only interest, an SNM model with a single blade mode family might be desirable.

To further verify the above statement, an SNM model with the 3rd blade mode family and the neighboring families (2nd and 4th blade modes) was used for the computation. Fig. 12.55, 12.56, and 12.57 compare the responses computed by SNM and ANSYS. They show good agreement between SNM and the ANSYS benchmark. Notice that the number of degrees of freedom in the 3-family SNM model is 72. The time saving of SNM is about 1.5 orders of magnitude over the ANSYS model.

8.5 Non-Reflective Boundary Conditions

8.5.1 A Vortex propagating through a outflow boundary

The first test case is a subsonic vortex propagating flow in an open flow field. The computed domain is rectangular inclined 30° about the horizontal axis as a validation for the generalized coordinates. The subsonic inflow and outflow boundary conditions are used at the inlet and exit, and far filed boundaries are used on the upper and lower borders. In [33], a supersonic vortex propagating flow is chosen. It is known that a subsonic vortex propagating flow is more difficult to deal with since the disturbance propagates both upstream and downstream. To test present method under more general conditions, the subsonic vortex propagating flow is selected for this study.

The computational mesh has a length of 2 units in streamwise direction which is 30 degrees to the x direction, while the width is 4 units in transverse direction. The mesh dimensions are 60×100. The laminar Navier-Stokes equations is solved for this flow with $M = 0.8$ and Reynolds number of 300.

A vorticity is initially located at the center of the domain when dimensionless time $t^* = 0$, and convected downstream toward the outflow boundary. The velocity flow field is initially specified as

$$\begin{pmatrix} u \\ v \end{pmatrix} = \begin{pmatrix} u_\infty \\ v_\infty \end{pmatrix} + \begin{pmatrix} \frac{\partial \psi}{\partial y} \\ -\frac{\partial \psi}{\partial x} \end{pmatrix} \tag{8.12}$$

$$\psi = C_v exp\left(-\frac{x^2+y^2}{2R_c^2}\right) \tag{8.13}$$

where u_∞ and v_∞ are the velocity components of the incoming flow, C_v is the coefficient that determines the vortex strength of the velocity field, and R_c is the vortex radius. The total energy field is initialized as

$$\rho e = \rho e_\infty + \rho \frac{C_e^2}{R_c^2} exp\left(-\frac{x^2+y^2}{2R_c^2}\right) \tag{8.14}$$

where C_e is the coefficient that determines the vortex strength of the total energy field. Equations (8.12) and (8.14) are adopted from those used by Poinsot and Lele[33]. The coefficients C_v and C_e, and radius R_c are defined by

$$C_v/(cL) = -0.0005, \quad C_e/(cL) = -0.02, \quad R_c = 0.15 \tag{8.15}$$

The inflow and outflow boundary conditions used in this case are described in previous section. The far field upper and lower boundaries are treated as perfect non-reflective outflow boundary.

The flow field at inflow boundary is initially set to be uniform. The direction of the incoming flow is parallel to the constant η lines. Obviously, at the inflow boundary, the transverse flux and viscous terms are very small. The error caused by LODI relations is very small and negligible.

To compare the present NRBC with the commonly-used outflow boundary conditions (FPBC) in which the fixed downstream pressure is imposed for subsonic flow simulations, the first computation is carried out with FPBC, which includes: at inflow boundary, u_o, v_o, ρ_o are given such that the streamwise velocity component is uniformly distributed and the transverse velocity component is equal to zero, the pressure is extrapolated from the interior domain, $p_o = p_i$, then the total energy ρe_o can be computed from the equation of state; at outflow boundary, all the primitive variables are extrapolated from the inner domain except the pressure is set to be constant. The CFL number of the pseudo time step is 500. The physical time step CFL is 0.74, which is determined by the time accuracy of the physical problem

The same case with the same initial flow condition and same CFL number is then calculated using the NRBC developed in present study. The value of σ in Equation (5.27) is set to be 0.25. Figures 12.58 and 12.59 show the computed density contours at four instants by FPBC and NRBC respectively. It can be seen from figure 12.58 that the flow field is seriously distorted by the reflective waves when the vortex propagates

through the exit boundary. But there is no noticeable distortion in the solution calculated using NRBC as shown in figure 12.59. The vortex passes through the outflow NRBC very smoothly. Figures 12.60 and 12.61 show the relative streamwise velocity component, $(u^{\tau} - u^{\tau}{}_{\infty})/u^{\tau}{}_{\infty}$ contours at the same four instants by FPBC and NRBC respectively. The same phenomenon is observed. Figure 12.62 shows the time histories of $|p_{max} - p_{min}|$ for the full course of the computation. As can be seen, the level of spurious pressure reflection caused by FPBC is much higher than the one by NRBC.

8.5.2 Inlet-Diffuser Flow

To test the non-reflective boundary conditions for realistic engineering problems. A transonic inlet-diffuser with shock wave boundary layer interaction [62] is computed to demonstrate the advantage of the NRBC.

8.5.3 Steady State Solutions

The steady state solution of the inlet diffuser is calculated first to verify that the NRBC is consistent with the steady state flow. The Reynolds Number is 3.45×10^5 and the inlet Mach number is 0.46.

The baseline geometry of the inlet diffuser has a height of $H = 4.4cm$ at the throat and a total length of $12.6H$. This case is run using a H-type grid with the dimensions of 110×56. The turbulence shear stress and heat flux are calculated by the Baldwin-Lomax model[48]. The experimental data provided by Bogar et al.[62] are available for validation.

As discussed before, for 3-D case, at $\xi = 1$ inlet boundary, waves $\mathcal{L}_1$ - $\mathcal{L}_4$ enter the boundary and $\mathcal{L}_5$ leaves. Hence four physical boundary conditions are required at this boundary. The amplitude of the outgoing characteristic wave $\mathcal{L}_5$ can be estimated from the interior points.

According to [33], the inlet and wall NRBC are not as critical as the exit NRBC. For this transonic inlet-diffuser case, at the upstream of the shock, the flow is supersonic. Hence the perturbation will not propagate upstream. The NRBC at inlet therefore may not be necessary. The conventional boundary condition at inlet is expected to work well. However, at the downstream of the shock, the flow is subsonic. The oscillation of the shock will generate strong reflecting waves at the exit boundary. Therefore exit NRBC is essential for this case. For this reason, the inflow NRBC is not used in this study. Instead, the inlet BC with given total pressure P_t, total temperature T_t, and flow angle is used. The NRBC outflow and wall conditions used are those described in previous section.

The $Mach$ number contours are shown in Figure 12.63. Corresponding to different

back pressure in the experiment, there are two cases of the flow, one has a weak shock (p_{outlet}/p_t=0.82) and the other has a strong shock (p_{outlet}/p_t=0.72). Figures 12.64 and 12.65 show the computed static pressure distributions compared with the experimental data along the top and bottom wall for the weak shock case. Good agreement is obtained between the computation and experiment.

Figures 12.66 and 12.67 show the static pressure distribution compared with the experimental data along the top and bottom walls for the strong shock case. Due to the strong shock interacting with the turbulent boundary layer, there is a flow separation downstream of the shock, which is not well predicted. There may be two reasons for the problem: 1) the flow is unsteady due to the separation and hence the steady state solution can not capture the separation bubble length correctly; 2) the Baldwin-Lomax turbulence model is inadequate to handle the non-equilibrium separated flow.

Different σ values from 0.1 to 0.35 are tested and the results show that the steady state results are insensitive to the σ value. The fixed pressure boundary conditions are also applied to the same case, and achieve almost the same results as those computed by the NRBC. This is because that, for the steady state solutions, the reflective waves are eventually diffused when the steady state solution is converged.

8.5.4 Unsteady Solutions

The steady state calculation indicates that the NRBC is not essential since the artificial reflective waves are diffused when the solution is converged. However, it is very different when the unsteady flow is calculated. For the inlet-diffuser case with a strong shock wave, the fixed pressure outflow boundary conditions (FPBC) generates strong reflective waves and makes the shock wave severely oscillating inside the duct. The amplitude of the oscillation is far greater than the experimental results. When the NRBC is applied, the shock oscillation is dramatically reduced.

Figures 12.68 and 12.69 show the time averaged pressure distributions compared with the experimental data. The CFL number of the pseudo time step is equal to 5 for all the cases. The CFL number of the physical time step is about 3000, which gives 132 steps in a shock oscillation cycle of the computed dominant frequency 260(Hz). The value of σ in Equation (5.27) is 0.25. Due to the large shock oscillation, the shock location is smeared out for the fixed pressure outflow boundary conditions (FPBC). Hence the shock location, strength and the pressure downstream of the shock are poorly predicted. When the NRBC is applied, the reduced shock oscillation yields sharp shock profile and much better agreement of the shock location with the experiment.

To match the experimental geometry for the measured shock oscillation frequency, the computational domain is then extend to a total length of $21.3H$. The simulation

is carried out with FPBC and NRBC respectively using the same flow conditions. The computed and experimental power spectra for the static pressure at the exit location ($x/H = 14.218$) are shown in Figure 12.70. The experimental spectrum (the bottom one) of the shock oscillation measured for this case has one dominant frequency around 200 (Hz)[62]. The power spectrum computed by NRBC in the middle plot shows that there is only one significantly dominant frequency at about 260 (Hz). The power spectrum computed by FPBC in the top plot has the dominant frequency at 380 (Hz), which is obviously very different from the dominant frequency of the experimental value of 200 (Hz). Obviously, NRBC gives better results than the FPBS does, which is also better than the computed value of 317 (Hz) predicted by Hsieh et al. [77]. It is evident that the NRBC improves the numerical accuracy by reducing the false reflections, and the noise level created by NRBC is also much lower than the one created by FPBC. The results show that the NRBC is essential to accurately predict unsteady aerodynamic forcing.

8.6 Separated Flow of NASA 3D Flutter Cascade

NASA GRC conducted compressor cascade wind tunnel tests to mimic the flow field of transonic compressor blade flutter[78][79]. The cascade is shown in fig. 12.71. As the first validation step, the steady state solution of the 3D cascade is calculated. The 3D effect of the flow field is from two aspects: 1) the cascade geometry is different near the end walls so that the blades can be mounted; 2) there is no endwall boundary suction. Hence the endwall boundary layer will create the 3D effect in the spanwise direction. The parameters used in the calculation is listed in Table 8.7.

Chord	$8.89cm$
Stagger angle	60°
Solidity	1.52
Reynolds number	1.522×10^5
Inlet Mach number	0.5
Mesh size	$150 \times 60 \times 40$
CFL	5.0

Table 8.7: NASA 3D Flutter Cascade

The 3D mesh is shown in Figure 12.72. The mesh is highly clustered near the cascade surface and the end walls to make sure y^+ is within the range of 3. The mesh is also clustered around leading edge and trailing edge. In Figure 12.73, the 2D mesh of the top, midspan and bottom planes are plotted, which indicate the geometry variation.

The boundary conditions are set as the following: at subsonic inlet, total pressure

and total temperature are specified; at subsonic outlet, the static pressure is specified; no slip adiabatic wall boundary condition are applied to bottom, top end walls and the cascade surfaces; periodic boundary conditions are used in the pitch direction upstream and downstream of the cascade wall surfaces.

8.6.1 Steady state results

Though the flow is separated and unsteady when the incidence is high, the time averaged flow field is calculated with the local time stepping enabled and the dual time stepping disabled in the code. The solution is obtained when the calculated flowfield is unchanged. The steady state solution is also used as the initial solution for the corresponding unsteady calculation.

At incidence angle of 0°, the computed midspan surface static pressure distribution is in a very good agreement with the experimental measurement[79] as shown in Figure 12.74.

An incidence of 10° is chosen for the following numerical study. The *van Leer* scheme is used to evaluate the inviscid flux. Though the *van Leer* scheme is more diffusive than the *Roe* schemee, when working with the *Baldwin-Lomax* turbulence model, it gives better agreement with the experiment in the current code. The *Roe* scheme predicts the separation larger than the experiment. The inlet Mach number is obtained by adjusting the back pressure level.

The result of the case with inlet Ma=0.5 is described in this section to demonstrated the characteristics of the 3D separation flow field. More results for Ma=0.8 and Ma=1.18 can be found in [80]. In the case of Ma=0.5, the corresponding *Reynolds* number is 9.6699×10^5. The CFL in the *Gauss-Seidel* iteration is 5.0. The calculation starts from a flowfield at rest.

The flow stream lines on the mid-span plane is shown in Fig. 12.75. The flow exhibits a large separated region on the suction surface that starts immediately at the leading edge and extends down to 45% of the blade chord. The flow pattern on the suction surface is plotted on the left in Fig. 12.76. The separation region has a parabola shape, which is approximately symmetric about along the blade mid-span line and extends to the blade upstream corners. Two counter rotating vortexes are formed downstream of the blade leading edge corners on the suction surface at its two ends. The experiment visualization with dye oil technique is shown in Fig. 12.76 on the right. The computation results agree with the experiment fairly well, except that the numerical results shows a fuller separation region in span-wise direction.

The mid-span static pressure distribution is plotted and compared with the experiment measurement in Fig. 12.77. A reasonable agreement is achieved. The pressure

is expressed as the pressure coefficient,

$$C_p = \frac{p - p_{in}}{\frac{1}{2}\rho_{in}U_{in}^2}$$

where p is the local static pressure. p_{in}, ρ_{in} and U_{in} are the averaged static pressure, density and velocity at the inlet.

On the leading edge of the suction side, the numerical pressure results varies more steeply than that given by the measurement. The separation region denoted by the cross of the pressure distributions on suction and pressure surfaces agrees very well with the experiment.

The separation region is enlarged when *Roe* scheme is used to calculate the inviscid flux. A possible reason for the difference is the application of turbulence model on the H-type mesh in the current code. It is shown that the implementation details the *Baldwin-Lomax* model is vital to the resulted turbulent viscosity accuracy. Better agreement is obtained in [81] for the same case, where the *Roe* scheme is applied on an O-type mesh. The H-type mesh in the current code is generated by an elliptic method as a whole, which meets difficulty in the mesh orthogonality in the wall boundary region, which affects the accuracy in calculating the outer layer eddy viscosity coefficient. A two-layer H-type mesh is used in [82], where an inner algebraic mesh is surrounded by an outer elliptic method generated mesh. The the inner mesh is designed to achieve better orthogonality. These grid generation techniques will be implemented in the code in the next step research work.

8.6.2 Unsteady separated flow simulation

The separation is believed to bring high unsteadiness to the cascade flow pattern. The inlet Mach number is an important factor which affects the separation characteristics[80]. To study the influence of the inlet Mach number on the unsteady characteristics of the separated flow, numerical simulation is carried out for high incidence angle cases with Mach number 0.5, 0.8 and 1.18. Each unsteady calculation is carried out based on its corresponding steady state result.

Due to the limitation of the computation capability, the physical time interval is chosen as large as 10% of the characteristic time of the cascade, $t_c = c/U_{in}$. $U_{in}$is the inlet velocity. This time interval varies with the inlet Mach number. The CFL number used in the pseudo time *Gauss-Seidel* implicit iteration is 20.0. Twenty pseudo time steps are used for each physical time step. Two parameters are recorded to analyze the unsteady characteristics of the separation flow. The first is the mid-span separation bubble length(x), which is marked by the streamwise zero velocity point at the first inner mesh point on the suction surface. The second parameter is the unsteady static pressure (p) measured at the location of 13% downstream the leading edge on the

suction surface, which is the same as the experiment measurement location. The unsteady pressure is refereed as "check point pressure" in the following.

Ma = 0.5

In the case of Ma = 0.5, the physical time interval is set as 0.052744 ms.

Fig. 12.78 shows the time history of the separation length oscillation in a time segment of 16 ms ($30t_c$). The separation length increases rapidly from $0.45c$ to $0.66c$ in the first 1.63 ms ($3t_c$) and then decreases to $0.63c$ at t =2 ms ($3.8t_c$). The separation region then grows up again toward downstream to $0.73c$ at t =3 ms ($5.7t_c$). With the time progressing, the separation region boundary oscillates back and forth on the suction surface. The average length tends to increase gradually until a periodic state is reached after 4.4 ms ($8.3t_c$). The oscillation of the separation length is between $0.73c$ and $0.76c$ with a fixed cycle. The periodicity information is clearly extracted using the FFT technique. The separation region oscillation spectra is calculated from the unsteady data after 4.4 ms ($8.3t_c$). The frequency spectrum is shown in Fig. 12.79, which clearly shows a peak at 770 Hz. This indicates the separation length oscillates with a period of 1.25 ms ($2.37t_c$).

Compared with the steady state solution, the unsteady separation calculation results in larger separation size. The reason is not clear.

The unsteady check point pressure data shows similar characteristics of the unsteady separation flow. Fig. 12.80 shows a segment of 16 ms ($30t_c$) pressure oscillation data. The pressure start at p =2.659 from the steady state results. The oscillation is between p =2.68 and p =2.72 after t =4.4 ms ($8.3t_c$). The oscillation amplitude is about 1.5% of the averaged pressure level. The frequency spectrum is shown in Fig. 12.81 with a peak at 770 Hz.

The mechanism behind the unsteady characteristics of the separation is illustrated in Fig. 12.83, where the evolution of a separation oscillation cycle is plotted. The stream lines at 8 time steps show the leading edge vortex shedding development. There are 4 physical time steps (0.21 ms, $0.4t_c$) between 2 sequential plots. The relationship between the oscillation of the pressure and the separation length is shown in Fig. 12.82.

At the starting time level a (t =4.4305 ms, $8.4t_c$), the separation region has just passed the maximum length location. There are 2 vortexes in the separation bubble. They are rotating in the same direction. The check point pressure is going up. At time level b (t =4.6415 ms, $8.8t_c$), the two vortexes are pushed toward downstream. The second vortex diminishes. The first vortex grows quickly and becomes the only vortex in the separation bubble. The separation region becomes thicker in the span-wise direction, but shorter in the stream-wise direction. The surface check point pressure reaches its maximum level at this time level. At time level c (t =4.8524 ms,

$9.2t_c$), the separation bubble approaches its shortest length in stream-wise direction, and maximum thickness in the span-wise direction. The check point pressure is going down. At time level d (t = 5.0634ms, $9.6t_c$), the separation bubble has passed the minimum length location, and begins to extend toward downstream. The check point pressure is still going down. At time level e (t =5.2744 ms, $10.0t_c$), a new vortex is generated at leading edge and becomes the first vortex. The check point pressure reaches its minimum value. The separation length is still increasing. At time level f (t=4854 ms, $10.4t_c$), the first vortex continues to grow. The second vortex is pushed toward downstream. Both the check point pressure and the separation length are going up. The latter is approaching its maximum location. At time level g (t =5.6964 ms, $10.8t_c$), the two vortexes have almost the same size, the flow structure is close to the starting time level a. The separation boundary has passed its maximum location and begin to shrink toward upstream. The check point pressure is going up. At time level h (t =5.9073 ms, $11.2t_c$), the second vortex diminishes. A new cycle is started at this time level.

The leading edge vortex shedding exhibits obvious periodical pattern in its evolution process. The leading edge keeps generating new vortexes. The new vortex pushes the old vortex bubble toward downstream and the old vortex decreases in size at the same time. When the two vortexes become of the same size, the maximum separation length is reached, where the separation bubble has the thinnest size in span-wise direction. As the new vortex grows further, the old vortex will diminish. The separation bubble will move upstream and makes the bubble thicker. The leading edge surface check point pressure reaches its maximum level when the separation bubble shrinks and reaches its minimum level when the separation bubble boundary extends. The vortex generation, pressure variation and separation length oscillation have the same frequency characteristics with a phase difference as shown in Fig. 12.82. Such oscillation is maybe one of the reasons to cause to flutter.

Ma = 0.8

The physical time interval used in the calculation for the case of *Mach* number 0.8 is 0.0342 ms. A similar flowfield unsteady characteristics is exhibited in the computation results.

Fig. 12.84 and Fig. 12.86 show the separation length and the checkpoint static pressure oscillation history in a time period of 21 ms. A clear periodicity is shown in these two figures. It is found in the time averaged steady state study in [80] that, the increase of the inlet Mach number will enlarge the separation bubble in size. Fig. 12.86 indicates that the inlet Mach number increase also increases the amplitude of the pressure oscillation. The oscillation amplitude is increased to about 5% of the averaged pressure level. The increased kinetic energy in the inflow bring higher unsteadiness intensity to the separated flow filed.

The corresponding FFT frequency analysis is shown in Fig. 12.85 and Fig. 12.87 respectively. The frequency analysis is based on the oscillation data after t=5 ms. The unsteady separation flow exhibits higher oscillation frequency because of the increased inlet Mach number. A clear frequency spectrum peak is shown at 1400 Hz in both figures, twice the frequency in the case of Ma = 0.5.

Ma = 1.18

In the steady state simulation of the cascade at Ma=1.18 in [80], the separation flow characteristics are very different from those at subsonic. The further increased kinetic energy in the inflow makes the flow attached to the blade surface in the leading edge. A smaller sized separation region appears after the shock wave because of the interaction of the shock wave and the turbulent boundary layer. The separation bubble shrinks in size and is located only in a small region at the center of the suction surface region.

The physical time interval in the calculation is set as 0.02483 ms. The pressure check point is located outside of the separation region in the supersonic case. The pressure oscillation history is shown in Fig. 12.88. The oscillation amplitude is very small compared to the cases of Ma = 0.5 and Ma = 0.8. The flow tends to steady at the leading edge. The pressure oscillation frequency spectrum is shown in Fig. 12.89.

The computed characteristics of the separation flow above is similar to the experiment measurement in [83]. In [83], when the blade is fixed, the blade surface pressure for low subsonic inlet flow at Ma=0.5 and low supersonic inlet flow at Ma=1.1 exhibits very low unsteadiness and very strong self-induced oscillations with a frequency of 110Hz is observed in high subsonic inlet flow at Ma=0.8. However, the strong low frequency oscillation is attributed to the tunnel resonance characteristics instead of the flow unsteadiness due to the flow separation in [84]. Even though, the cascade flow separation is believed to have a direct relation with the wall surface pressure unsteady oscillation, which is an important factor to the flutter. Further detailed numerical research is necessary to discover the mechanism.

8.7 Forced Vibration of the NASA Flutter Cascade

8.7.1 Parameters used in flow analysis

The steady state static pressure coefficient is defined as the following,

$$C_p\left(x/c\right) = \frac{p\left(x/c\right) - p_\infty}{\frac{1}{2}\rho_\infty U_\infty^2} \tag{8.16}$$

where p_∞, ρ_∞ and U_∞ are the averaged pressure, density and velocity at inlet.

The blades vibrate harmonically with a constant IBPA. The motion of the nth blade is defined by the blade deflection angle[?],

$$\alpha^n(t) = \alpha_0 + \hat{\alpha} Re\left[\exp\left(i\left(\omega t + n\beta\right)\right)\right] \tag{8.17}$$

where n is the blade index, t is the time, α_0 is the deflection angle at the mean blade position, $\hat{\alpha}$ is the amplitude of blade deflection, Re denotes the real part of a complex value, ω is the angular frequency, β is the inter blade phase angle.

The reduced frequency k_c is defined based on the chord length C as the following,

$$k_c = \frac{\omega C}{U_\infty} \tag{8.18}$$

The first harmonic unsteady pressure coefficient is defined as,

$$C_p(x) = \frac{p_1(x)}{\rho_\infty U_\infty^2 \hat{\alpha}} \tag{8.19}$$

where $p_1(x)$ is first harmonic pressure along the blade surface. It is a complex value obtained from the unsteady pressure signals using the Fourier transformation. $p_1(x)$ has a phase angle relative to the blade motion α.

The time dependent aerodynamic moment coefficient is defined as,

$$C_m(t) = \frac{-\int \mathbf{r} \times p(x)\,\mathrm{ds}}{\frac{1}{2}\rho_\infty U_\infty^2 \hat{\alpha}} \tag{8.20}$$

where $p(x)$ is the unsteady pressure along the blade surface, $\mathbf{s}$ is the surface area vector pointing outward from the blade, $\mathbf{r}$ is the vector pointing from the pivot location to an arbitrary point x on the surface.

The imaginary part, or the out of phase part of the unsteady pressure determines the damping or excitation of the blade motion. The aerodynamic damping coefficient is defined as,

$$\Xi = -Im\left(C_m\right) \tag{8.21}$$

where Im denotes the imaginary part of a complex value. A positive Ξ corresponds to a damped oscillation.

8.7.2 The Cascade

The NASA Lewis Oscillating Cascade test section consists of 9 identical airfoils with the cross section similar to the tip airfoil of modern low-aspect ratio fan blades[?].

The airfoil has a chord of 8.89 cm and is installed with a stagger angle of 60°. The solidity is 1.52. In the experiment, the inlet Mach number is 0.5. All blades vibrate simultaneously along a pitching axis at 0.5 chord with a constant IBPA of 180°. The oscillating amplitude is 1.2° and the reduced frequency based on chord varies at 0.4, 0.8 and 1.2. The blade motion is identical on every other blade. The two neighboring blades always vibrate in opposite direction.

The inlet Mach number $Ma = 0.5$ is achieved by adjusting the outlet static pressure level. The Reynolds number based on the chord length is 9×10^5. The flow incidence is 0°. For the unsteady dual-time stepping, one physical blade oscillation cycle is divided into 100 time intervals and 100 pseudo time Gauss-Seidel iterations are carried out for each physical time step. The 100 pseudo time iterations are proved to be sufficient to obtain a converged solution within a physical time step with the residual reduced by 3 orders in magnitude. Before the unsteady simulation, the corresponding steady state calculation is carried out to obtain the initial flow field for the unsteady computation. The inlet flow angle is adjusted to 61° to obtain good agreement with the steady state experimental surface pressure distribution.

Before the full scale computation, a simplified 2-passage cascade is computed with a reduced frequency of $k_c = 0.8$ by applying the periodic boundary condition. The information of the moving mesh and the conservative variables are exchanged across the periodic boundary. The multi-passage full scale simulation is then conducted for the 9-blade cascade with the wind tunnel side walls for more realistic results. The periodic boundary condition is not needed. The vibration frequencies of k_c=0.4, 0.8 and 1.2 are calculated and compared with the experiment measurement. The influence of the end walls are studied by comparing the results of k_c=0.8 from both simulations.

8.7.3 Computation domain decomposition and mesh generation

As shown in Fig. 12.107, the computation domain which is consistent with the experiment configuration is split into 10 subdomains based on flow passages P1 through P10. The 10 subdomains are computed by 10 CPUs running in parallel. The subdomains are separated from their neighbors by the blade surfaces B1 through B9 and the MPI interface boundaries. The MPI interface boundaries are straight lines passing through the leading edge (LE) and trailing edge (TE) of the blades with appropriate angles in accord with the local flow direction. The pitchwise distance between the end wall and the blade is half of the inner pitch distance. The US (upper surface) is the suction surface and LS (lower surface) is the pressure surface.

The inlet and outlet boundaries are set as 1.5 and 3 times chord length away from the airfoil LE and TE in axial direction. A part of the mesh is shown in Fig. 12.108

with the regions of LE and TE zoomed in for more details. The H-type mesh is generated for each subdomain respectively. Each subdomain shares the grid point distribution on the common MPI interface boundaries with its neighbors. To achieve good orthogonality on the blade surface, an additional algebraic boundary layer mesh is generated in the wall surface region. As shown in Fig. 12.108, the grid lines are orthogonal on all blade surfaces except the small regions at LE and TE. The mesh size is $195(\xi)\times180(\eta)$ for all subdomains. For clarity, the mesh is plotted every 4 lines in the un-zoomed plots. The blade surface has 100 points in streamwise direction. The boundary layer has 40 points in pitchwise direction. Because of the high gradient of the flow variables in near wall region, the mesh is clustered near the wall surfaces. On the blade surfaces, the grid points are also clustered toward the LE and the TE in streamwise direction.

8.7.4 Simulation in two passage cascade

The two passage cascade simulation uses the meshes of two inner neighboring passages (P2 and P3) in the compressor cascade. As shown in Fig. 12.109, The blade between the two passages is called BC (blade at center) and the two blade surfaces on the two outside periodic boundaries are treated as blade BP (blade at periodic boundary) .

The steady state pressure coefficient distributions along the blade surfaces are plotted in Fig. 12.110. The pressure coefficient predicted agrees well with the measurement. The result on BC agrees very well with that of BP, which shows good periodicity is achieved on the pitchwise direction.

Fig. 12.111 shows the pressure variation history on two points on the suction surface (US) and the pressure surface (LS) respectively. The pressure on the suction surface is located at $x/C = 0.15$ and the pressure on the pressure surface is located at $x/C = 0.1$. The temporal periodicity is achieved very soon after the start of the vibration simulation. Because of the excellent temporal periodicity, the unsteady data extracted from a single blade motion cycle is enough for the unsteady Fourier analysis. The IBPA of 180° is clearly shown by comparing the pressure maximums and minimums on BC and BP.

The unsteady pressure coefficients are plotted in Fig. 12.112 and Fig. 12.113 for suction surface (US) and the pressure surface (LS) respectively. The unsteady pressure coefficient C_p is expressed in terms of the real part or in phase part and the imaginary part or out of phase part. On the suction surface, as shown in Fig. 12.112, the CFD results compare fairly well with experiment data after 30% chord. The real part of the coefficient is predicted lower than experiment data on leading edge, but the trend agrees very well with the experiment. The imaginary part is over predicted in the leading edge region. On the pressure surface, as shown in Fig. 12.113, the real part of the unsteady pressure coefficient agrees well with the experiment data. The imaginary part is under predicted compared with the measurement on the front

part of the blade. This means that the CFD does not accurately capture the phase angle difference between the pressure response and the blade motion. A local flutter stability analysis based on the aerodynamic work per cycle suggested by Buffum[?] is presented in Fig. 12.114 by plotting $\left(0.5 - \frac{x}{c}\right) Im\left(C_{p,\text{upper}} - C_{p,\text{lower}}\right)_{1\text{st}}$. The current numerical simulation predicts a larger local stable region on the front part of the blade. On the aft part, the experiment data indicates a shallow stable region. The CFD predicts the trend very well. The aft part stable region is predicted more shallow than the experiment.

8.7.5 Simulation in full scale cascade

The full scale steady and unsteady simulation use the same inlet flow angle as that of the 2-passage case. In the steady state calculation, all blade are parallel to each other at their mean positions. As shown in Fig. 12.107, the end wall is made up of 3 sections, which have different angles relative to the x axis: $\alpha_1 = 61°$, $\alpha_2 = 60°$ and $\alpha_3 = 64°$. The middle section is parallel to the blade at its mean position. The front and aft sections follow the inlet and outlet averaged flow directions obtained in the 2-passage steady state computation.

The steady state Mach number contours for the full scale cascade is shown in Fig. 12.115. The flow pattern is highly influenced by the end wall especially for the near end wall passages, P1 and P10. The influence is reduced rapidly from the boundary passages to the inner passages. Good periodicity in flow pattern is achieved among the inner passages (P3 through P8). Three center blades, B4, B5 and B6 are chosen to study the steady and unsteady periodicity in the rest of the paper. Even though the periodicity looks good in the Mach contour plot, the static pressure distribution still shows the influence of the end walls on different blades.

Fig. 12.116 shows the pressure coefficient chordwise distribution on the 3 center blades. The experiment measurement and the 2-passage calculation results are also plotted for comparison. The surface pressure increases gradually from B4 to B6 on both the pressure surface and the suction surface. The pressure distribution on blade B6 is closest to the 2-passage periodic results on most part of the surfaces. The experiment measurement also shows the pressure variation on different blades[?], but its variation trend is opposite to the current numerical results. A possible reason for this difference is that the inlet and outlet end wall angles used in the experiment may differ from the values used in the current simulation. The experimental angles are not available. Such a pitchwise flow pattern difference is also expected in the following unsteady calculations.

The full scale unsteady simulation is first carried out for a reduced frequency k_c = 0.8 to study the end wall influence on the periodicity of the blade unsteady characteristics. Figs. 12.117 and 12.118 are the unsteady pressure coefficient chordwise distribution on the 3 center blades compared with the 2-passage cascade and the ex-

periment results. On the upper surface, as shown in Fig. 12.117, the 3 blades have very similar unsteady coefficients on most of the chordwise distance. The results of blade B6 are closest to those of the 2-passage calculation. The difference between the full scale results and the 2-passage results mainly locate at the front and center part of the blade. The full scale results agree with the experiment better in the center part. On the lower surface, as shown in Fig. 12.118, the full scale results of the 3 blades are similar. The 2-passage results are closer to the experiment data in the real part.

As shown in Fig. 12.119, the full scale calculations predict higher stability on the front part of the blade compared with the 2-passage results. The full scale results are closer to the experiment measurement on the aft part of the blade. In the chordwise region of $x/C = 0.5$ to x/C=0.7, the measured stability is better predicted in the full scale results. The 2-passage results shows instability in the same region. The end wall influence on the flow pattern periodicity is clearly shown in the unsteady aerodynamic moment oscillation plots within a whole blade motion cycle in Fig. 12.120. The moment is plotted versus the normalized deflection angle, $\alpha' = (\alpha - \alpha_0)/\hat{\alpha}$. Because of the end wall influence, the moment oscillations on the 3 center blades are different. They are also different from the 2-passage calculation results. The anti-clockwise direction of all the unsteady moment curves indicates negative work acted by the fluid on the blade. The blade motion is therefore damped down by the fluid flow. The blade motion is stable, which corresponds to a positive damping coefficient Ξ. The area enclosed by the moment curve indicates the magnitude of the work exchanged between the fluid and the blade, which is also proportional to the magnitude of the damping coefficient.

The damping coefficients on all the 9 blades in the full scale calculation versus the blade number are shown in Fig. 12.121. The damping coefficient varies among the blades. The damping coefficients for blade B4, B5 and B6 are 0.67, 0.65 and 0.68 respectively. Blade B1 has the lowest stability (Ξ =0.45) and blade B9 has the highest stability ($\Xi = 1.4$). The damping coefficient distribution is more uniform on the center blades (B3 through B7), even though small variation exists. The blade stability in the full scale cascade depends on the location of the blade. The damping coefficient obtained in the 2-passage periodic computation is 0.55.

Fig. 12.122 plots a series of Mach number contours around blade B5 and B6. A separation bubble is generated and grows periodically on the leading edge of the suction surface. At t =0, the two blades are initially located at their mean positions and are parallel to each other. Blade B5 then rotates in the counter-clockwise direction with a negative deflection angle (nose down). At the same time, blade B6 is rotating in the clockwise direction with a positive deflection angle (nose up). At t=0.2T, blade B5 is close to its minimum deflection position. The separation bubble at its LE is pushed downstream and shrinks in size. At t=0.4T, blade B5 is rotating back from its minimum deflection location toward its mean position, the separation

bubble disappears from the suction surface. At $t = 0.8$T, a new separation bubble is generated when blade B5 passes its maximum deflection position and rotates back toward its mean position. The bubble obtains its maximum size when the blade is close to its mean position. Similar phenomenon is observed on the neighboring blade B6, but with a phase difference of 180°.

More extensive unsteady simulations are carried out for reduced frequencies $k_c = 0.4$ and $k_c = 1.2$. Figs. 12.123 and 12.124 show the unsteady pressure coefficient chordwise distribution of $k_c = 1.2$. Similar to the results of $k_c = 0.8$, the predicted unsteady complex pressure coefficients are close to each other on the 3 center blades, even though some small difference exists. As shown in Fig. 12.123, on the upper surface, the imaginary parts of CFD results agree very well with the experiment results except that it is over-predicted in the region of x/C=0.15 to x/C=0.40. The real part is also predicted quite well on the middle and aft part of the blade. On the lower surface, as shown in Fig. 12.124, the predicted real parts compare very well with experiment. The Imaginary part is under-predicted from LE to $x/C = 0.7$.

The local stability analysis for $k_c = 1.2$ is plotted in Fig. 12.125. The correct trend is predicted compared with the experiment measurement, even though the magnitude does not agree very well. The stability is over-predicted in LE region. The unstable region predicted on the front part of the blade is smaller than the experiment results. The stability is predicted on the aft part, but the magnitude is smaller than the experiment data. The damping coefficients for all the blades are plotted in Fig. 12.126. The damping coefficients for blade B4, B5 and B6 are 0.81, 0.78 and 0.84 respectively. The stability increases with the frequency. Similar to the results of $k_c = 0.8$, the most stable blade is blade B9 (Ξ=1.5) and the least stable blade is blade B1 (Ξ=0.6). The damping coefficient is more uniformly distributed on the central blades. The variation of the damping coefficient on the center blades increases with the increasing frequency.

Because of the lack of experiment data, the unsteady pressure coefficient of k_c=0.4 is not presented for comparison. However, the local stability is analyzed and compared with the experiment data in Fig. 12.127. Similar to the results of $k_c = 0.8$ and $k_c = 1.2$, the trend is predicted well, but the magnitude differs from the experiment. As expected, the damping coefficient distribution is more uniform on center blades (Fig. 12.128). The variation of their magnitudes decreases with the decreasing vibration frequency compared with the high frequency cases of $k_c = 0.8$ and $k_c = 1.2$. The damping coefficients on blade B4, B5 and B6 are 0.448, 0.446 and 0.434 respectively. The most stable blade is B9 with $\Xi = 1.02$ and the least stable blade is B1 with $\Xi = 0.28$.

The unsteady aerodynamic moment oscillations on blade B5 under the 3 frequencies under investigation are plotted together and compared in Fig. 12.129. The damping coefficient increase with the increasing frequency is indicated by the increased area enclosed by the unsteady moment oscillation curve. The local stability analysis

is summarized for all the 3 frequencies in Fig. 12.130. The computation results indicate higher stability near the leading edge for higher frequency vibration, which is consistent with the experiment measurement. Even though the destabilization region on the front part of the blade and the stability magnitude on the aft part of the blade predicted by the numerical computation are smaller than those in the experiment, the trend is predicted well. Both the destabilization and stabilization increase with the increasing frequency.

8.8 3D AGARD Wing Flutter Prediction

The result of steady state transonic ONERA M6 wing is calculated first in order to validate CFD solver. Then, the flutter boundary of an AGARD wing 445.6 is calculated.

8.8.1 Steady State Transonic ONERA M6 wing

As a validation of the three dimensional solver for a transonic wing, the steady state solution of the transonic ONERA M6 wing is calculated. The freestream conditions for this study are listed in Table 8.8 below.

Table 8.8: Free-stream condition for ONERA M6 wing

Mach number	0.8395
Static Pressure (psia)	12.2913
Temperature (R)	447.0
Angle-of-Attack (deg)	0.0
Reynolds Number	19.7×10^6

This case is calculated using an O-type grid with the dimension of 144 (around wing) $\times60$ (normal to the wing) $\times40$ (spanwise). The far field boundary is located 15 chords away from the chord center of the wing. The surface mesh of the wing is depicted in Figure 12.133.

The Zha E-CUSP2 scheme is used to evaluate the inviscid fluxes with the 3rd order MUSCL type differencing [85]. The turbulent Reynolds stress and heat flux are calculated by the Baldwin-Lomax algebraic model[48].

The computed surface pressure distributions at various cross sections are shown in Figure 12.134, together with the experimental data given by Schmitt et al. [86]. The location of $z/b = 0.2$ is near the root, and $z/b = 0.99$ is at wing tip.

Overall, very good agreement is obtained between the computation and experiment for each cross-section.

8.8.2 Validation of Structural Solver

To validate the structural model used in the present study, the dynamic responses of a flexible plate wing shown in Figure 12.135 is calculated and compared with the results by using the finite element solver ANSYS. The purpose of the study is to find out how many mode shapes are required for accurate representation of the structural motion under dynamic force.

The plate wing has the same outline as the AGARD wing 445.6, and its first mode natural vibration frequency is nearly the same as the corresponding one of the AGARD wing 445.6. The thickness of the plate is 0.3", the root chord is 21.96", the tip chord is 14.49", and the spanwise length is 30". The plate wing consists of 80 elements and 861 node points on each side of the wing. The plate wing is held fixed on the root.

A time-dependent force is exerted at node point 510 which is located at the mid-point of the wing tip. The three components of the force in the unit of pound are:

$$f_x = 0.5sin(2\pi f_e t), \qquad f_y = 0.3sin(2\pi f_e t), \qquad f_z = 0.8sin(2\pi f_e t) \tag{8.22}$$

where the exciting frequency f_e is equal to 10 Hz. The modal damping ratio $\zeta_j = 0.01$, the time step used is 0.0005 *second*. The dynamic responses at several locations are recorded. Figure 12.136 shows the time histories of the responses at the node point 491 which is located almost at the center of the plate wing. The numerical predictions by the present structural solver with first five mode shapes agree excellently with the results using ANSYS with first five mode shapes and the full model. The three results are virtually duplicated to each other and are indistinguishable.

8.8.3 AGARD Wing 445.6 Flutter

The AGARD 445.6 wing is selected to demonstrate the capability of the present solver for predicting the flutter boundary. This wing has a quarter-chord sweep angle of 45 degree, an aspect ratio of 1.65, a taper ratio of 0.6576, and a NACA65A004 airfoil section in the streamwise direction. The weakened wing model (Model 3) listed in [55] is chosen for this study. The geometry of the wing and its first six mode shapes as well as the experimental flutter results are also provided in the same report [55]. The wing structure is modeled by its first five natural vibration modes in the present computation.

The simulations start with the stationary rigid body wing model. After the steady state flow field around the wing is fully developed, the rigid body wing is switched to the flexible wing model. As a small imposed perturbation, the first mode displacement of the structural motion is set into sinusoidal motion for one cycle with the maximum amplitude of 0.0005 - 0.001 and the first mode frequency of the wing. Then the wing is allowed to deflect in response to the dynamic force load. Within each physical time step, the solution is usually converged within 50 iterations.

In Figures 12.137 through 12.139 the time histories of generalized displacements of the AGARD wing 445.6 at $M_\infty = 0.96$ are plotted for three different V^*. In these figures, from $V^* = 0.26$ to $V^* = 0.315$, the plots correspond to the damped, neutral, and diverging responses, respectively. When the value of V^* is smaller than the critical value on the flutter boundary, the amplitudes of all modes decrease in time corresponding to the damped response as shown in Figure 12.137. Once the value of V^* coincides with or is close to the critical value, the neutral response appears as shown in Fig. 12.138. When the value of V^* is above the neutral stability point, the amplitudes of first five modes grow very fast, a diverging response is reached as shown in Fig. 12.139.

For a given Mach number, several runs with different V^* are needed to determine the location of the flutter boundary using bisection method. When V^* is varied, the free-stream Reynolds number is changed accordingly. Strictly speaking, the free-stream Reynolds number needs to be updated and the initial steady-state flow field with actual Reynolds number should be re-generated for each run. In present simulation, the initial flow field and the Reynolds number remain unchanged when V^* is varied since the effect on final solution due to small variation in the free-stream Reynolds number is negligible when a turbulence model is used.

The comparison of computed flutter boundary and experimental data for AGARD Wing 445.6 is illustrated in Figure 12.140. Overall, the computed results are in good agreement with the experimental data. The "sonic dip" near Mach = 1.0 measured in the experiment is very well captured by the computation. The discrepancy between computed results and experimental data may be due to the inadequacy of the turbulent modeling to capture the shock/wave boundary layer interaction or may be due to the inaccurate measurement in the experiment as suspected by some researchers.

Chapter 9

Personnel

The personnel participating this research include the PI, Dr. Gecheng Zha; Co-PI, Dr. Mingta Yang; the research associate, Dr. Xiangying Chen; and a Ph.D. student, Mr. Zongjun Hu, who has partially participated in this research.

Chapter 10

Conclusions

In this research, a new high efficiency low diffusion upwind scheme is developed and is applied to moving grid systems. The fully coupled fluid-structural interaction with the new upwind scheme is successfully developed and predicts the 3d AGARD wing flutter boundary very well. The SNM model at time domain is developed and validated. The forced vibration of the NASA flutter cascade is simulated with reasonable agreement with the experiment. A set of nonlinear non-reflective boundary conditions for Navier-Stokes equations on the generalized coordinates is developed to avoid the reflective waves. The code is ready to calculate the fluid-structural interaction of the mistunned rotor bladed disk. However, since the funding is only 3 years, which is one year shorter than the 4 years time period originally proposed, the mistunned rotor simulation is not completed and will be done in future when the funding is available.

The following is the specific conclusions achieved in this research:

10.1 The New E-CUSP scheme

A new efficient upwind scheme based on the concept of convective upwind and split pressure (CUSP) is developed. The upwinding of the convective term and the pressure splitting are consistent with their characteristics directions. The numerical dissipation of the new scheme at stagnation is low and is not greater than that of the Roe scheme. The scheme hence is able to resolve accurately wall boundary layers, and are able to capture crisp shock waves and exact contact discontinuities. The performance of the new scheme is compared with the Roe scheme, AUSM$^+$ scheme, Van Leer scheme, and Van Leer-Hänel scheme.

For the 1D Sod shock tube problem using Euler explicit scheme, the new scheme has the crispest shock profile and highest allowable CFL number of 1.0. For a slowly moving contact surface, the new scheme is demonstrated to capture the exact contact surface discontinuity with the maximum allowable CFL of 1.0, which is far greater

than that of the other schemes. For a quasi-1D transonic nozzle, all the other schemes generate expansion shocks at the sonic point. The new scheme does not have the expansion shock even though it has a glitch at the sonic point, which is due to the discontinuity of the first derivative of the pressure splitting at sonic point.

For a Mach=2.0 supersonic adiabatic laminar flat plate boundary layer, the new scheme is able to accurately resolve the boundary layer velocity and temperature profiles using the first order differencing. The solution is as accurate as that of the Roe scheme and the AUSM$^+$ scheme and hence demonstrates the low diffusion of the new scheme.

For a transonic converging-diverging nozzle, oblique shock waves and reflections are crisply captured even though the shock waves do not align with the mesh lines. The predicted wall surface isentropic Mach number distribution agrees well with the experiment. For a transonic inlet-diffuser with shock/turbulent boundary layer interaction, the new scheme and the Roe scheme predict the surface pressure distributions agreeing well with the experiment for the case of a weak shock. For the strong shock case, both the new scheme and the Roe scheme over predict the strength of the shock wave. However, the pressure distribution predicted by the new scheme is closer to the experiment. The AUSM$^+$ solution has large pressure oscillations.

In the applications of the original Zha-Hu E-CUSP scheme, it is found that there is temperature oscillations near wall boundaries. The scheme is modified by replaceing the pressure term with the total enthalpy in the smoothing factor of the energy equation. The temperature oscillations are removed in the modified scheme, which is named Zha E-CUSP2 scheme.

10.2 Non-Reflective Boundary Conditions

The non-reflective boundary conditions of Poinsot and Lele[33] for 3D Navier-Stokes equations are extended to the generalized coordinates in this paper. The characteristic form Navier-Stokes equations in conservative variables are given. The NRBC is applied numerically in an implicit time marching method. The governing equations for inner domain and NRBC are solved simultaneously in a fully couple manner.

For the unsteady subsonic vortex propagating flow, the fixed pressure outflow boundary conditions imposing the exit pressure generates serious wave reflection and the flow field is distorted, whereas, the NRBC developed in this paper generates clean results with no wave reflection and solution distortion.

For the transonic inlet-diffuser, the NRBC is not necessary for steady state solutions since the reflective waves are diffused when the solutions are converged. However, for unsteady flows, the NRBC is essential. The fixed pressure outflow boundary conditions generate strong reflective waves due to the shock/boundary layer inter-

action, which makes the shock oscillating motion far greater than the experimental data. When the NRBC is applied, the shock oscillation is dramatically reduced and the computed time averaged pressure distributions and frequency spectrum agree much better with the experiment than FPBC.

The NRBC is essential for unsteady fluid-structural interactions, in particular for the internal flows such as the mistunned rotors.

10.3 2D Flutter Prediction

The efficient high resolution E-CUSP upwind schemes developed in this research have been successfully extended and applied to calculate flow-induced vibration with a moving grid based on fully coupled fluid-structural interaction.

For an elastically mounted cylinder, various cases with different structural parameters have been calculated. The predicted displacement agrees very well with the experiment and the numerical results of other researchers.

For the forced pitching NACA 64A010 airfoil, the computed lift oscillation agrees accurately with the experiment. The computed moment oscillation has large deviation from the experiment, but the results have a similar order of accuracy as other researchers have achieved. The discrepancy may be due to the inaccurate prediction of the surface shear stress caused by the inadequacy of the turbulence modeling and experimental uncertainties.

The same airfoil has been calculated as an elastically mounted airfoil with free vibration in plunging and pitching directions. The computations have been carried out using different values of velocity index V^* which are below, close, and beyond the critical point on the flutter boundary when Mach number is fixed. The corresponding responses of the airfoil flows are well simulated. The predicted value of V^* at the bottom of the transonic dip is consistent with the numerical results of other researchers [5, 73, 70].

10.4 SNM model of Transient Response

The transient response (time domain) structural vibration model for mistunned rotor bladed disk based on the efficient Subsets of Nominal Modes (SNM) model is developed. The vibration response results predicted by the SNM model for a full annulus bladed disk with blade frequency variation agree well with the results predicted by the finite element model. The simplified model was designed such that transient response computations can be performed in ANSYS with tractable computational cost. The comparison of the results showed that SNM model can capture both low frequency

and high frequency responses. In the case of low frequency excitation, only one family of blade modes is needed in SNM. In the case of high frequency excitation, multiple families of blade modes are needed in SNM. The computational efficiency was improved by at least 30 times over ANSYS direct simulations for the cases examined. The improvement is expected to be much greater when high fidelity ANSYS models are needed.

10.5 Separated Flows in NASA 3D Flutter Cascade

1. The high incidence cascade separation flow shows a sinusoidal pattern on the oscillation of the surface pressure and the separation bubble size.

2. The leading edge vortex shedding is the mechanism behind the unsteady characteristics of the subsonic high incidence separation flow. New vortexes are continuously generated at the suction surface leading edge. The new vortex grows and pushes the old vortexes downstream. The interaction between the vortexes results in the periodical oscillation of the separation bubble size and the surface pressure. The vortex generation, pressure variation and separation length oscillation have the same frequency characteristics with a phase difference.

3. The characteristics of the separation flow is determined by the inlet Mach number. When the inlet flow goes from lower subsonic to higher subsonic, the size and the oscillation intensity of the separation bubble are enhanced. The flowfield oscillation peak frequency increases. When the inflow goes further to supersonic, the flow is attached on the leading edge. A small size separation bubble due to the interaction of the shock wave and the turbulent boundary layer is located right after the shock wave.

10.6 Forced Vibration of the NASA Flutter Cascade

The fully nonlinear time dependent Navier-Stokes equations are solved with the parallel computation technique to simulate the unsteady flow field in a full scale compressor cascade with forced blade vibration. The calculation in this paper is conducted with a low incidence of 0° and a subsonic inflow $M=$ 0.5. The blade motion amplitude is 1.2°and the inter blade phase angle is 180°. The full scale computation is carried out for 3 reduced frequencies, 0.4, 0.8 and 1.2. The blade stability under different

vibration frequency is analyzed. The end wall influence on the steady and unsteady flow characteristics is studied by comparing the full scale results with the 2-passage periodic cascade results at k_c =0.8. The conclusions are the following:

1. The flow pattern in the full scale cascade shows that the flowfield is affected by the existence of the end walls. The steady state blade surface pressure varies with the the blade position in the cascade. The periodicity of the flow pattern is improved by adjusting the end wall configuration. The end wall influence attenuates rapidly from boundary passages to center passages. Good periodicity is achieved in the inner passages. The full scale computation gives better results of the unsteady pressure coefficient, local stability and aerodynamic moment among the center blades.

2. All blades in the full scale cascade are stable, which is indicated by a positive damping coefficient. The damping coefficient is more uniformly distributed on center blades. The most stable and the least stable blades are the two boundary blades. The damping coefficient and its variation across the center blades increase with the increasing vibration frequency.

3. The unsteady pressure coefficients are predicted well compared with the experiment measurement. The local stability trend is correctly predicted in the numerical computation. The blade local stability is over-predicted on LE and under-predicted on the aft part. The destabilization region located at the front part of the blade is predicted smaller compared with the experiment. The predicted stabilization and destabilization increase with the increasing frequency, so do the damping coefficients.

10.7 3D AGARD Wing Flutter Prediction

A numerical methodology with fully coupled fluid-structural interaction for predicating 3-D transonic wing flutter has been developed. A dual-time step implicit unfactored Gauss-Seidel iteration with Roe scheme are employed in the flow solver. A modal approach structure solver is used to simulate the wing response. An efficient mesh deformation strategy based on an algebraic method is developed and is shown to be accurate and robust. The flow and structure solvers are fully coupled vis successive iterations within each physical time step.

The accuracy of the modal approach structure solver has been verified by using the finite element solver ANSYS. The results indicate that the first five modes are sufficient to accurately model the wing structure in the present study.

The computed flutter boundary of AGARD wing 445.6 for free stream Mach numbers ranging from 0.499 to 1.141 is presented and compared well with the experimental

data except for $M_\infty = 1.171$, where the flutter boundary is over-predicted. The sonic dip is very well captured.

10.8 Future Work

With the foundation laid in the research, the next step is to apply the fully coupled fluid-structural interaction solver to mistunned rotor bladed disk.

Chapter 11

Publications

In this research project, we have published five journal publications, submitted two papers for journal publications, and published 12 conference papers.

Journal Publications:

1) Chen, X. and Zha, G.-C., "Implicit Application of Non-Reflective Boundary Conditions for Navier-Stokes Equations in Generalized Coordinates ", International Journal for Numerical Methods in Fluids, Vol. 50, No. 7, pp767-793, 2006

2) Chen, X. and Zha, G.-C.,"Fully Coupled Fluid-Structural Interactions Using an Efficient High Solution Upwind Scheme", Journal of Fluid and Structure, Vol. 20, No. 8, Nov. 2005, pp1105-1125

3) Zha, G.-C., "A Low Diffusion Efficient Upwind Scheme " , AIAA Journal, Vol.43, No.5, pp 1137-1140, 2005

4) Hu, Z. and Zha, G.-C.,"Calculations of 3D Compressible Using an Efficient Low Diffusion Upwind Scheme",International Journal for Numerical Methods in Fluids, Vol. 47, pp253-269, Nov. 2004

5) Zha, G.-C. and Hu, Z.,"Calculation of Transonic Internal Flows Using an Efficient High Resolution Upwind Scheme" , AIAA Journal, Jan. 2004

Submitted for Journal Publication:

1) Chen, X., Zha, G.-C. and Yang, M.-T. "3D Simulation of a Transonic Wing Flutter using an Efficient High Resolution Upwind Scheme, to AIAA J. of Aircraft ", Submitted for publication in AIAA Journal of Aircraft

2) Chen, X.-Y. and Zha, G.-C. and Yang, M.-T. "Numerical Simulation of 3-D Wing Flutter with Fully Coupled Fluid-Structural Interaction " Submitted for publication in Journal of Computer and Fluids

Conference Publications:

1) Chen, X., Zha, G.-C. and Yang, M.-T. "3D Simulation of a Transonic Wing Flutter using an Efficient High Resolution Upwind Scheme, to AIAA J. of Aircraft ", AIAA Paper 2006-3216, 36th AIAA Fluid Dynamics Conference and Exhibit, June 5-8, 2006, San Franscisco, CA

2) Hu, Z. and Zha, G.-C. "Parallel Computation of Forced Vibration for A Compressor Cascade ", AIAA Paper 2006-0628, AIAA the 44th Aerospace Sciences Meeting and Exhibit Conference, Jan. 8-12, 2006, Reno, NV

3) Chen, X.-Y. and Zha, G.-C. and Yang, M.-T. "Numerical Simulation of 3-D Wing Flutter with Fully Coupled Fluid-Structural Interaction ", AIAA Paper 2006-0697, AIAA the 44th Aerospace Sciences Meeting and Exhibit Conference, Jan. 8-12, 2006, Reno, NV

4) Chen, X. and Zha, G.-C., "Implicit Application of Non-Reflective Boundary Conditions for Navier-Stokes Equations in Generalized Coordinates ", AIAA Paper 2005-0091, AIAA the 43rd Aerospace Sciences Meeting and Exhibit Conference, Jan. 10-13, 2005, Reno, NV

5) Hu, Z. and Zha, G.-C.,"Simulation of 3D Flows of Propulsion Systems Using an Efficient Low Diffusion E-CUSP Upwind Scheme",AIAA Paper 2004-4082, 40th AIAA/ASME/SAE/ASEE Joint Propulsion Conference and Exhibit, July 11–14, Fort Lauderdale, Florida

6) Chen, X. and Zha, G.-C.,"Fully Coupled Fluid-Structural Interactions Using an Efficient High Solution Upwind Scheme" , AIAA Paper 2004-2331, 34th AIAA Fluid Dynamics Conference and Exhibit, 28 Jun - 1 Jul 2004, Portland, Oregon

7) Chen, X. Zha, G.-C. and Hu, Z.,"Numerical Simulation of Flow Induced Vibration Based on Fully Coupled Fluid-Structural Interactions" , AIAA Paper 2004-2240, 34th AIAA Fluid Dynamics Conference and Exhibit, 28 Jun - 1 Jul 2004, Portland, Oregon

8) Zha, G.-C., "A Low Diffusion E-CUSP Upwind Scheme for Transonic Flows " , AIAA Paper 2004-2707, 34th AIAA Fluid Dynamics Conference and Exhibit, 28 Jun - 1 Jul 2004, Portland, Oregon

9) Hu, Z. and Zha, G.-C.,"Numerical Study of a Casacde Unsteady Separated Flow" , ASME Paper GT2004-53195, ASME TURBO EXPO 2004, June 14-17, 2004, Vienna, Austria

10) Chen, X., Zha, G.-C., Hu, Z. and Yang, M.-T.,"Flutter Prediction Based on Fully Coupled Fluid-Structural Interactions" , paper, 9th National Turbine Engine High Cycle Fatigue Conference, 16-19 March 2004

11) Zha, G.-C. and Hu, Z., "Calculation of Transonic Internal Flows Using an Efficient High Resolution Upwind Scheme" , AIAA-2004-1097, AIAA the 42st Aerospace Sciences Meeting and Exhibit Conference, Jan. 5-8, 2004, Reno, NV

12) Zha, G.-C. and Hu, Z.,"Numerical Study on Flow Separation of A Transonic

Cascade" , AIAA-2004-0199, AIAA the 42st Aerospace Sciences Meeting and Exhibit Conference, Jan. 5-8, 2004, Reno, NV

Chapter 12

Acknowledgment

The funding support from AFOSR for this research with grant F49620-03-1-0253 is acknowledged. The authors would like to thank the program manager Dr. Fariba Fahroo at AFOSR for her support of this research. The authors would also like to thank the management of Pratt & Whitney to support this research collaboration with the cost sharing.

Bibliography

[1] G.-C. Zha and Z.-J. Hu, "Calculation of Transonic Internal Flows Using an Efficient High Resolution Upwind Scheme," *AIAA Journal*, vol. 42, No. 2, pp. 205–214, 2004.

[2] X. Chen and G.-C. Zha, "Fully Coupled Fluid-Structural Interactions Using an Efficient High Solution Upwind Scheme," *Journal of Fluid and Structure*, vol. 20, pp. 1105–1125, 2005.

[3] G.-C. Zha, "Low Diffusion Efficient Upwind Scheme ," *AIAA Journal*, vol. 43, 2005.

[4] X.-Y. Chen, G.-C. Zha, and M.-T. Yang, "Numerical Simulation of 3-D Wing Flutter with Fully Coupled Fluid-Structure Interaction Approach." AIAA Paper 2006-0697, 44th AIAA Aerospace Sciences Meeting and Exhibit, Reno, NA,, Revised for publication in the Journal of Computer & Fluids, July 2006.

[5] X.-Y. Chen, G.-C. Zha, and Z.-J. Hu, "Numerical Simulation of Flow Induced Vibration Based on Fully Coupled-Structural Interactions." AIAA Paper 2004-2240, AIAA 34th AIAA Fluid Dynamics Conference,, Jaun 28 - July 1, 2004.

[6] X. Chen and G.-C. Zha, "Implicit Application of Non-Reflective Boundary Conditions for Navier-Stokes Equations in Generalized Coordinates," *International Journal for Numerical Methods in Fluids*, vol. 50, 2006.

[7] R. B. Melville, "Next Generation Computational Tools for Next Generation Challenges." AFOSR/AFRL Workshop on Nonlinear Aspects of Aeroelasticity, March 6-7, 2003.

[8] P. D. Silkowski, C. M. Rhie, G. S. Copeland, J. A. Eley, and J. M. Bleeg, " CFD Investigation of Aeromechanics ." ASME Paper 2001-GT-0267, Proceedings of ASME TURBO EXPO 2001, New Orleans, Louisiana., June 4-7, 2001.

[9] G. Hilbert and A. Blair, "Accuracy of Airfoil Resonance Stress Predictions." Proceedings of the 6th National Turbine Engine High Cycle Fatigue (HCF) Conference, Jacksonville, Florida, 5-8 March 2001.

[10] O. Bendiksen and K. Kousen, "Transonic Flutter Analysis Using the Euler Equations." AIAA Paper 87-0911, 1987.

[11] J. J. Alonso and A. Jameson, "Fully-Implicit Time-Marching Aeroelastic Solutions." AIAA Paper 94-0056, 1994.

[12] J. J. Alonso, L. Martineli, and A. Jameson, "Multifrid Unsteady Navier-Stokes Calculations with Aeroelastic Applications." AIAA Paper 95-0048, 1995.

[13] F. Liu, J. Cai, Y. Zhu, A. Wong, and H. Tsai, "Calculation of Wing Flutter by a Coupled CFD-CSD Method." AIAA-2000-0907, 2000.

[14] R. B. Melville and S. A. Morton, "Fully Implicit Aeroelasticity on Oveerset Grid Systems ." AIAA Paper-98-0521, 1998.

[15] A. Sayma, J. Vahdati, M. Green, and M. Imregun, "Whole-assembly Flutter Analysis of a Low Pressure Turbine Blade," *The Aeronautical Journal*, vol. 102, pp. 459–463, 1998.

[16] A. Sayma, M. Vahdati, and M. Imregun, "Turbine Forced Response Prediction Using an Integrated Nonlinear Analysis ," *Journal of Multi-body Dynamics*, vol. 214(K1), pp. 45–60, 2000.

[17] A. Sayma, M. Vahdati, and M. Imregun, "Multi-stage whole-annulus forced response predictions using an integrated non-linear analysis technique - Part I: Numerical model," *Journal of Fluids & Structures*, vol. 14(1), pp. 87–101, 2000.

[18] A. Sayma, M. Vahdati, and M. Imregun, "Multi-stage whole-annulus forced response predictions using an integrated non-linear analysis technique - Part II: Study of a HP turbine," *Journal of Fluids & Structures*, vol. 14(1), pp. 103–125, 2000.

[19] H. Doi and J. J. Alonso, "Fluid/Structure Coupled Aeroelastic Computations for Transonic Flwos in Turbomachinery." GT-2002-30313, June 3-6, 2002.

[20] A. Jameson, "Analysis and Design of Numerical Schemes for Gas Dynamics I: Artificial Diffusion, Upwind Biasing, Limiters and Their Effect on Accuracy and Multigrid Convergence in Transonic and Hypersonic Flow." AIAA Paper 93-3359, July, 1993.

[21] A. Jameson, "Analysis and Design of Numerical Schemes for Gas Dynamics I: Artificial Diffusion, Upwind Biasing, Limiters and Their Effect on Accuracy and Multigrid Convergence in Transonic and Hypersonic Flow," *Journal of Computational Fluid Dynamics*, vol. 4, pp. 171–218, 1995.

[22] A. Jameson, "Analysis and Design of Numerical Schemes for Gas Dynamics II: Artificial Diffusion and Discrete Shock Structure," *Journal of Computational Fluid Dynamics*, vol. 5, pp. 1–38, 1995.

[23] M.-S. Liou, "A Sequel to AUSM: AUSM$^+$," *Journal of Computational Physics*, vol. 129, pp. 364–382, 1996.

[24] D. Hänel, R. Schwane, and G. Seider, "On the Accuracy of Upwind Schemes for the Solution of the Navier-Stokes Eqautions." AIAA paper 87-1105 CP, 1987.

[25] J. R. Edwards, "A Low-Diffusion Flux-Splitting Scheme for Navier-Stokes Calculations." AIAA Paper 95-1703-CP, June, 1995.

[26] J. R. Edwards, "A Low-Diffusion Flux-Splitting Scheme for Navier-Stokes Calculations," *Computer & Fluids*, vol. 6, pp. 635–659, 1997.

[27] X.-Y. Chen and G.-C. Zha, "Fully Coupled Fluid-Structural Interactions Using an Efficient High Resolution Upwind Scheme," *Journal of Fluids and Structures*, vol. 20, pp. 1105–1125, 2005.

[28] X.-Y. Chen and G.-C. Zha, "Calculation of 3D Transonic Wing Flutter Using an Efficient High Resolution Upwind Scheme." AIAA-2006-3216, 36th AIAA Fluid Dynamics Conference and Exhibit, San Francisco, CA, 5-8 June, 2006.

[29] E. Lee-Rausch and J. Batina, "Calculation of AGARD Wing 445.6 Flutter Using Navier-Stokes Aerodynamics." AIAA Paper 93-3476, 1993.

[30] S. A. Morton, R. B. Melville, and M. R. Visbal, "Accuracy and Coupling Issues of Aeroelastic Navier-Stokes Solutions on Deforming Meshes." AIAA Paper-97-1085, 1997.

[31] R. B. Melville, S. A. Morton, and D. P. Rizzetta, "Implementation of a Fully-Implicit, Aeroelastic Navier-Stokes Solver." AIAA Paper-97-2039, 1997.

[32] R. Gordnier and M. R.B., "Transonic Flutter Simulations Using an Implicit Aeroelastic Solver," *Journal of Aircraft*, vol. 37, pp. 872–879, September-October 2000.

[33] T. Poinsot and S. Lele, " Boundary Conditions for Direct Simulations of Compressible Viscous Flows," *Journal of Computational Physics*, vol. 101, pp. 104–129, 1992.

[34] T. Nishizawa and H. Takata, " Numerical Study on Rotating Stall in Finite Pitch Cascades." ASME Paper., Proceedings of the International Gas Turbine and Aeroengine Congress and Exposition, The Hague, Netherlands, June 1994.

[35] L. He, " Computational Study of Rotating Stall Inception in Axial Compressors," *Journal of Propulsion and Power*, vol. 13, pp. 31–38, 1997.

[36] M. Giles, "Nonreflecting Boundary Conditions for Euler Calculations ," *AIAA Journal*, vol. 28, No. 12, pp. 2050–2058, 1990.

[37] J. W. Kim and D. J. Lee, "Generalized Characteristic Boundary Conditions for Computational Acoustics," *AIAA Journal*, vol. 38, pp. 2040–2049, 2000.

[38] G. B. Whitham, *Linear and Nonlinear Waves.* Wiley, New York, 1974.

[39] K. Thompson, "Time Dependent Boundary Conditions for Hyperbolic Systems," *Journal of Computational Physics*, vol. 68, 1987.

[40] C. H. Bruneau and E. Creuse, "Towards a Transparent Boundary Conditions for Compressible Navier-Stokes Equations," *International Journal for Numerical Methods in Fluids*, vol. 36, pp. 807–840, 2001.

[41] R. Prosser and J. Schluter, "Toward Improved Boundary Conditions for the DNS and LES of Turlents Subsonic Flows," tech. rep., Stanford University/NASA Ames, Center for Turbulence Research, Proceeding of the CTR Summer Program, 2004.

[42] V. Moureau, G. Lartigue, Y. Sommerer, and C. Angelberger, "Numerical Methods for Unsteady Compressible Mult-Component Reacting Flows on Fixed and Moving Grids," *Journal of Computational Physics*, vol. 202, pp. 710–736, 2005.

[43] M.-T. Yang and J. H. Griffin, " A Reduced Order Model of Mistuning Using a Subset of Nominal System Modes ," *Journal of Engineering for Gas Turbines and Power*, vol. 123, pp. 893–900, 2001.

[44] S. Srinivasan and M.-T. Yang, " Status and Plan for Aeromechanics and Structures." Internal Report, Pratt & Whitney Aircraft, April 1999.

[45] M. Kruse and C. Pierre, "Forced Response of Mistuned Bladed Disks Using Reduced-Order Modeling." AIAA 96-26801, 37th Proceedings of AIAA/ASME/ASCE/AHS/ASC Structures, Structural Dynamics and Materials Conference and Exhibit, 1996.

[46] E. Petrov, K. Sanliturk, D. Ewins, and R. Elliot, " Quantitative Prediction of the Effects of Mistuning Arrangement on Resonant Response of a Practical Turbine Bladed Disc ." Proceedings of 5th National Turbine Engine High Cycle Fatigue Conference, Chandler, Arizona, March 7-9, 2000.

[47] F. Moyroud, T. Fransson, and G. Jacquet-Richardet, "A Comparison of Two Finite Element Reduction Techniques for Mistuned Bladed Disks," *Journal of Engineering for Gas Turbines and Power*, vol. 124, pp. 942–952, 2002.

[48] B. Baldwin and H. Lomax, "Thin Layer Approximation and Algebraic Model for Separated Turbulent Flows." AIAA Paper 78-257, 1978.

[49] A. Jameson, "Time Dependent Calculations Using Multigrid with Application to Unsteady Flows past Airfoils and Wings." AIAA Paper 91-1596, 1991.

[50] P. Roe, "Approximate Riemann Solvers, Parameter Vectors, and Difference Schemes," *Journal of Computational Physics*, vol. 43, pp. 357–372, 1981.

[51] B. Van Leer, J. Thomas, P. L. Roe, and R. Newsome, "A Comparison of Numerical Flux Formulas for the Euler and Navier-Stokes Equations." AIAA paper 87-1104, 1987.

[52] G.-C. Zha, B. Carroll, C. Paxton, A. Conley, and A. Wells, "High Performance Airfoil with Co-Flow Jet Flow Control." AIAA-Paper-2005-1260,Jan. 2005, submitted for publication in AIAA Journal.

[53] P. Thomas and C. Lombard, "Geometric Conservation Law and Its Application to Flow Computations on Moving Grids," *AIAA Journal*, vol. 17, pp. 1030–1037.

[54] D. Rudy and J. Strikwerda, "A Nonreflecting Outflow Boundary Condition for Subsonic Navier-Stokes Calculations," *Journal of Computational Physics*, vol. 36, pp. 55–70, 1980.

[55] E. C. Yates Jr, "AGARD Standard Aeroelastic Configurations for Dynamic Response, I-Wing 445.6." AGARD Report No. 765, Sept. 1985.

[56] G. Sod, "A survey of several finite difference methods for systems of nonlinear hyperbolic conversation laws," *Journal of Computational Physics*, vol. 27, pp. 1–31, 1978.

[57] Y. Wada and M.-S. Liou, "An Accurate and Robust Splitting Scheme for Shock and Contact Discontinuities." AIAA Paper 94-0083, 1994.

[58] G.-C. Zha, "Numerical Tests of Upwind Scheme Performance for Entropy Condition ," *AIAA Journal*, vol. 37, pp. 1005–1007, 1999.

[59] G.-C. Zha, "Comparative Study of Upwind Scheme Performance for Entropy Condition and Discontinuities." AIAA Paper 99-CP-3348, June 28- July 1, 1999.

[60] A. Harten, P. D. Lax, and B. Van Leer, "On Upstream Differencing and Godunov-type Scheme for Hyperbolic Conservation Laws," *SIAM Review*, vol. 25, No.1, pp. 35–61, Jan. 1983.

[61] M. L. Mason and L. E. Putnam, "The Effect of Throat Contouring on Two-Dimensional Converging-Diverging Nozzles at Static Conditions ." NASA Technical Paper 1704, 1980.

[62] T. Bogar, M. Sajben, and J. Kroutil, "Characteristic Frequency and Length Scales in Transonic Diffuser Flow Oscillations." AIAA Paper 81-1291, 1981.

[63] A. Roshko, "On the Development of Turbulent Wakes From Vortex Streets." NACA Rep. 1191, 1954.

[64] S. Goldstein, "Modern Developments in Fluid Dynamics." Clarendon Press, Oxford, 1938.

[65] J. Alonso, L. Martinelli, and A. Jameson, "Multigrid Unsteady Navier-Stokes Calculations with Aeroelastic Applications." AIAA Paper 95-0048, 1995.

[66] A. Roshko, "On the development of turbulent wakes from vortex streets," Tech. Rep. NACA Technical Note 2913, NACA, March 1953.

[67] O. M. Griffin, "Vortex-induced vibrations of marine structures in uniform and sheared currents." NSF Workshopon Riser Dynamics, University of Michigan, 1992.

[68] H. Blackburn and G. Karniadakis, "Two and Three-Dimensional Vortex-Induced Vibration of a Circular Cylinder." ISOPE-93 Conference, Singapore, 1993.

[69] P. Cook, M. McDonald, and M. Firmin, "Aerofoil RAE 2822 - Pressure Distributions, and Boundary Layer and Wake Measurements." AGARD Report AR 138, 1979.

[70] B. B. Prananta, H. M. H. L., and Z. R. J., "Two-Dimensional Transonic Aeroelastic Analysis Using Thin-Layer Navier-Stokes Method," *Journal of Fluid and Structures*, vol. 12, pp. 655–676, 1998.

[71] S. S. Davis, "Naca 64 a010 (naca ames model) oscillatory pitching," Tech. Rep. AGARD Report No. 702, AGARD, August 1982.

[72] M. McMullen, A. Jameson, and J. Alonso, "Application of a Non-Linear Frequency Domain Solver to the Euler and Navier-Stokes Equations." AIAA Paper-2002-0120, 2002.

[73] J. Bohbot and D. Darracq, "Time Domain Analysis of Two D.O.F. Airfoil Flutter Using an Euler/Turbulent Navier-Stokes Implicit Solver." International Forum on Aeroelasticity and Structural Dynamics, Madrid, Spain, June 5-7, 2001.

[74] K. Isogai, "Transonic Dip Mechanism of Flutter of a Sweptback Wing: Part II," *AIAA Journal*, vol. 19, pp. 1240–1242, September 1981.

[75] J. J. Alonso and A. Jameson, "Fully-Implicit Time-Marching Aeroelastic Solutions." AIAA Paper 94-0056, 1994.

[76] K. Kousen and O. Bendiksen, "Nonlinear Aspects of the Transonic Aeroelastic Stability Problem." AIAA Paper 88-2306, 1988.

[77] T. Hsieh, T. J. Bogar, and T. J. Coakley, "Numerical Simulation and Comparison with Experiment for Self-Excited Oscillations in a Diffuser Flow," *AIAA Journal*, vol. 25, No. 7, July, 1987.

[78] J. Lepicovsky, E. McFarland, R. Chima, and J. Wood, "On Flowfield Periodicity in the NASA Transonic Flutter Cascade, Part I-Experimental Study." NASA/TM-2000-209934, ASME 2000-GT-0572, 2000.

[79] D. H. Buffum, V. R. Capece, A. J. King, and Y. M. EL-Aini, "Oscillating cascade aerodynamics at large mean incidence." NASA Technical Memorandum 107247, 1996.

[80] Z. Hu, G. Zha, and J. Lepicovsky, "Numerical study on flow separation of a transonic cascade," Jan. 2004. AIAA Paper 2004–0199.

[81] B. Grüber and V. Carstens, "The impact of viscous effects on the aerodynamic damping of vibrating transonic compressor blades—a numerical study," *Journal of Turbomachinery*, vol. 123, 2001.

[82] S. Weber and M. F. Platzer, "A Navier-Stokes analysis of the stall flutter characteristics of the Buffum cascade," *Journal of Turbomachinery*, vol. 122, 2000.

[83] J. Lepicovsky, E. R. McFarland, V. R. Capece, and J. Hayden, "Unsteady pressures in a transonic fan cascade due to a single oscillating airfoil." ASME Paper GT-2002-30312, 2002.

[84] J. Lepicovsky, V. R. Capece, and C. T. Ford, "Resonance effects in the NASA transonic flutter cascade facility." ASME Paper GT-2003-38344, 2003.

[85] B. Van Leer, "Towards the Ultimate Conservative Difference Scheme, III," *Journal of Computational Physics*, vol. 23, pp. 263–75, 1977.

[86] V. Schmitt and F. Charpin, "Pressure Distributions on the ONERA-M6-Wing at Transonic Mach Numbers," Tech. Rep. AGARD AR 138, AGARD, May 1979.

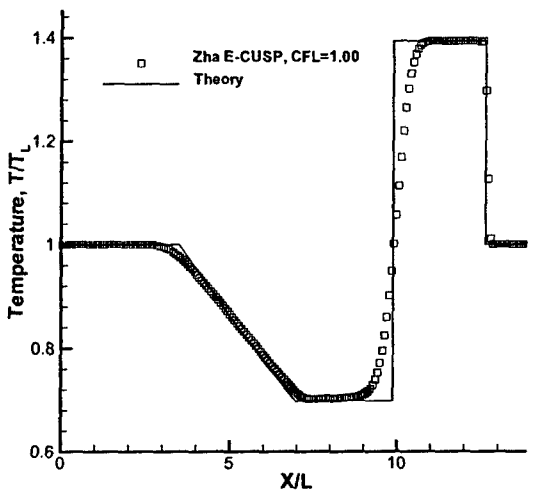

Figure 12.1: Temperature distribution of the Sod 1D shock tube computed by Zha E-CUSP scheme

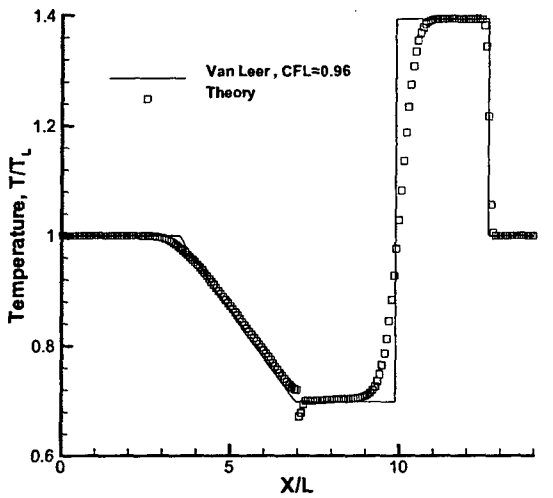

Figure 12.3: Temperature distribution of the Sod 1D shock tube computed by Van Leer scheme

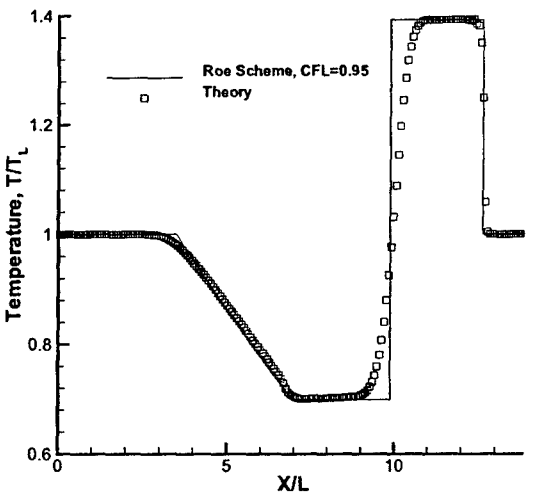

Figure 12.2: Temperature distribution of the Sod 1D shock tube computed by Roe scheme

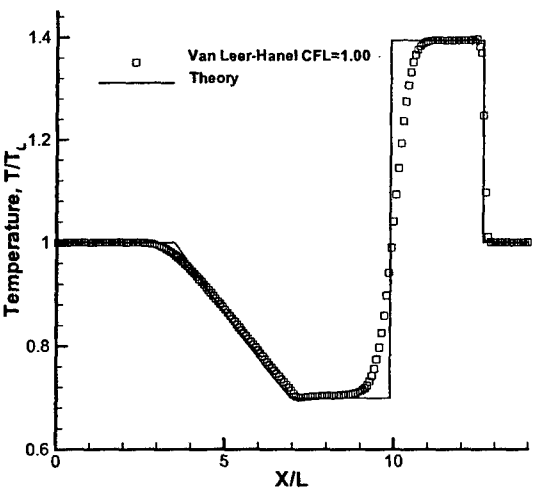

Figure 12.4: Temperature distribution of the Sod 1D shock tube computed by Van Leer-Hänel scheme

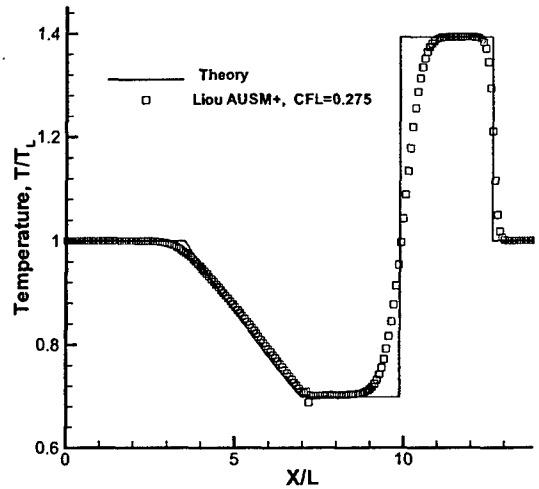

Figure 12.5: Temperature distribution of the Sod 1D shock tube computed by AUSM$^+$ scheme

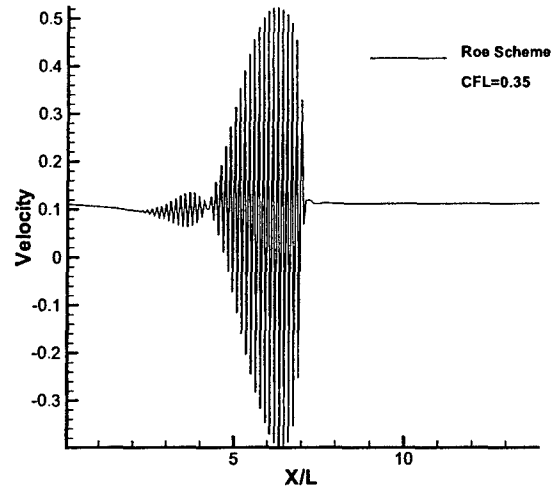

Figure 12.7: Computed density profile of a slowly moving contact surface using the Roe scheme

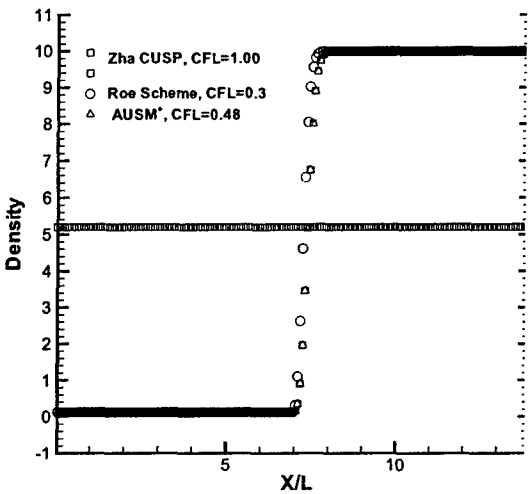

Figure 12.6: Computed density and velocity profiles of a slowly moving contact surface

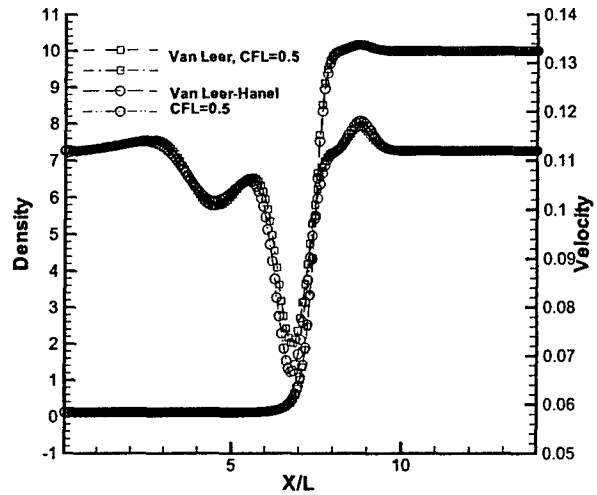

Figure 12.8: Computed density and velocity profiles of a slowly moving contact surface

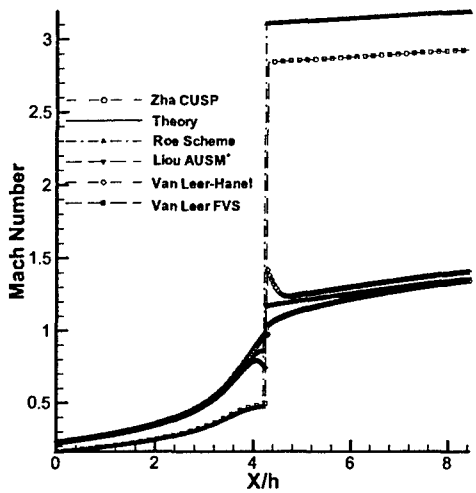

Figure 12.9: Computed Mach numb distributions for the converging-diverging nozzle

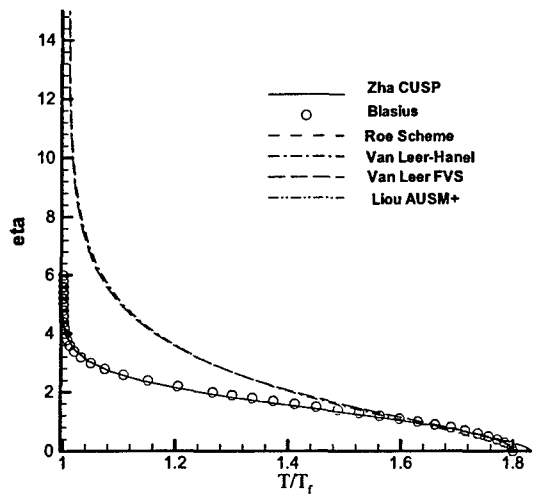

Figure 12.11: Computed temperature profiles of the laminar boundary layer using 1st order schemes

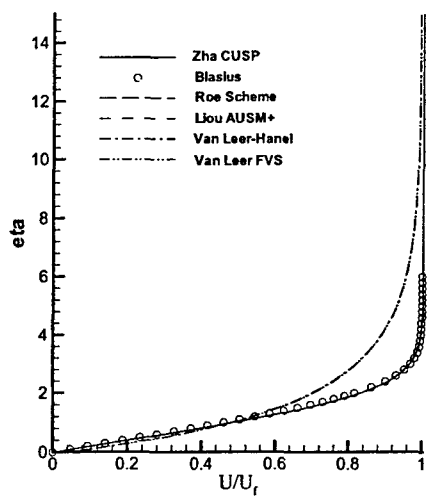

Figure 12.10: Computed velocity profiles of the laminar boundary layer using 1st order schemes

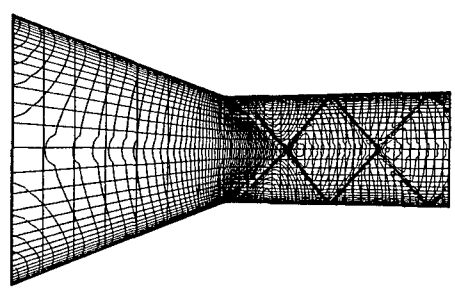

Figure 12.12: Computed Mach number contours using the Zha CUSP scheme

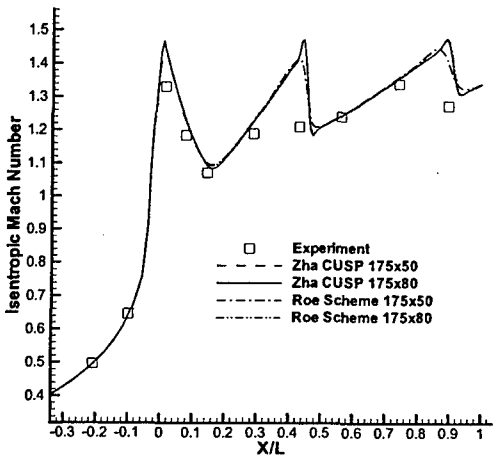

Figure 12.13: Adiabatic Mach number distribution computed on the wall surface of the nozzle

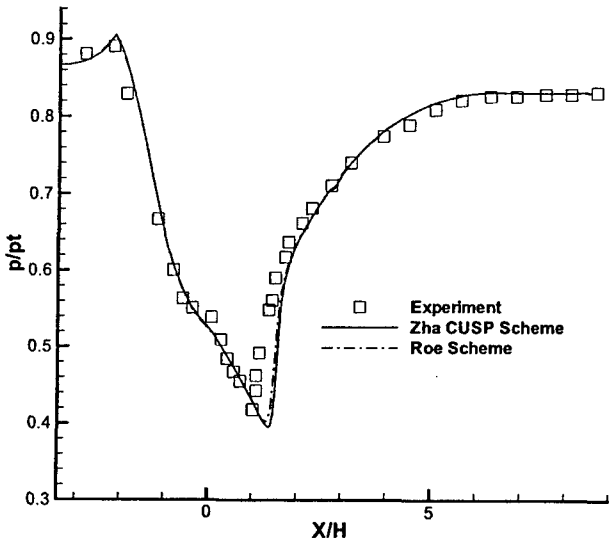

Figure 12.15: Static pressure distribution computed on the upper surface of the inlet-diffuser ($p_{out}/p_t = .83$)

Figure 12.14: Computed Mach number contours using the Zha CUSP scheme with $p_{out}/p_t = .83$

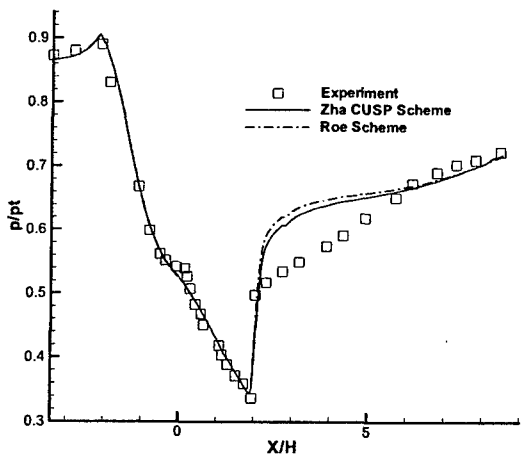

Figure 12.16: Static pressure distribution computed on the upper surface of the inlet-diffuser ($p_{out}/p_t = .72$)

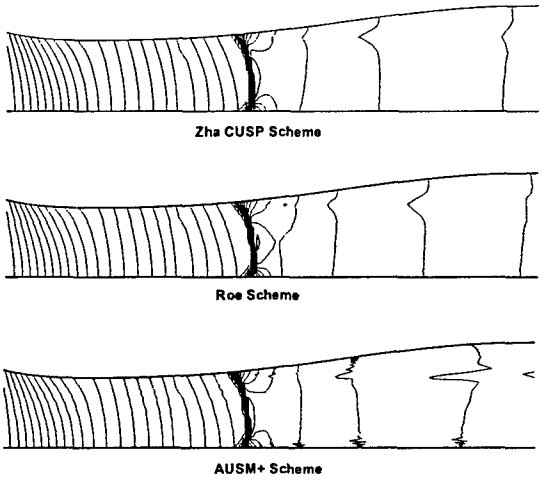

Figure 12.17: Comparison of computed pressure contours using the Zha CUSP scheme, Roe Scheme, and Liou's AUSM$^+$ scheme ($p_{out}/p_t = .72$)

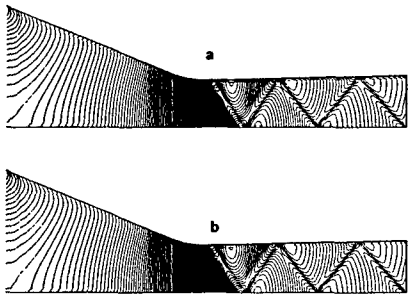

Figure 12.18: Computed Mach number contours using the Zha CUSP (a) and Zha CUSP2 scheme (b)

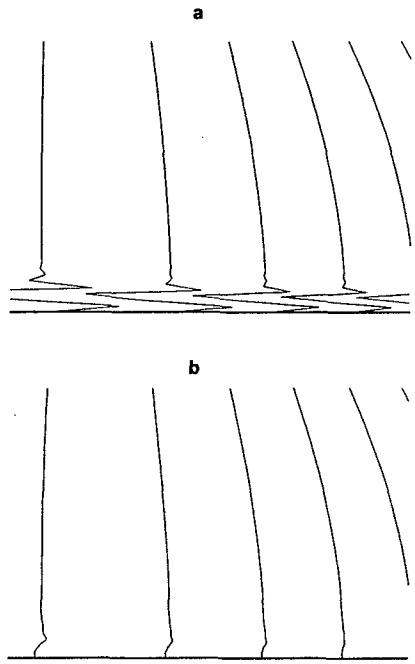

Figure 12.19: Zoomed temperature contours near the symmetric boundary using the Zha CUSP(a) and Zha CUSP2 scheme(b)

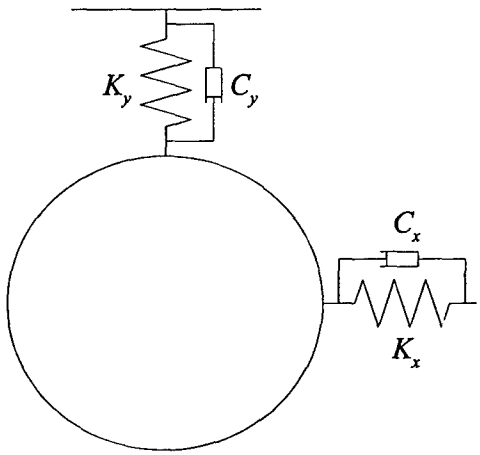

Figure 12.20: Sketch of the elastically mounted cylinder.

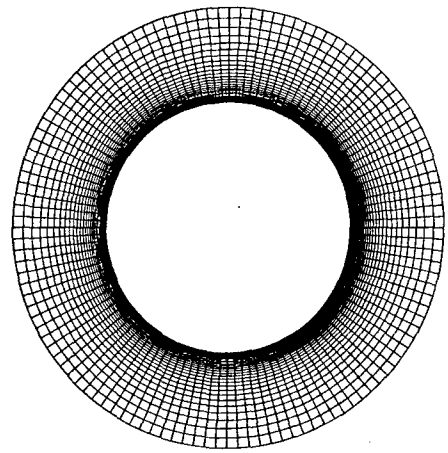

Figure 12.22: The near wall zone mesh around the solid surface of the cylinder.

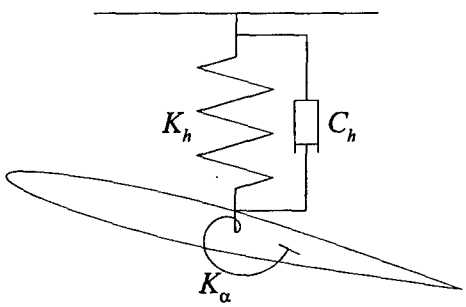

Figure 12.21: Sketch of the elastically mounted airfoil.

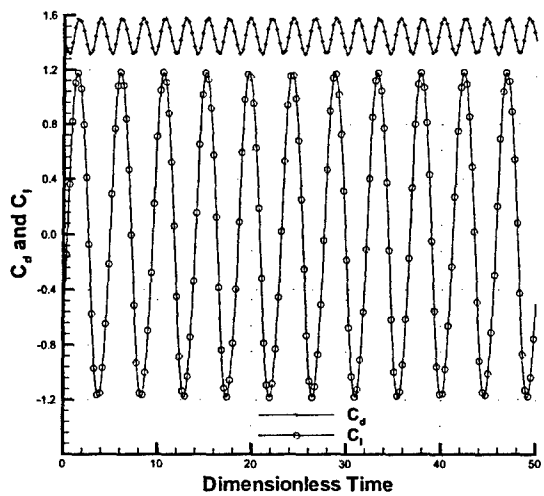

Figure 12.23: Time histories of the lift and drag coefficients of the stationary cylinder due to vortex shedding.

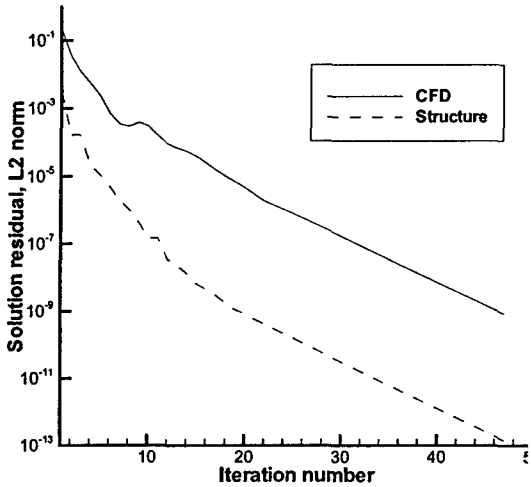

Figure 12.24: Typical convergence histories of the CFD and structural solvers within one physical time step.

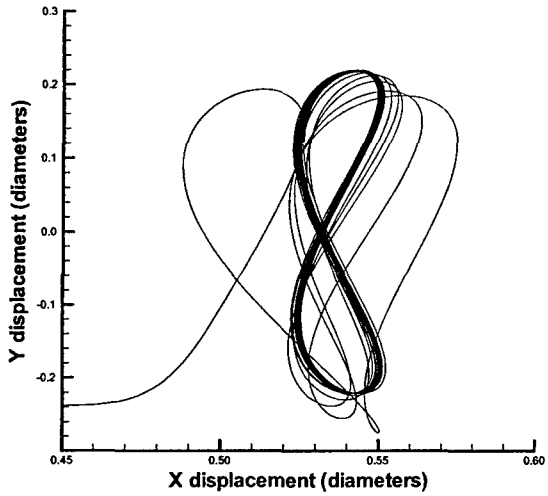

Figure 12.26: The trajectory of the center position of the oscillating cylinder, $\mu_s = 1.2732$, $\zeta = 0.63326$.

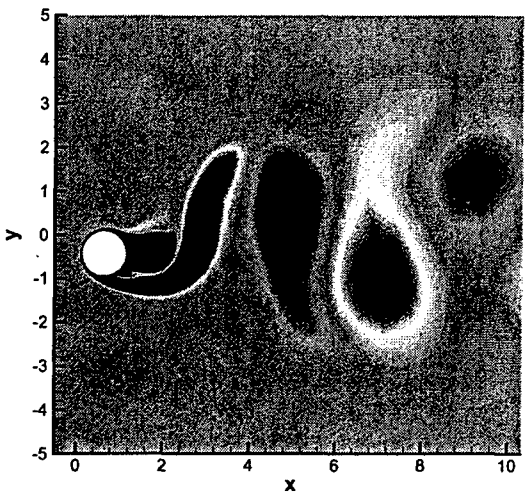

Figure 12.25: Vorticity contours around oscillating cylinder, $\mu_s = 1.2732$, $\zeta = 0.03166$.

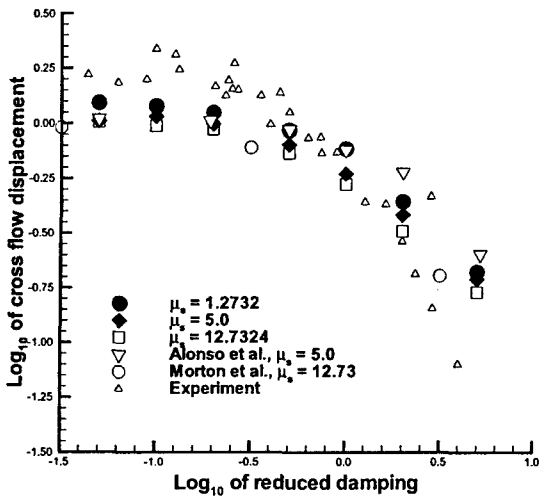

Figure 12.27: Comparison of the computed amplitude with Griffin's experimental data for the elastically mounted cylinder.

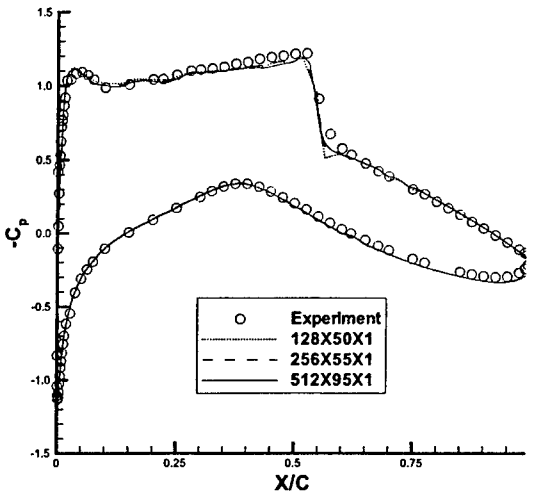

Figure 12.28: Surface pressure coefficient comparison for RAE 2822 airfoil at M=0.729.

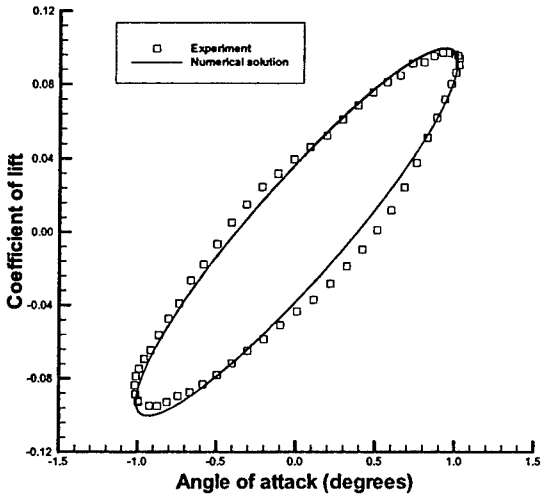

Figure 12.30: Comparison of computed lift coefficient with Davis' experimental data for the forced pitching airfoil.

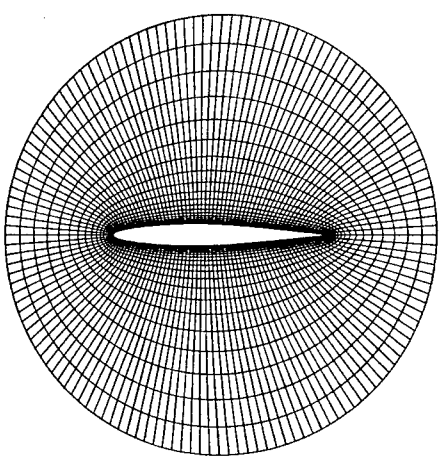

Figure 12.29: The near wall O-type mesh around the NACA 64A010 airfoil.

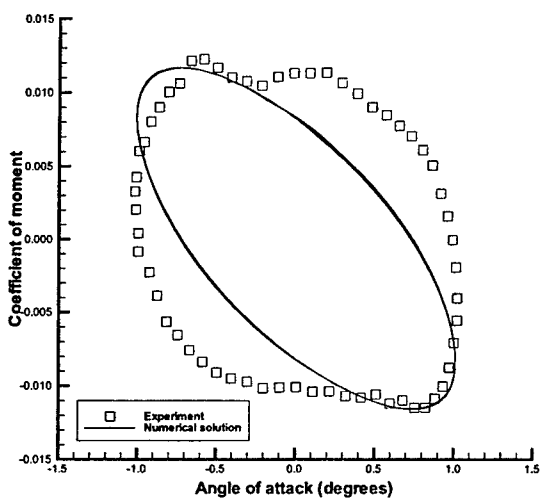

Figure 12.31: Comparison of computed moment coefficient with Davis' experimental data for the forced pitching airfoil.

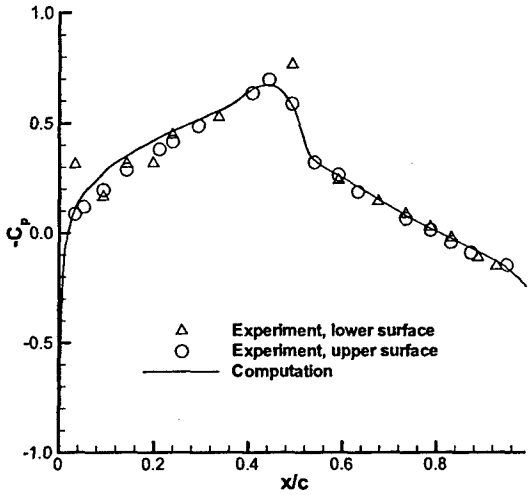

Figure 12.32: Comparison of the mean pressure distribution along the pitching airfoil.

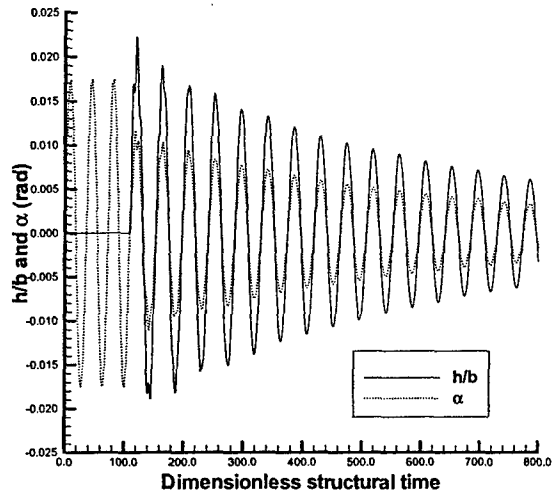

Figure 12.34: Time histories of plunging and pitching displacements for $M_\infty = 0.825$ and $V^* = 0.55$ - Damped response.

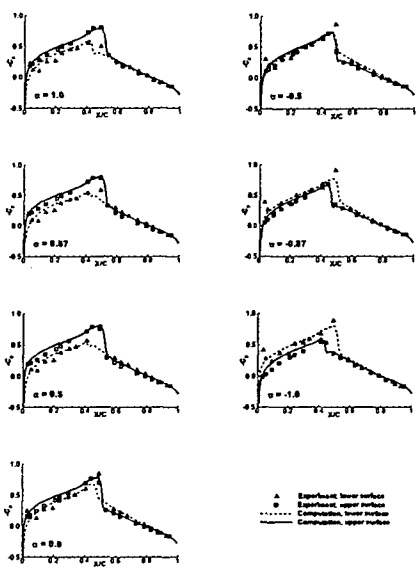

Figure 12.33: Comparison of the instantaneous pressure distributions at various angles of attack.

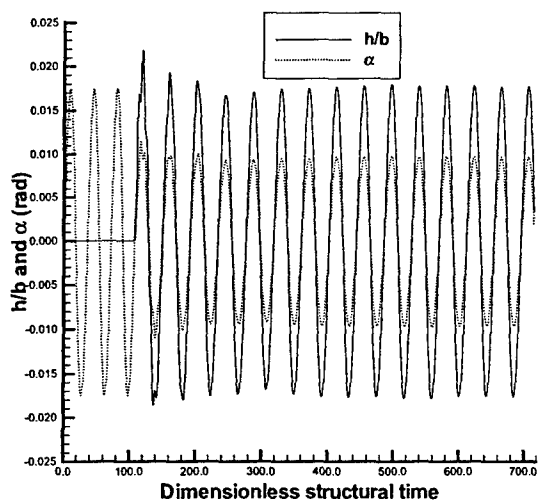

Figure 12.35: Time histories of plunging and pitching displacements for $M_\infty = 0.825$ and $V^* = 0.615$ - Neutrally stable response.

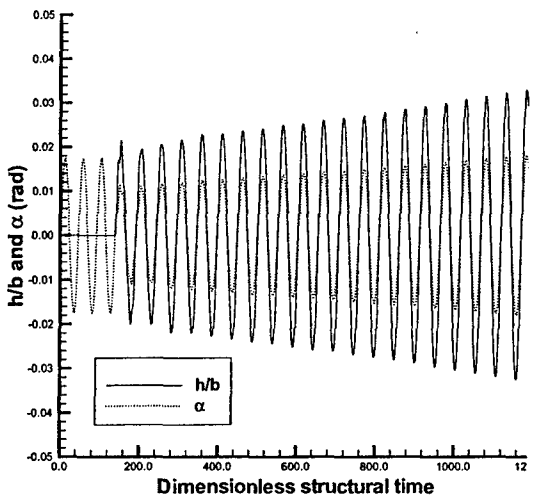

Figure 12.36: Time histories of plunging and pitching displacements for $M_\infty = 0.825$ and $V^* = 0.70$ - Diverging response.

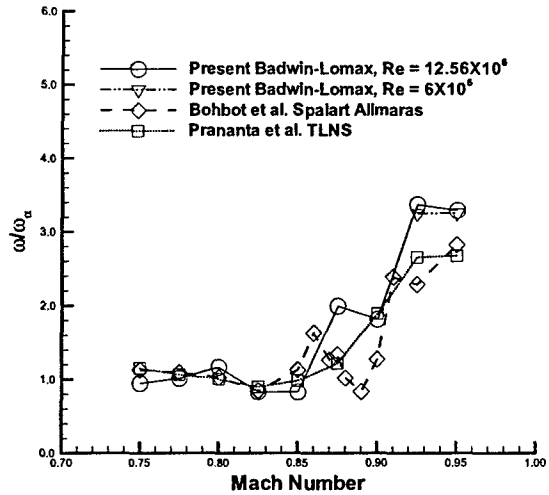

Figure 12.38: Comparison of computed flutter boundaries - $\frac{\omega}{\omega_\alpha}$ versus Mach number.

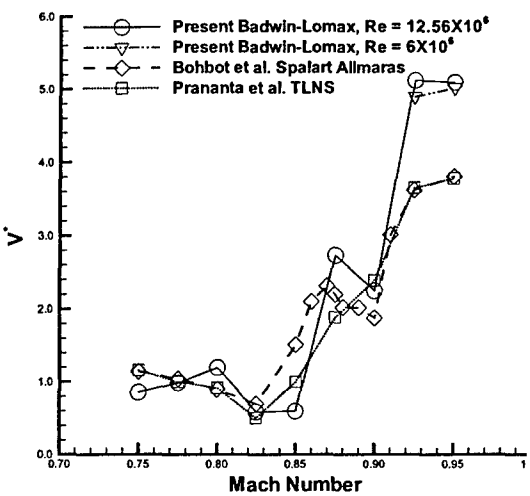

Figure 12.37: Comparison of computed flutter boundaries - Speed index versus Mach number.

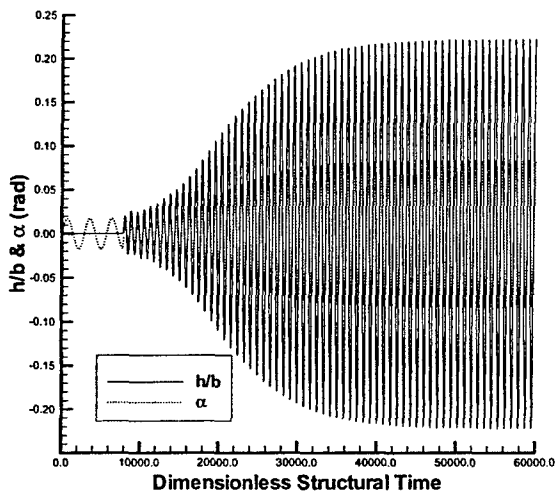

Figure 12.39: Time histories of plunging and pitching displacements for $M_\infty = 0.925$ and $V^* = 5.5$ - Limit Cycle Oscillation.

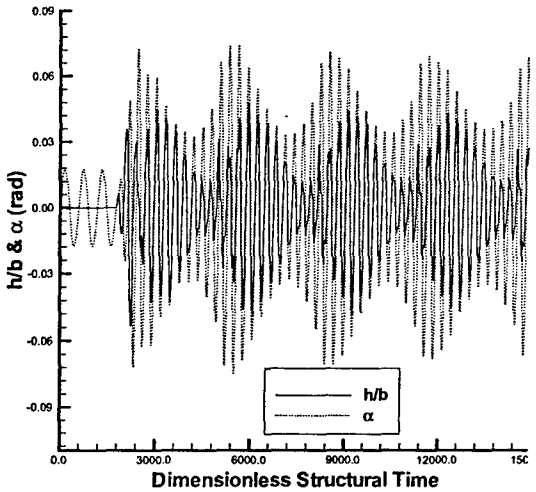

Figure 12.40: Time histories of plunging and pitching displacements for $M_\infty = 0.9$ and $V^* = 2.5$ with the second mode vibration dominant.

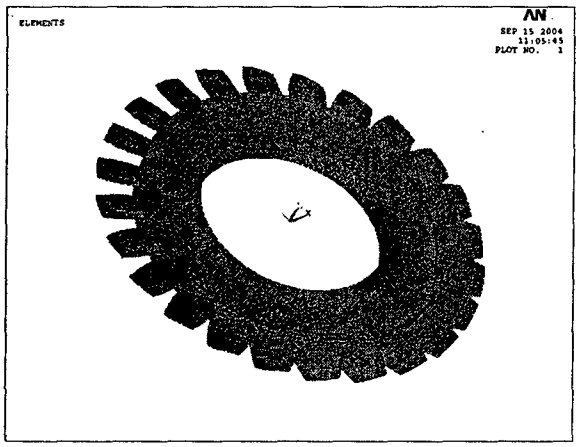

Figure 12.42: Finite element model of 24-blade disk.

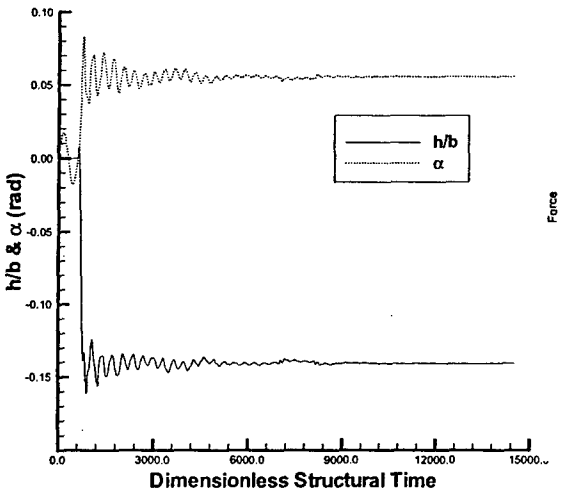

Figure 12.41: Time histories of plunging and pitching displacements for $M_\infty = 0.875$ and $V^* = 2.5$ - 'Standing' status.

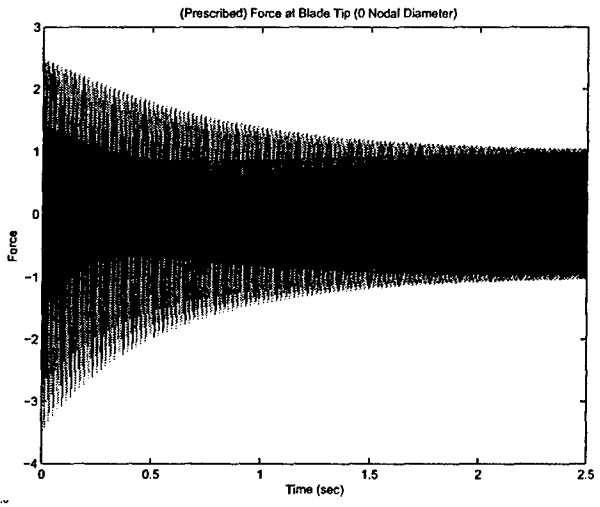

Figure 12.43: Prescribed force at blade tip, zero0 nodal diameter at low frequency.

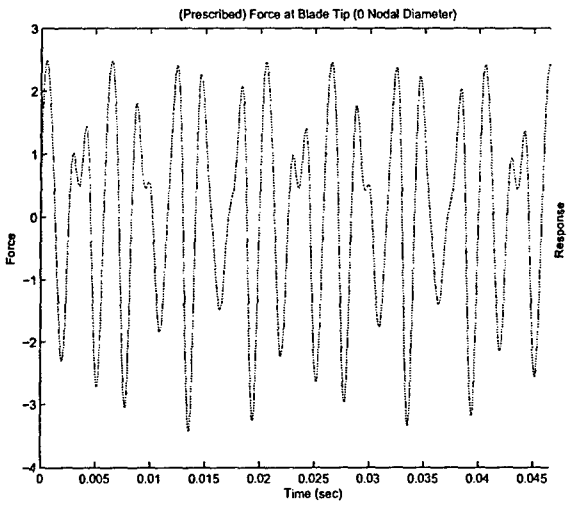

Figure 12.44: Prescribed force at blade tip, zero nodal diameter at low frequency.

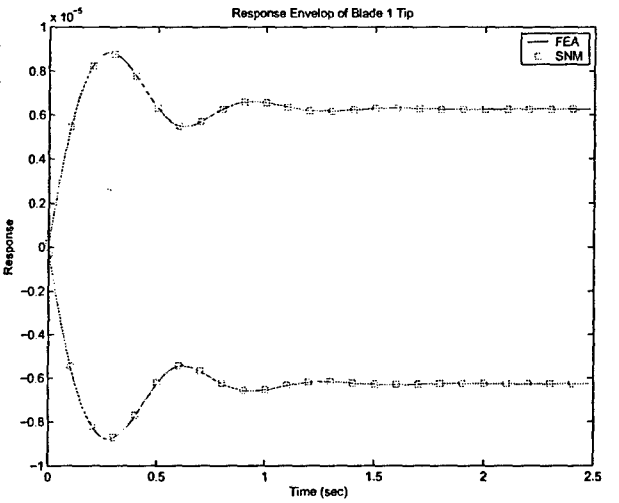

Figure 12.46: Comparison of the predicted transient response at low frequency.

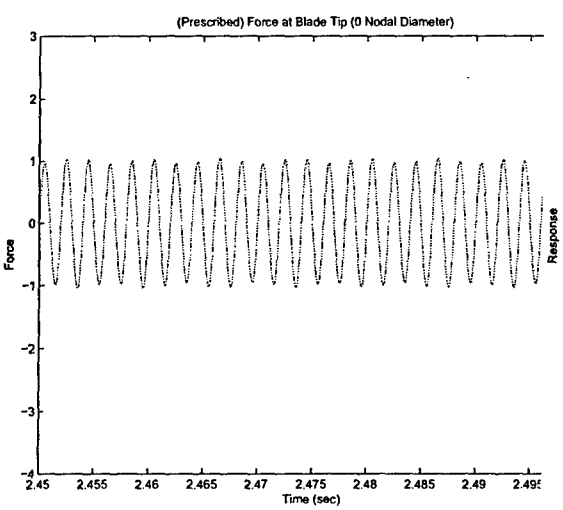

Figure 12.45: Prescribed force at blade tip, zero nodal diameter at low frequency.

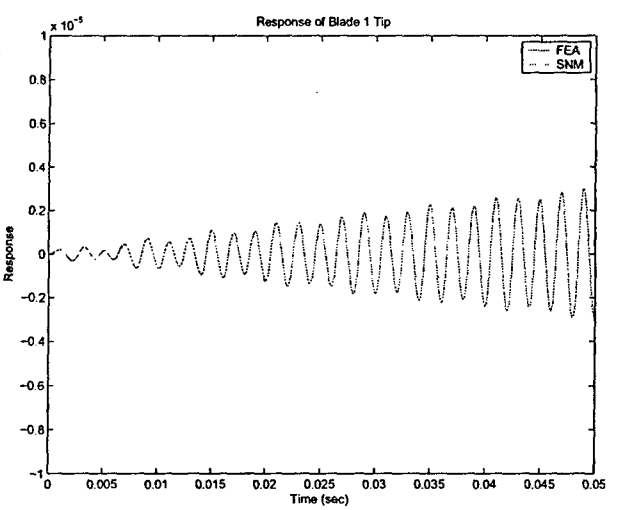

Figure 12.47: Comparison of the predicted transient response at low frequency.

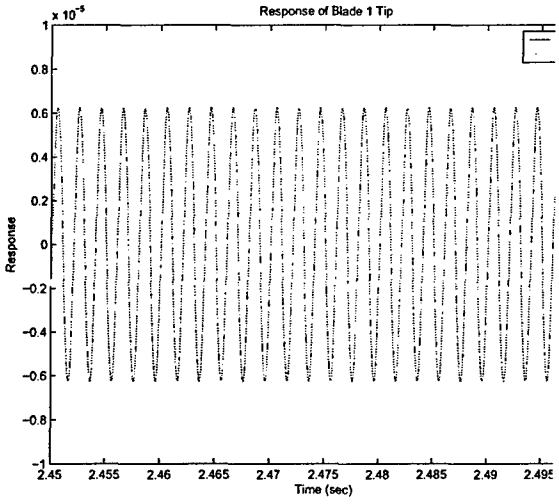

Figure 12.48: Comparison of the predicted transient response at low frequency.

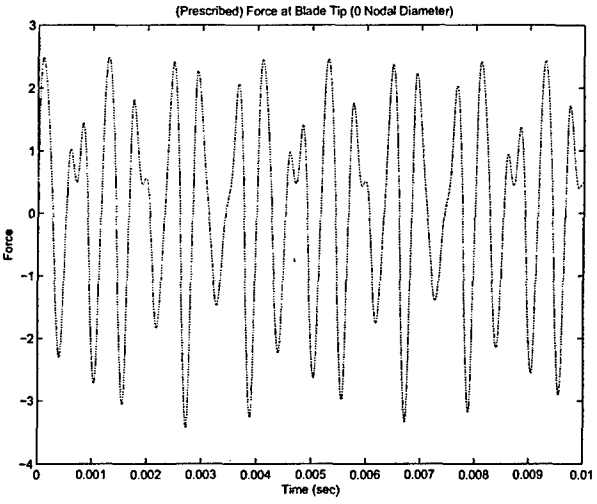

Figure 12.50: Prescribed force at blade tip, zero nodal diameter at high frequency.

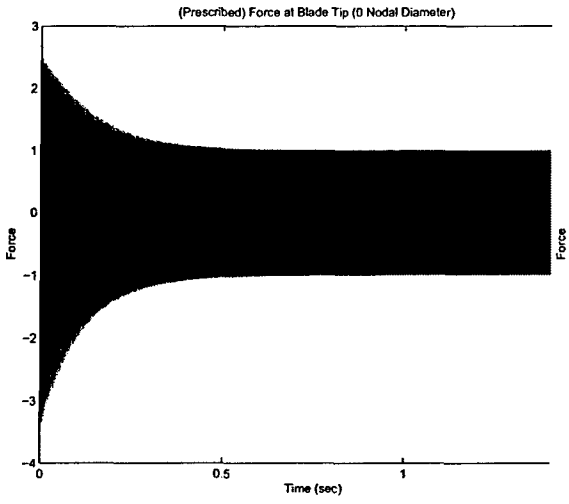

Figure 12.49: Prescribed force at blade tip, zero nodal diameter at high frequency.

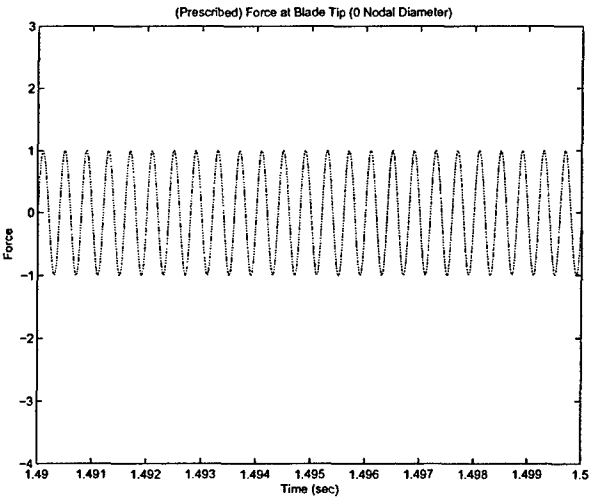

Figure 12.51: Prescribed force at blade tip, zero nodal diameter at high frequency.

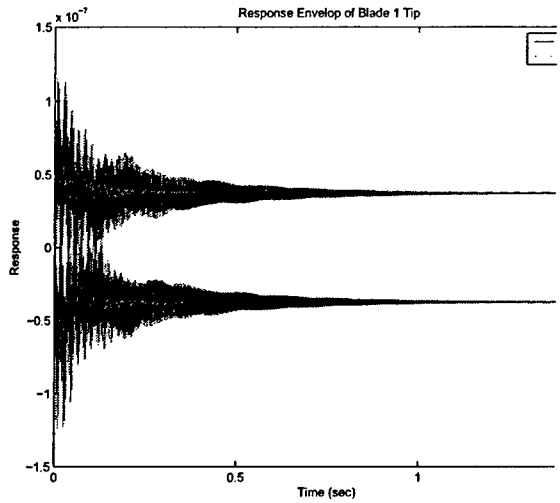

Figure 12.52: Comparison of the predicted transient response at high frequency.

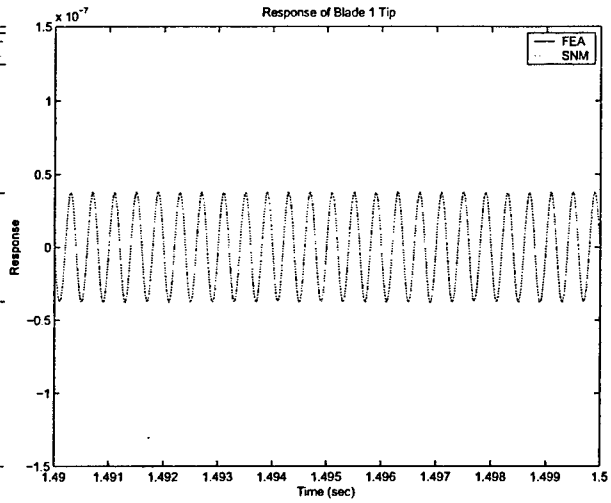

Figure 12.54: Comparison of the predicted transient response at high frequency.

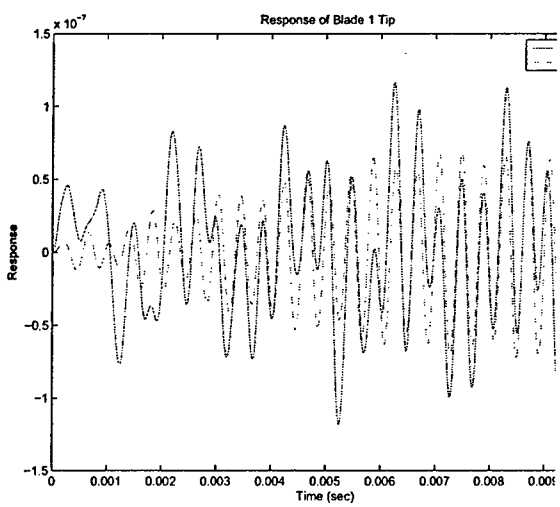

Figure 12.53: Comparison of the predicted transient response at high frequency.

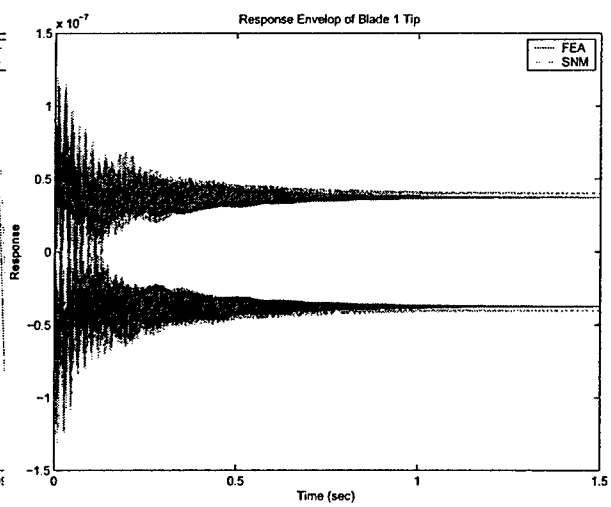

Figure 12.55: Comparison of the predicted transient response at high frequency.

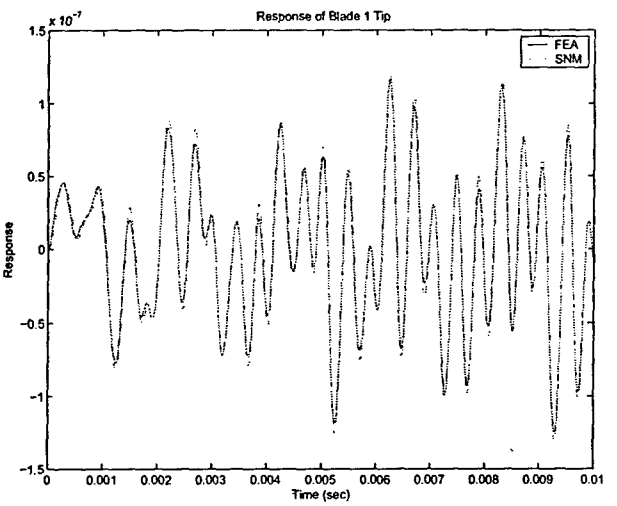

Figure 12.56: Comparison of the predicted transient response at high frequency.

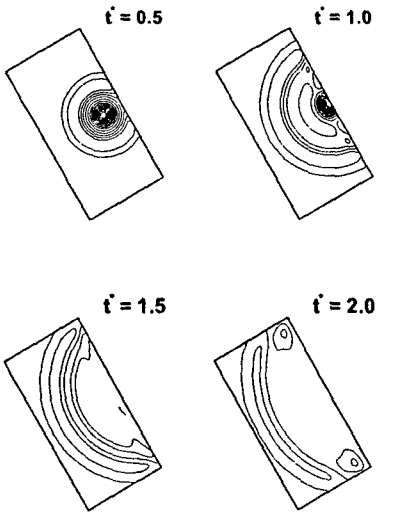

Figure 12.58: Density contours at four instants for a vortex leaving the domain using imposed exit static pressure boundary conditions.

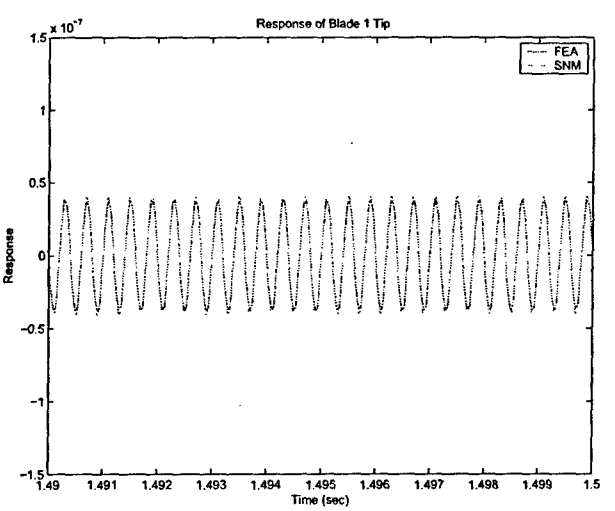

Figure 12.57: Comparison of the predicted transient response at high frequency.

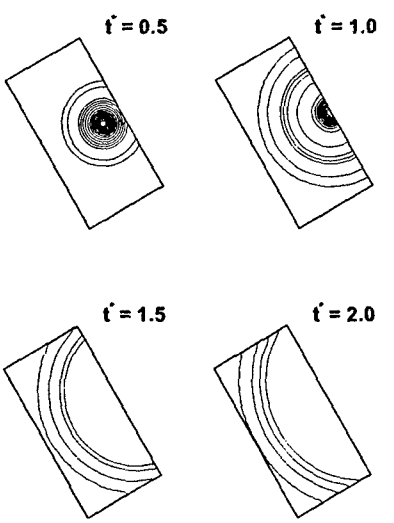

Figure 12.59: Density contours at four instants for a vortex leaving the domain using NRBC exit boundary conditions.

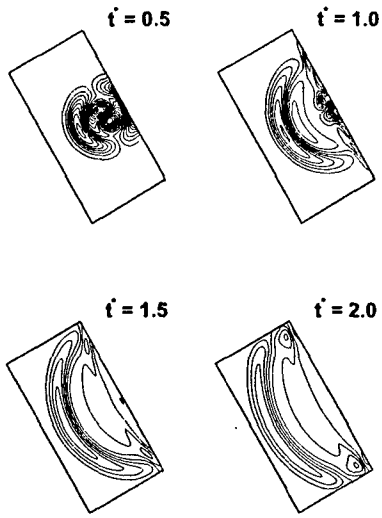

Figure 12.60: $(u^{\tau} - u^{\tau}{}_{\infty})/u^{\tau}{}_{\infty}$ contou at four instants for a vortex leaving t domain using imposed exit static pressu boundary conditions.

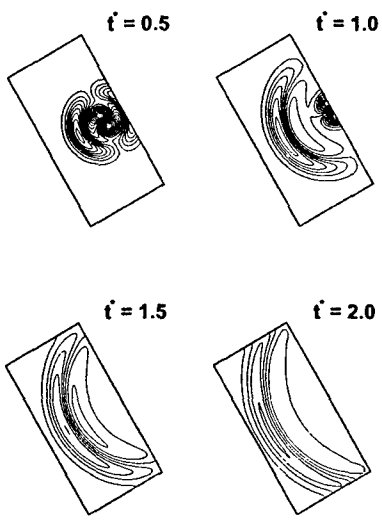

Figure 12.61: $(u^{\tau} - u^{\tau}{}_{\infty})/u^{\tau}{}_{\infty}$ contours at three instants for a vortex leaving the domain using NRBC exit boundary conditions.

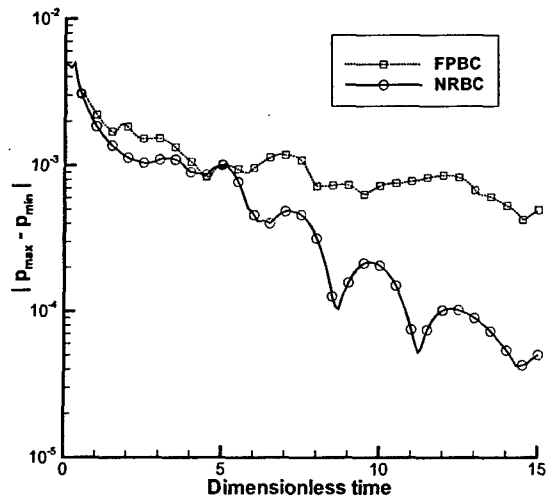

Figure 12.62: Time histories of $|p_{max} - p_{min}|$ for a vortex leaving the domain.

Figure 12.63: *Mach* number contours the inlet diffuser.

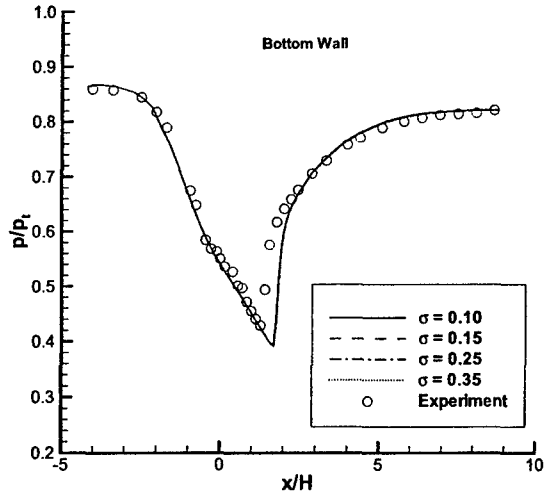

Figure 12.65: Steady state pressure distribution along the bottom wall for $p_{outlet}/p_t = 0.82$.

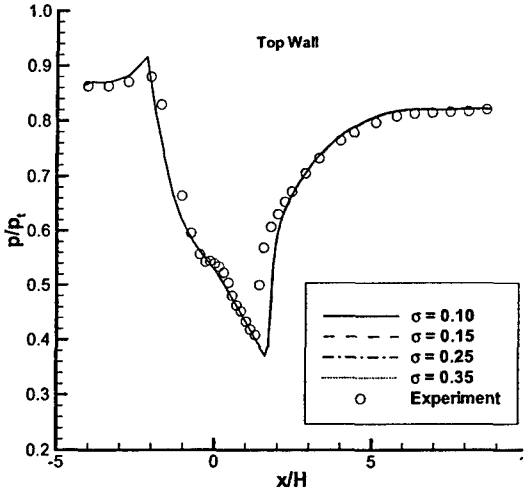

Figure 12.64: Steady state pressure dist bution along the top wall for p_{outlet}/p_t 0.82.

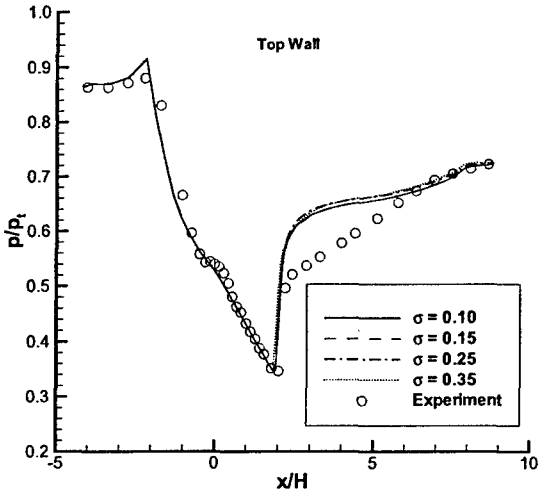

Figure 12.66: Steady state pressure distribution along the top wall for $p_{outlet}/p_t = 0.72$.

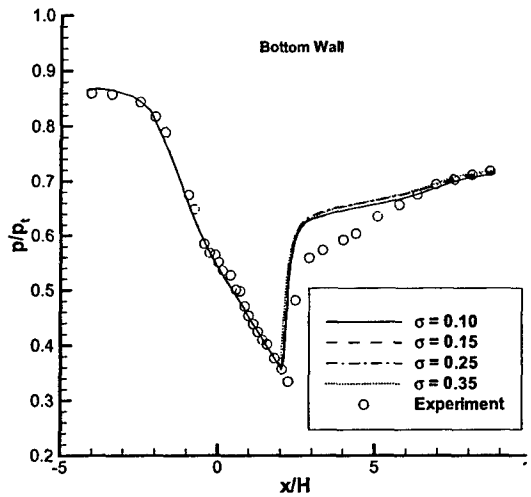

Figure 12.67: Steady state static pressure distribution along the bottom wall for $p_{outlet}/p_t = 0.72$.

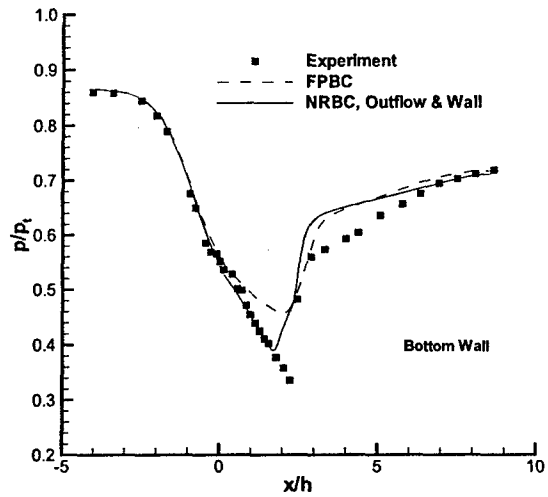

Figure 12.69: Time averaged unsteady pressure distribution along the bottom wall for $p_{outlet}/p_t = 0.72$.

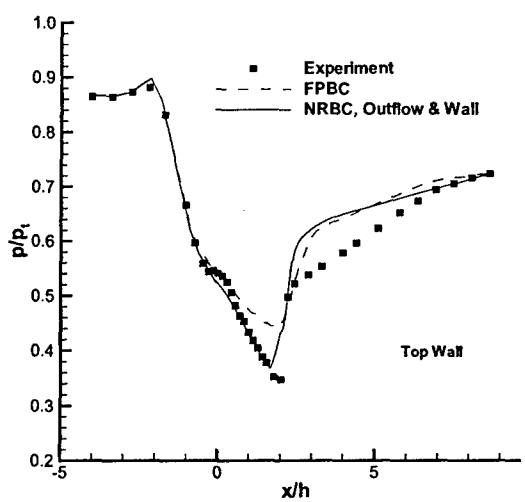

Figure 12.68: Time averaged unsteady pressure distribution along the top wall for $p_{outlet}/p_t = 0.72$.

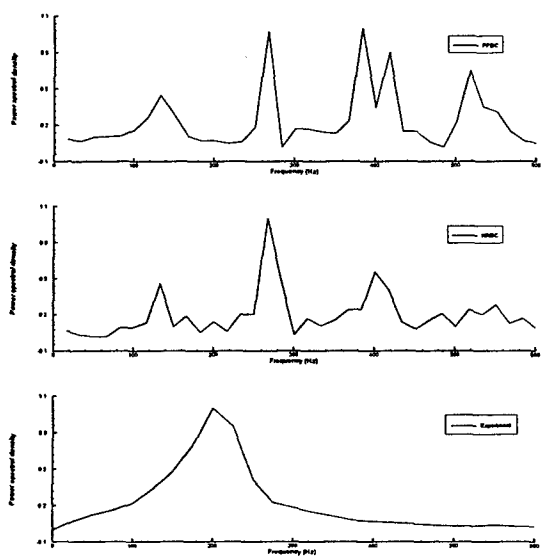

Figure 12.70: Power spectral density for the static pressure fluctuations at $x/H = 14.218$, $p_{outlet}/p_t = 0.72$.

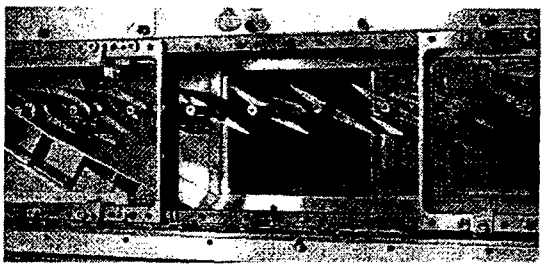

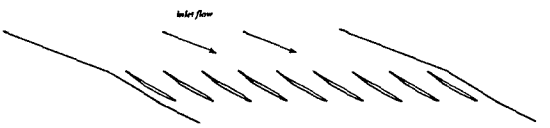

Figure 12.71: NASA transonic flutter cascade structure

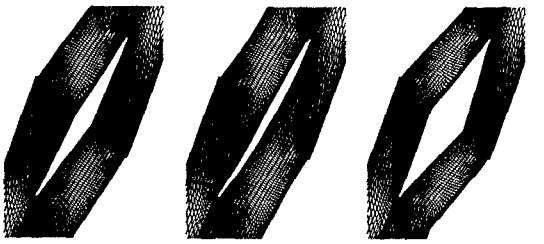

(a) bottom (b) midspan (c) top

Figure 12.73: Bottom, mid-span and top planes of the cascade mesh

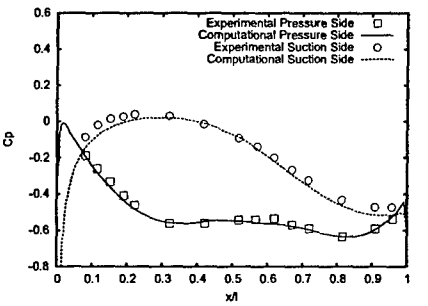

Figure 12.74: Mid-span static pressure distribution at Mach number 0.5

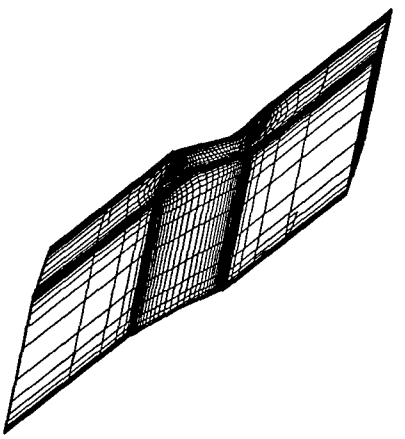

Figure 12.72: Cascade 3D mesh

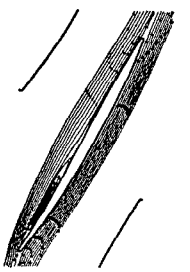

Figure 12.75: Mid-span Stream Lines at Incidence Angle 10°

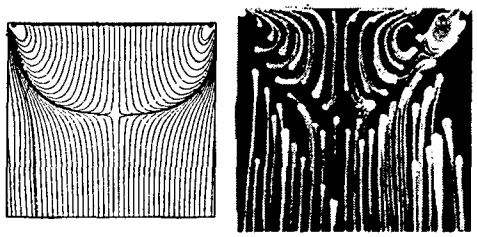

Figure 12.76: Mid-span Suction Surface Streamlines at Incidence Angle 10°

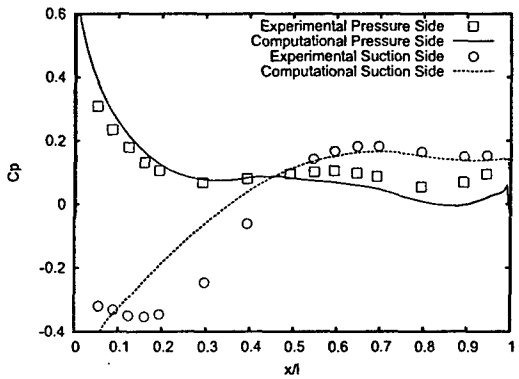

Figure 12.77: Mid-span Surface Pressure Distribution at Incidence Angle 10°

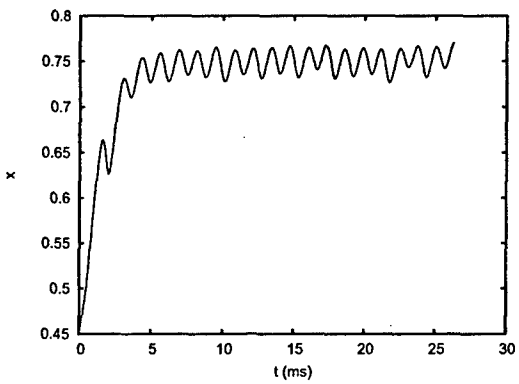

Figure 12.78: Separation Zone Length Variation with Time

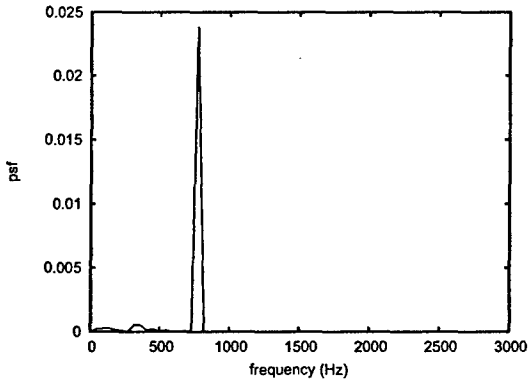

Figure 12.79: Separation Zone Length Variation Frequency Spectrum

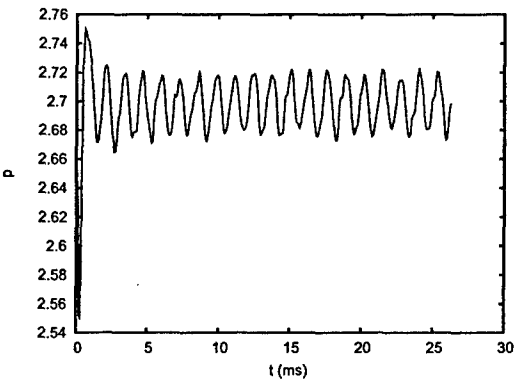

Figure 12.80: Suction Surface Check Point Pressure Variation with Time

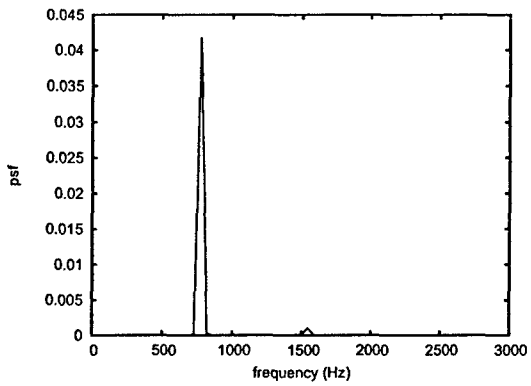

Figure 12.81: Suction Surface Check Point Pressure Frequency Spectrum

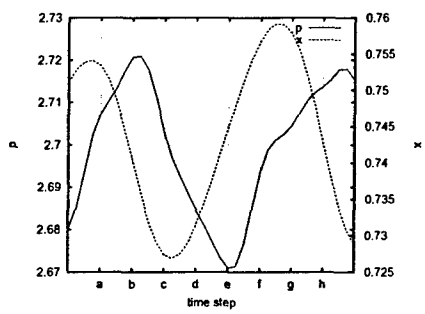

Figure 12.82: Check Point Pressure and Separation Locations Relation

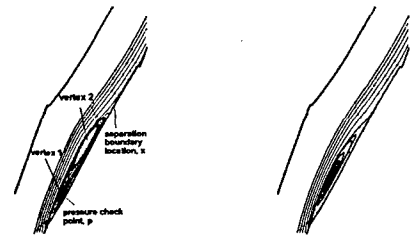

a, t =4.4305 ms, $8.4t_c$ b, t =4.6415 ms, $8.8t_c$

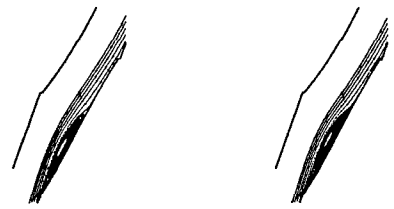

c, t =4.8524 ms, $9.2t_c$ d, t =5.0634 ms, $9.6t_c$

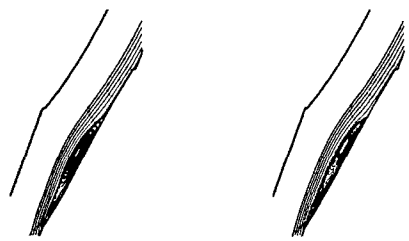

e, t =5.2744 ms, $10.0t_c$ f, t =5.4854 ms, $10.4t_c$

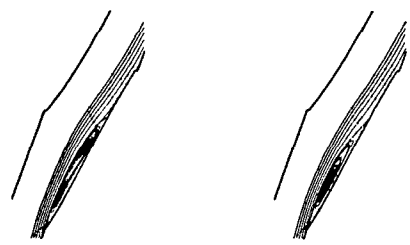

g, t =5.6964 ms, $10.8t_c$ h, t =5.9073 ms, $11.2t_c$

Figure 12.83: Separation Bubble Evolution

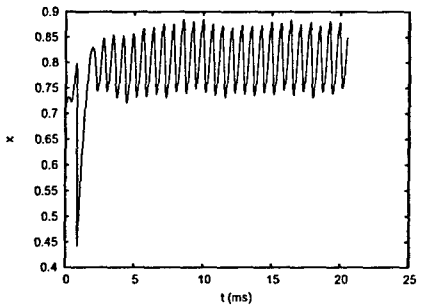

Figure 12.84: Separation Zone Length Oscillation (Ma=0.8)

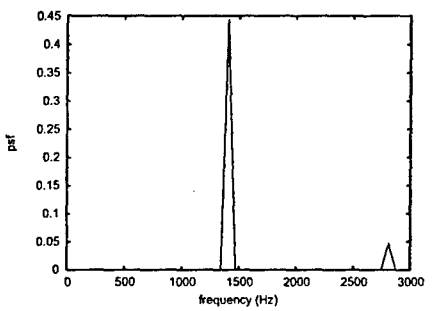

Figure 12.85: Separation Zone Length Oscillation Frequency Spectrum (Ma=0.8)

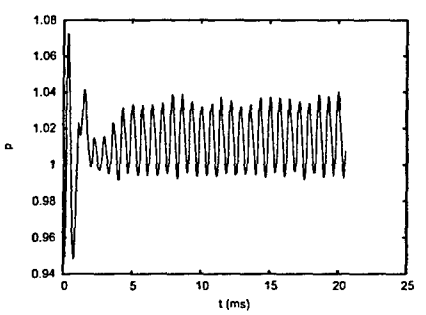

Figure 12.86: Checkpoint Pressure Oscillation (Ma=0.8)

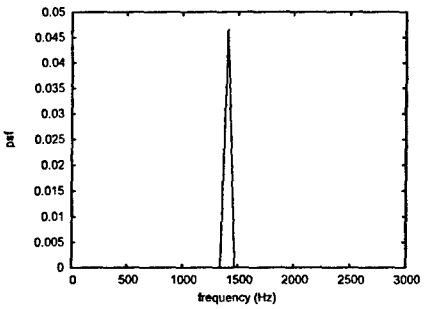

Figure 12.87: Checkpoint Pressure Oscillation Frequency Spectrum (Ma=0.8)

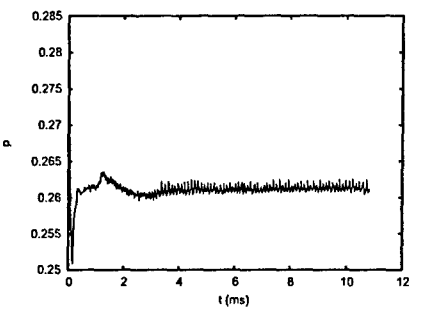

Figure 12.88: Checkpoint Pressure Oscillation (Ma=1.18)

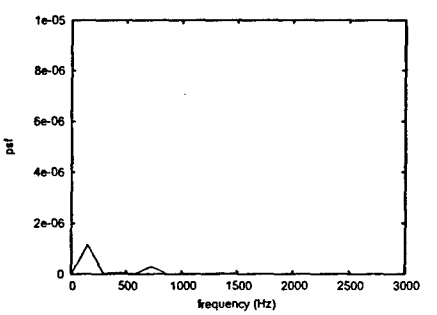

Figure 12.89: Checkpoint Pressure Oscillation Frequency Spectrum (Ma=1.18)

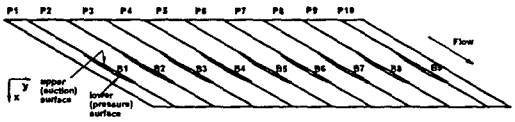

Figure 12.90: Cascade structure and CFD setup

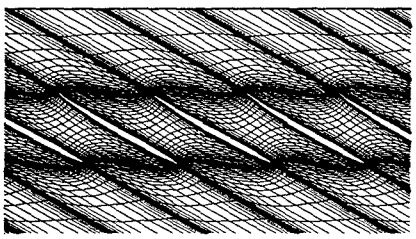

Figure 12.91: Cascade Mesh

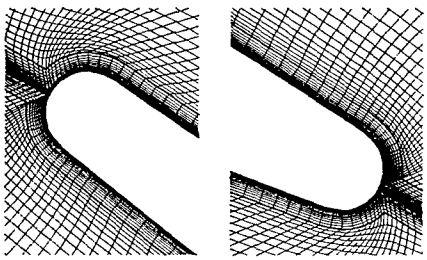

Figure 12.92: Additional mesh layer for better orthogonality

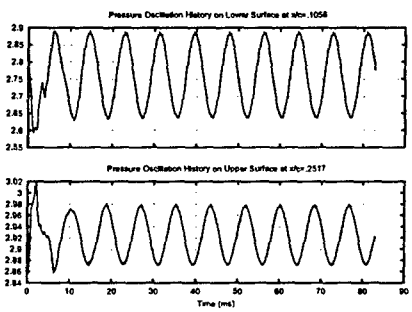

Figure 12.93: Pressure oscillation history

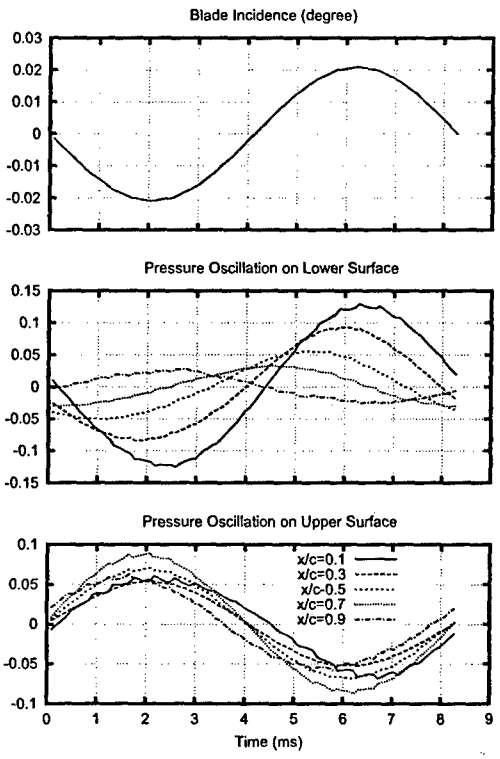

Figure 12.94: Pressure oscillation at different chordwise locations

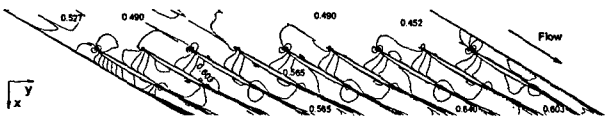

Figure 12.95: Mach number contours of the cascade

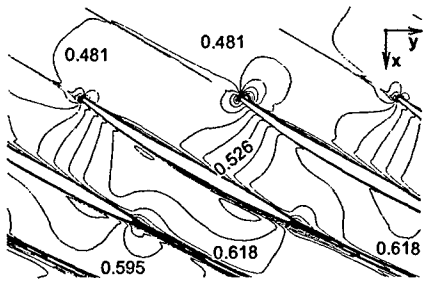

Figure 12.96: Mach number contours at different time steps

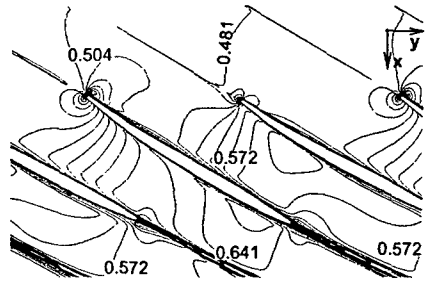

Figure 12.99: Mach number contours at different time steps

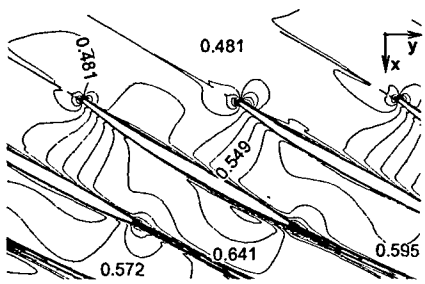

Figure 12.97: Mach number contours at different time steps

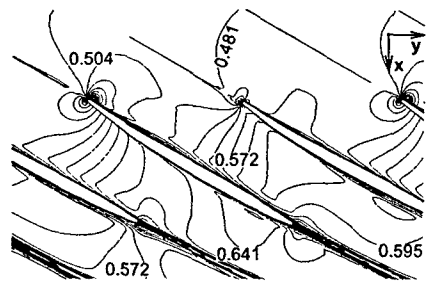

Figure 12.100: Mach number contours at different time steps

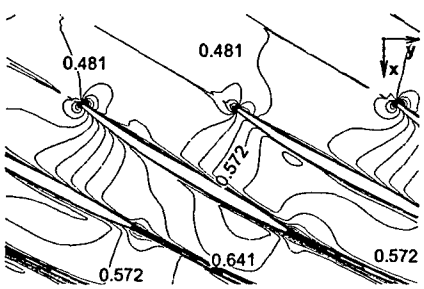

Figure 12.98: Mach number contours at different time steps

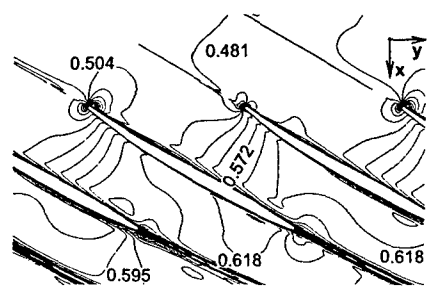

Figure 12.101: Mach number contours at different time steps

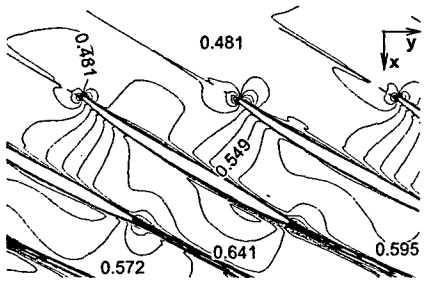

Figure 12.102: Mach number contours at different time steps

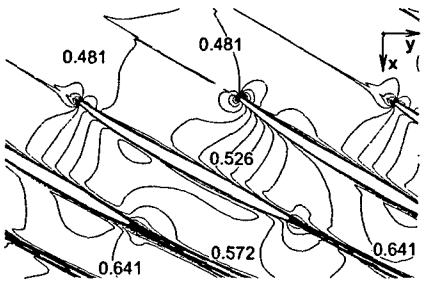

Figure 12.103: Mach number contours at different time steps

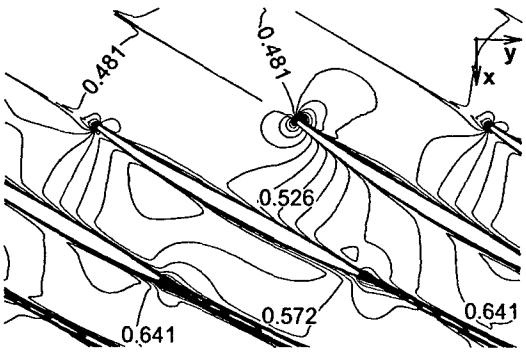

Figure 12.104: Mach number contours at different time steps

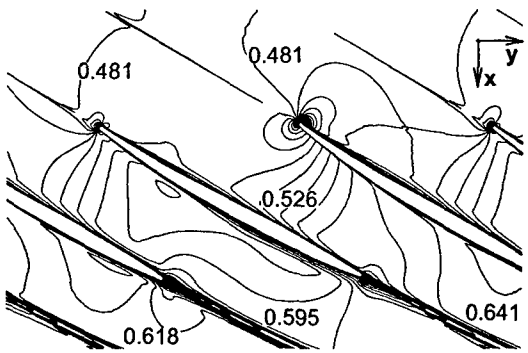

Figure 12.105: Mach number contours at different time steps

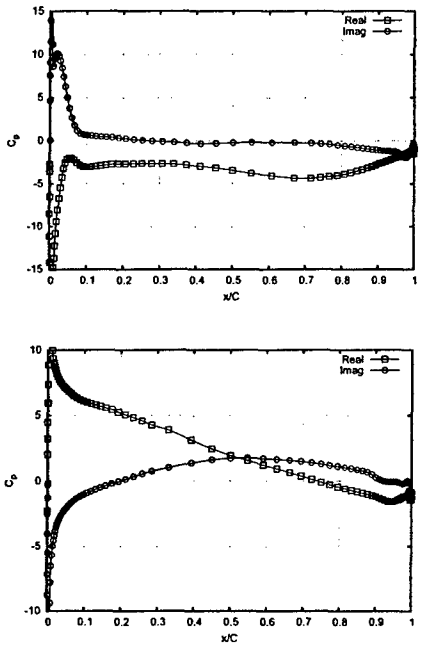

Figure 12.106: Unsteady pressure analysis

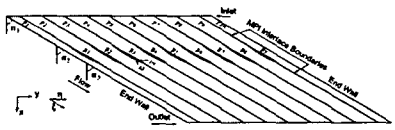

Figure 12.107: Computation Domain Configuration

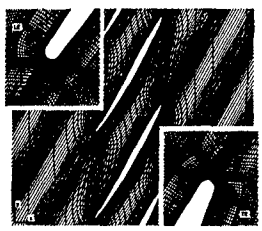

Figure 12.108: Computation mesh

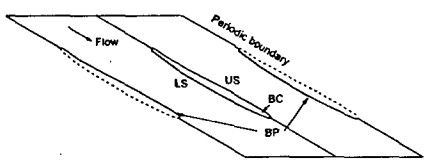

Figure 12.109: Two-passage cascade periodic computation domain

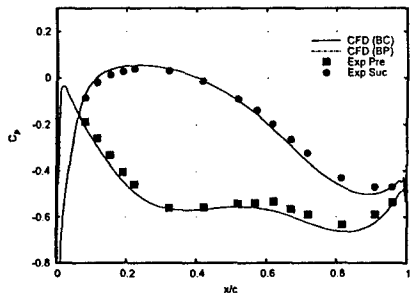

Figure 12.110: Steady state pressure coefficient in 2-passage cascade

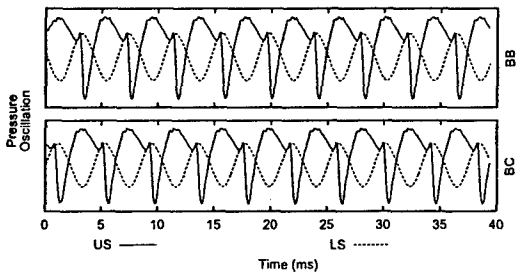

Figure 12.111: Pressure oscillation history, k_c= 0.8

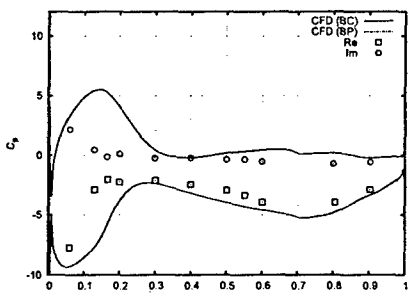

Figure 12.112: Unsteady pressure coefficient on upper surface in 2-passage cascade, $k_c = 0.8$

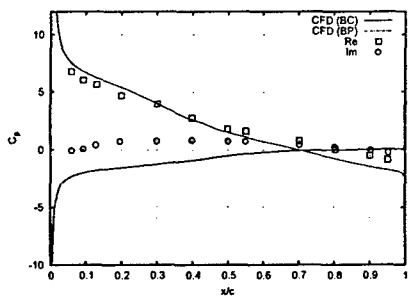

Figure 12.113: Unsteady pressure coefficient on lower surface in 2-passage cascade, k_c= 0.8

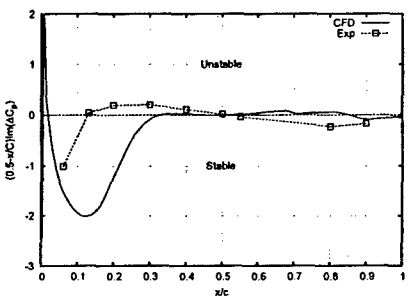

Figure 12.114: Local stability analysis in 2-passage cascade, k_c=0.8

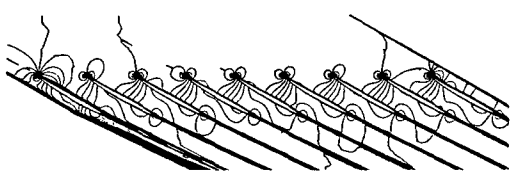

Figure 12.115: Steady state Mach contours in full scale cascade

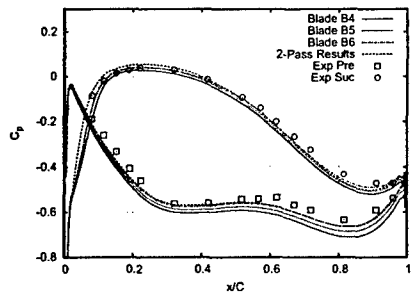

Figure 12.116: Steady state pressure coefficient in full scale cascade

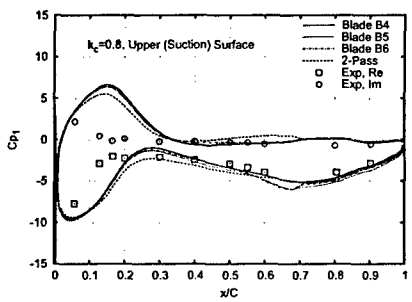

Figure 12.117: Unsteady state pressure coefficient on upper surface, k_c =0.8

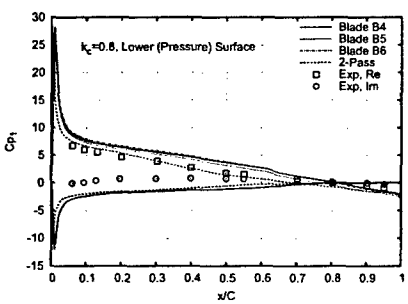

Figure 12.118: Unsteady state pressure coefficient on lower surface, k_c =0.8

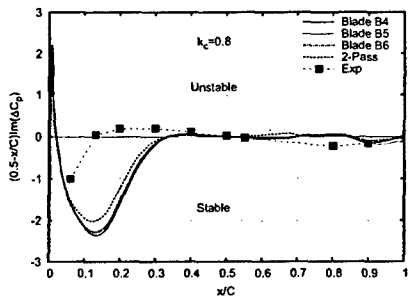

Figure 12.119: Local stability analysis, k_c =0.8

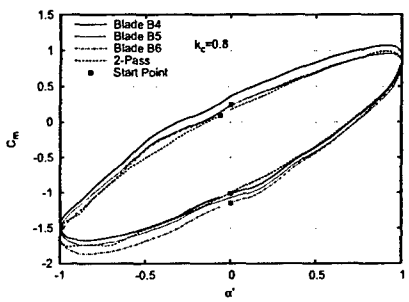

Figure 12.120: Unsteady aerodynamic moment oscillation, k_c =0.8

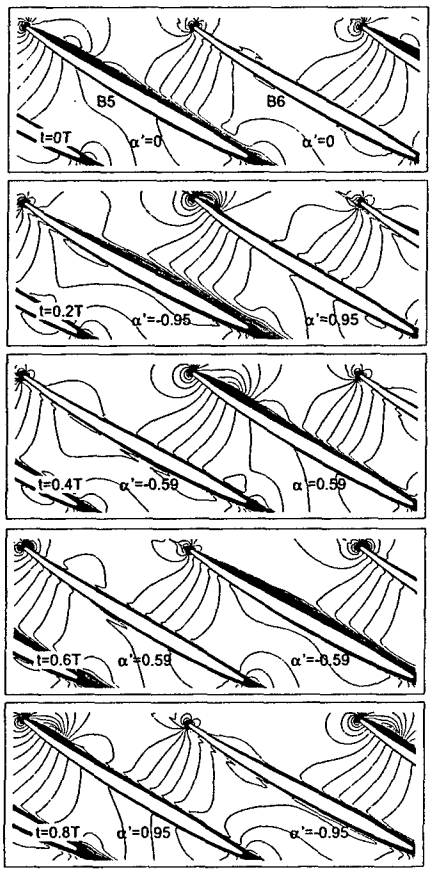

Figure 12.122: Unsteady Mach number contours, k_c =0.8

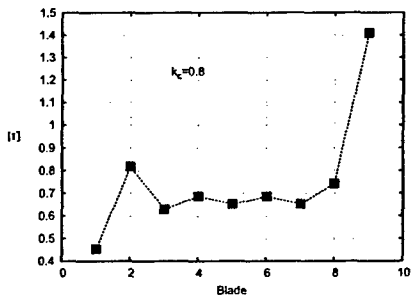

Figure 12.121: Damping coefficient distribution, k_c =0.8

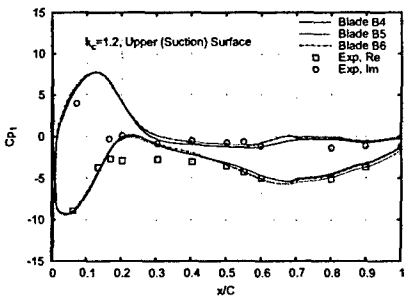

Figure 12.123: Unsteady pressure coefficient on upper surface, k_c =1.2

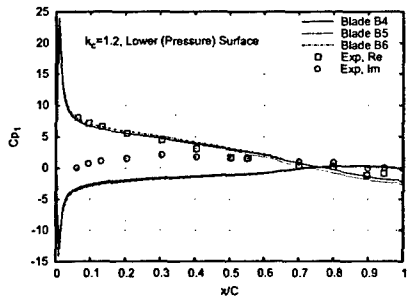

Figure 12.124: Unsteady pressure coefficient on lower cascade, k_c =1.2

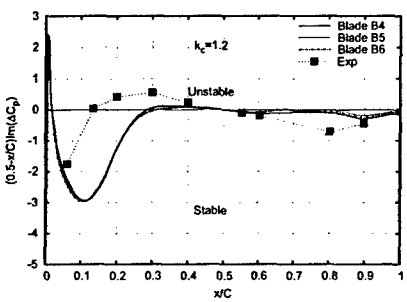

Figure 12.125: Local stability analysis, k_c =1.2

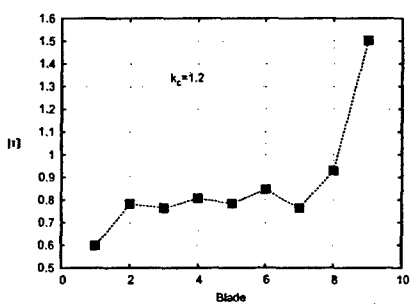

Figure 12.126: Damping coefficient distribution, k_c =1.2

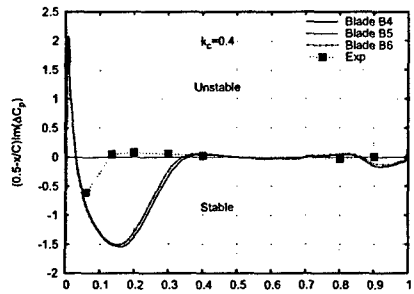

Figure 12.127: Local stability analysis, k_c =0.4

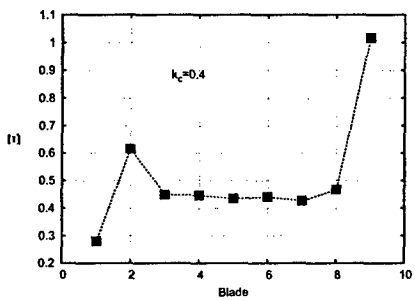

Figure 12.128: Damping coefficient distribution, k_c =0.4

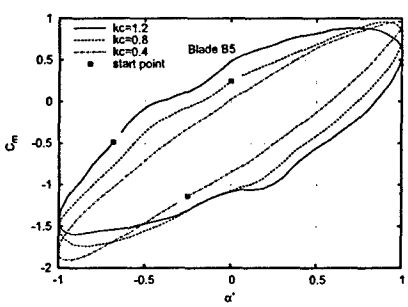

Figure 12.129: Unsteady aerodynamic moment oscillation comparison

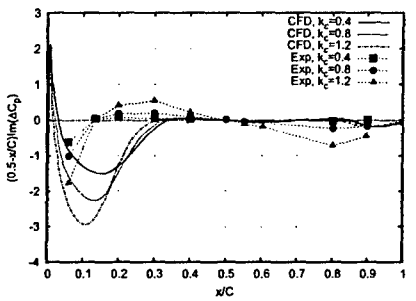

Figure 12.130: Local stability analysis comparison

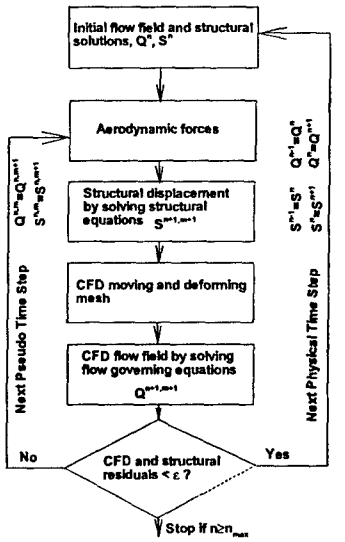

Figure 12.132: Fully coupled flow-structure interaction calculation procedure

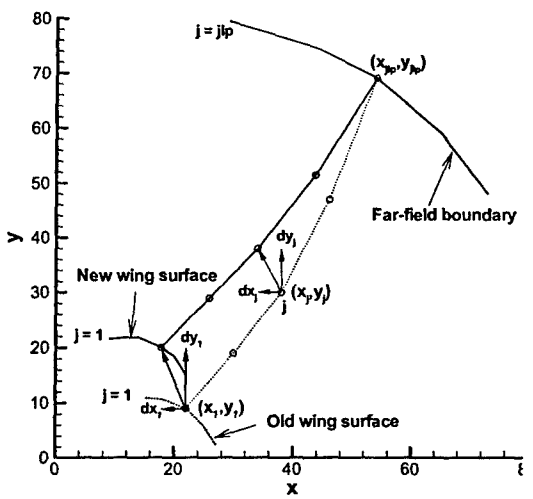

Figure 12.131: A sketch of the mesh d formation

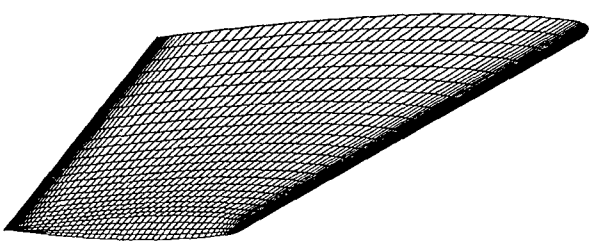

Figure 12.133: The mesh around the ONERA M6 wing surface.

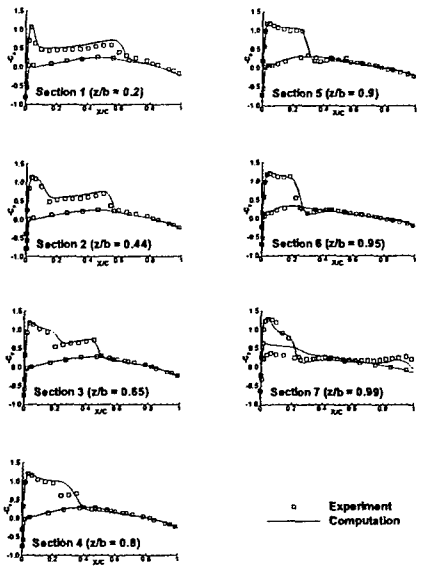

Figure 12.134: Pressure coefficients on the wing surface at different cross-section.

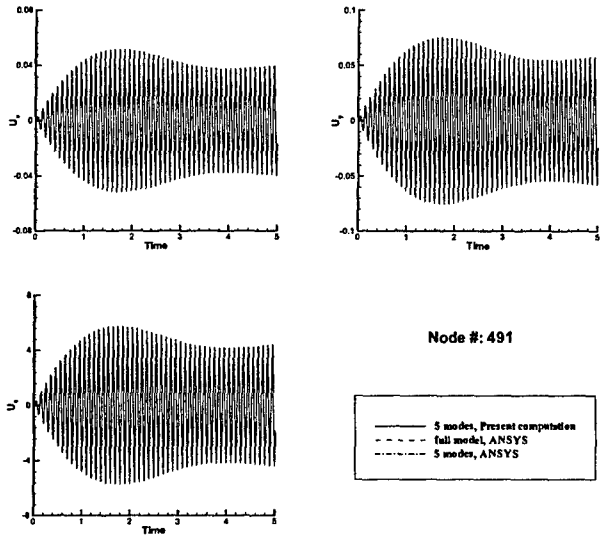

Figure 12.136: Histories of the dynamic responses at node point 491.

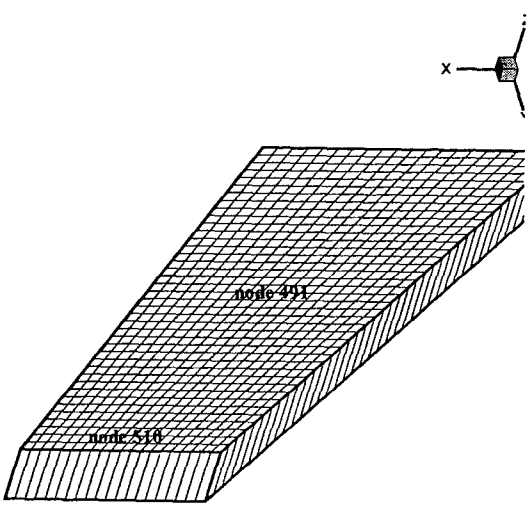

Figure 12.135: Plate wing geometry.

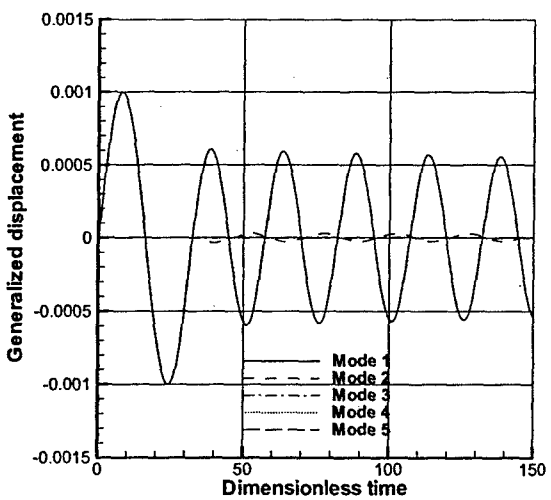

Figure 12.137: Time histories of the generalized displacements of first five modes for $M_\infty = 0.96$ and $V^* = 0.26$ - Damped response.

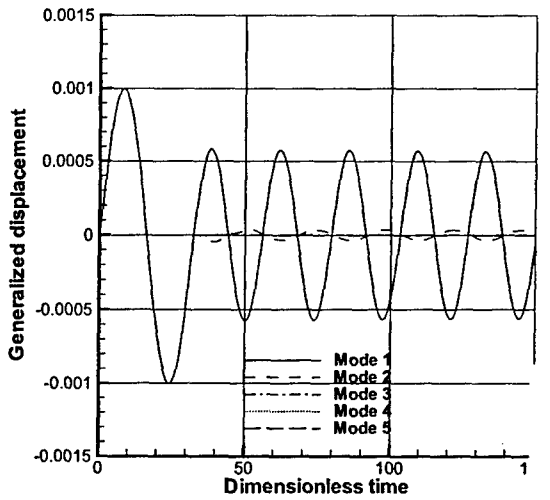

Figure 12.138: Time histories of the ge eralized displacements of first five mod for $M_\infty = 0.96$ and $V^* = 0.285$ - Neutral stable response.

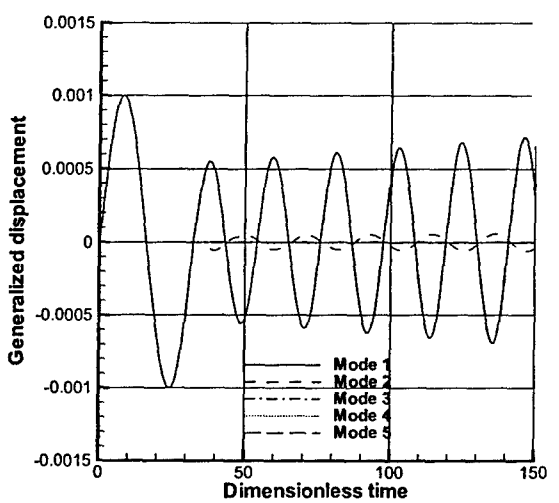

Figure 12.139: Time histories of the generalized displacements of first five modes for $M_\infty = 0.96$ and $V^* = 0.315$ - Diverging response.

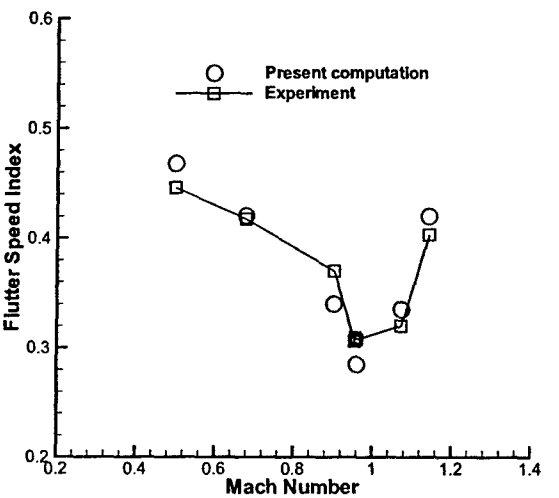

Figure 12.140: Comparison of predicted wing flutter boundary with experimental data for AGARD Wing 445.6.